THESIS REPORT

Master's Degree

Machinability Evaluation of Dental Restorative Materials through Surface Texture Characterization

by S.J. Ng
Advisor: G.M. Zhang

M.S. 96 -6

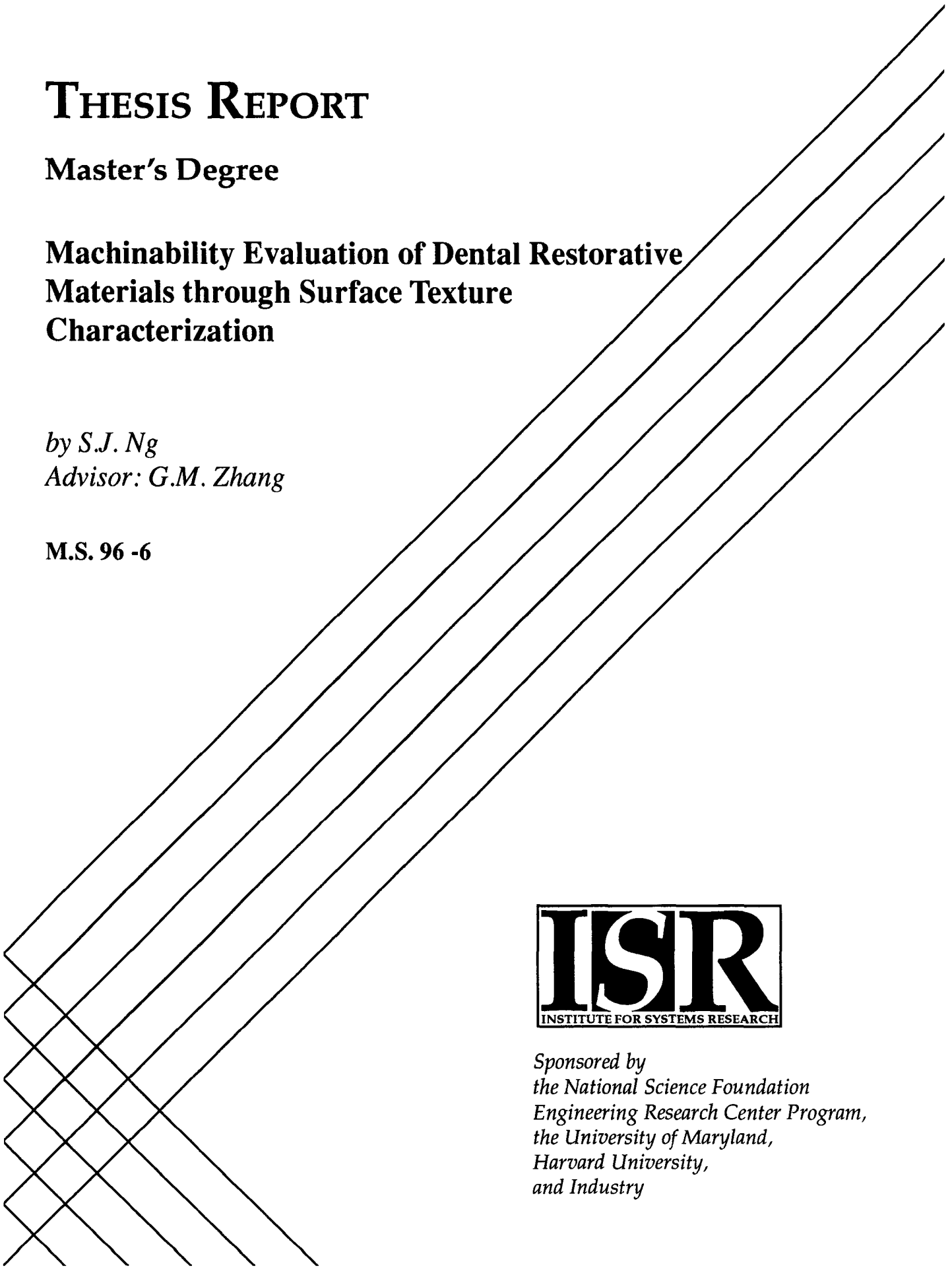

Sponsored by
the National Science Foundation
Engineering Research Center Program,
the University of Maryland,
Harvard University,
and Industry

Machinability Evaluation of Dental Restorative Materials through Surface Texture Characterization

by

Stanley Jay Ng

Thesis submitted to the Faculty of the Graduate School of the
University of Maryland in partial fulfillment
of the requirement for the degree of
Master of Science
1996

Advisory Committee:

Associate Professor Guangming Zhang, Chairman/Advisor
Professor Davinder K. Anand
Associate Professor K. J. Ray Liu

Abstract

Title of Thesis:	Machinability Evaluation of Dental Restorative Materials through Surface Texture Characterization
Name of degree candidate:	Stanley Jay Ng
Degree and Year:	Master of Science, 1996
Thesis directed by:	Dr. Guangming Zhang, Associate Professor Department of Mechanical Engineering, and Institute for Systems Research

Ceramic materials are ideal candidates for dental restorative applications for their color, texture, and mechanical properties which closely resemble those of the human enamel. However, due to the inherent brittleness of ceramic material, material processing, especially machining, poses a variety of difficulties. Research efforts of this thesis are directed to the development of a critical guideline for evaluating the machinability of ceramic materials, where human enamel is used as a reference material for comparison

Using a systems engineering approach, a computer-based surface integrity assessment methodology is formulated. It combines the most recently developed image processing technology with computer graphics while incorporating the principles of fracture mechanics. Microhardness testing is used to study material properties related to machining. Four types of material selected are human enamel, Dicor-MGC, HCC Dentine, and HCC Enamel. Three-dimensional visualization of the surface impressions is achieved using an environmental scanning electron microscope and an atomic force microscope. Machining experiments are conducted to study the surface integrity, including surface finish, micro-cracking, and edge chipping. Analytical investigation correlates these surface responses to the machining parameters, such as spindle speed, feed rate, and the depth of cut, to seek a parametric region in which quality of machined ceramic components can be ensured. Surface integrity

performance indices such as surface roughness, cavity density, and chip aspect ratio are proposed to quantify such evaluations.

Major contributions of this thesis research include the development of the combined SEM-AFM stereophotography method. The high resolution achieved with this method ensures coverage of rich information on the surface texture formed during machining. Specific findings of this thesis research include the identification of micro-mechanics of fracture occurred during the material removal process ,and a good understanding of possible influences of the microstructures on the machining performance.

Machinability Evaluation of Dental Restorative Materials through Surface Texture Characterization

by

Stanley Jay Ng

Thesis submitted to the Faculty of the Graduate School of the
University of Maryland in partial fulfillment
of the requirement for the degree of
Master of Science
1996

Advisory Committee:

Associate Professor Guangming Zhang, Chairman/Advisor
Professor Davinder K. Anand
Associate Professor K. J. Ray Liu

ACKNOWLEDGMENTS

I would like to express my sincere appreciation to Professor Guangming Zhang for providing tremendous inspiration and guidance throughout the course of my thesis study. Besides Professor Zhang, I would also like to thank Professor Davinder K. Anand and Professor K. J. Ray Liu for serving on my committee.

Special acknowledgments are due to the educational support provided by the Department of Defense (D.O.D) through the Defense Acquisition Scholarship Program. In addition, I also like to thank other research fundings granted by the National Institutes of Health, Mechanical Engineering Department, and the Institute for Systems Research which make this work possible.

Special gratitude is due to all my colleagues and friends at the Advanced Design and Manufacturing Laboratory. Personally, I like to thank Mr. Wing F. Ko, Mr. Dung T. Le, and Ms. Shelly R. Tucker who have generously donated their invaluable time and energy throughout the course of my study.

Finally, I like to thank my family for all they have provided and done for me. I could not have accomplished what I have done without their genuine guidance and understanding.

DEDICATION

To my father, who has always provided the best for me and taught me everything he believes in, and my wonderful sister who has provided her love and encouragement at all times.

TABLE OF CONTENTS

LIST OF TABLES

LIST OF FIGURES

Chapter 1

Introduction

1.1 Advanced Ceramics for Dental Restorations

Advanced ceramic materials have been successfully developed during the past decades. They are widely used in a variety of applications for their superior properties, such as high-strength-to-mass ratio, excellent wear resistance and exceptional corrosion resistance, compared to conventional materials, such as metals and plastics. The capability of ceramics to be manufactured to near net shape by pressing and sintering processes also makes economic production of ceramics possible. These desirable intrinsic properties and advances in manufacturing technology have led ceramics to be prime candidates for dental restorative fabrications.

Although the development of advanced ceramic materials has progressed tremendously over the years, barriers to their wide acceptance exist. One of these barriers is the inherent difficulty in material processing. For instance, after sintering ceramic material becomes hard and brittle. In the processing of ceramic material using traditional methods, such as machining and grinding, fracture occurs at stress-concentration locations which leaves cracks on and beneath the machined surfaces of ceramic components. These processing induced damage areas degrade the quality of products and often lead to malfunctioning and/or catastrophic failure during the period of service.

Research on processing advanced ceramics has been concentrated on the development of new and innovative machining technologies. Most of these research efforts aim at maintaining the material's distinct features while remaining as cost-

effective as possible. High speed grinding, electro-discharge machining, and laser assisted machining have been exploited for machining ceramics with success [13]. Theoretical studies of deformation and fracture mechanisms of brittle solids have also made steady progress. Important criteria including the Griffith fracture criterion, the Hertzian contact fracture theory, and the Irwin plastic-fracture criterion have been developed to determine the onset of the transition from a deformation process to a fracture process [7,11-13]. Theory of micro-scale bridging between neighboring grains during the micro-cracking along the grain boundaries has directed the development of new ceramic materials with high fracture toughness, leading to significant improvement in strength properties of ceramic components in service.

1.2 Challenge in Using Dental Ceramics

As new types of ceramic material emerge, assessment of their machinability becomes critical to ensure dental restorations made from these materials meet clinic requirements and patient needs. The research work presented in the first part of this thesis is on microhardness tests of human enamel. The obtained information will be used as a critical reference to assess the feasibility of new ceramic materials for use as dental restorative materials in the second part of the thesis. Behavior of material under the hardness testing in general reflects the characteristics of the material removal during machining. Therefore, results from the microhardness testing can be directly used to assess their machinability. It should be noted that the methodology employed in this research is new and different from those previously used in the dental research. It combines recently developed image processing technology, computer graphics, and fracture mechanics. Advanced measurement techniques, such as environmental scanning electron microscopy and atomic force microscopy, are used to provide quantitative

information. The objective of this study is to investigate the behavior of enamel material under hardness testing with emphasis on the effect of enamel rod orientation on hardness. The information for newly developed ceramic materials, such as Corning-MGC, is valuable, especially as it relates to material removal during shaping of dental restorations.

1.3 Scope of the Thesis

This thesis focuses on the research of evaluating the machinability of dental restoration materials using a computer based surface characterization system. The basic methodology employed in this evaluation is composed of three techniques, scanning electron microscopy, atomic force microscopy, and image processing. Special efforts of this thesis work are categorized in the following three areas:

1. Microhardness study of human enamel material. Investigation of hardness of human enamel serves as a reference to the evaluation of other dental restorative materials. Vickers indentations are made and a study of the indentation impression is performed using an atomic force microscope. Accurate three dimensional topographies of the indents are reconstructed using the digitized image data obtained to understand the microstructural properties of human enamel and their effects on performance.

2. Characterization of the surface texture formed in Corning-MGC glass dental ceramic material. To investigate the machinability of dental restorative materials, Corning-MGC is chosen to be machined to study the effect of three machining parameters, spindle speed, feed, and the depth of cut on the machined surface roughness and surface cracking.

3. Control of Machining induced edge chipping in Corning-MGC material. Special efforts are made to characterize the damage found on the entry, interior and exit edges of the machined specimen. A new method using epoxy resin is proposed for the purpose of controlling the fracture damage incurred by the material removal process.

In light of these contents, this thesis presents a systematic study of developing a computer-based system for surface texture and damage characterization in ceramic materials.

1.4 Organization of Thesis

There are seven chapters to this thesis. Although each chapter has been written to be self-contained, each chapter builds on the results of preceding chapters. Two appendices are included. The contents of each chapter are summarized below.

Chapter 2 gives an overview of the relevant literature. This review covers five aspects of advanced ceramic materials. They are the history of ceramic material, physical properties, criteria for material selection, machining, and surface integrity. The review also covers surface integrity assessment techniques for advanced ceramic materials. The review serves as the foundation of this thesis research.

Chapter 3 presents the methodology and results from the microhardness study of ceramic materials. The contents include the experimental setup, data acquisition, and three-dimensional characterization analysis of the surface indentation impressions. Four

types of ceramic material are used in this study. They are human enamel, Dicor-MGC, HCC Dentine, and HCC Enamel. The results obtained from this study strongly indicate that microhardness is an excellent performance index to assess the compatibility of the ceramic materials developed for dental restorations. In order to quantify the assessment, a call for developing a new methodology to quantify the indentation experimentation is proposed. Therefore, the work presented in this chapter serves as a basis for justifying the need to develop the SEM-AFM stereophotography methodology, which is covered in Chapter 4.

Chapter 4 describes the computer-based surface characterization procedure developed in this study. Important techniques such as the environmental scanning electron microscopy , atomic force microscope, and 3D image reconstruction are employed and integrated as a new methodology, called the SEM-AFM stereophotography analysis. Detailed results obtained from applying this new method are presented in this chapter.

Chapter 5 presents the experimental investigation related to machining. Emphasis is given to the assessment of the machinability of Corning-MGC material. Detailed discussions include the experimental set up, design of using a milling operation, and image processing to characterize surface texture formed during machining.

Chapter 6 presents the results obtained from the experiment performed using the Dicor-MGC material. Effects of machining parameters, such as spindle speed, feed an depth of cut, on the quality of the machined surface and machined edges are discussed. Important observations are made through analyzing the combined effects of microstructure and machining parameter settings on the machining performance, illustrating the interdisciplinary nature of the ceramic machining research and pointing

out the importance of adapting machining, namely, the setting of machining parameters has to be considered in such a way that microstructural characteristics of the material being machined are fully taken into account.

Chapter 7 summarizes the thesis research and provides recommendations on continuing research in this field.

Chapter 2

Literature Survey

2.1 Introduction

This chapter presents a background literature survey pertaining to the research subjects related to this thesis work. The survey covers introduction to ceramic materials, physical properties of advanced ceramics, material selection, machining of advanced ceramics, and surface integrity assessment techniques. The survey is divided into five sections. At the end of the survey, an outline of the proposed research is presented.

2.2 Ceramic Materials

In the engineering domain, people have made significant technological progress in every aspect of the design and manufacturing in a product development cycle. However, every progress made has to initiate in the selection of material for making the product. Generally speaking, we live on material.

As we recall, our ancestors used stone as the fundamental material to make tools for survival. The industrial revolution in the nineteenth century had not been possible without the progress in metallurgy at that time. Metals dominated the material supply for the first half of this century until plastics emerged in 1950's. During the past two decades, ceramic material has become a major interest in the research community under the pressure of searching for new and advanced engineering materials.

Ceramics have long been noted for their great strength at high temperature and resistance to heat, abrasion, and corrosion. Man first started using ceramics as low-firing earthwares. Until about 100 years ago, ceramics were considered as everyday pottery for uses such as tableware, clay pipes, and bricks. Even today, despite its many advanced and technical uses, people tend to think of ceramics as simple pottery [6].

Ceramics first real technical use began during the mass production of iron and steel in the latter half of the nineteenth century. Ceramic pots and ladles, made of alumina, silica, or magnesia were used to work with the red hot molten metal. Today, the use of ceramics can be found everywhere. Aircraft, automotive, micro-electronics, and computer are some of the industries that are finding increasing applications for ceramic materials. Typical applications include cutting tools, artificial teeth and bones, automobile spark plugs, brakes, magnets, fiber optics, insulators and many more.

Common sense dictates that ceramic materials are hard to be machined. As a result, most ceramic parts are manufactured to near net shape by hot pressing and sintering the ceramic powder. However, advances in today's technology requires parts with a higher degree of machine accuracy. Precision machining is now required after sintering. To meet today's demand, traditional and nontraditional methods of machining ceramics need to be improved or developed to achieve the full potential of ceramics.

The need for high-strength materials at high temperature applications has led to the development of advanced ceramics. Ceramics are formed from a powder compound and then sintered. Composed of oxide or non-oxide based compound, ceramics can acquire different material properties depending on the manufacturing process. Oxide based compounds tend to be made of natural occurring materials where non-oxide based compounds are made of artificial material. Compared to oxide based ceramics, non-

oxide based ceramics are stronger and harder with a higher resistance to thermal shock. These non-oxide ceramics show great promise in engineering applications [16].

Ceramics are recognized for their high-strength at high temperatures, yet they are commonly brittle and have a low thermal shock resistance. Other advantages that ceramics have over other materials is its superior heat resistance, wear and abrasion resistance, hardness, corrosion resistance, and lightness. As a result, strategic material considerations and economic factors are forcing the modern industries towards the use of ceramic components.

2.3 Dental Ceramic Materials

Ceramic materials are inorganic, nonmetallic materials which consist of metallic and nonmetallic elements bonded together primarily by ionic and/or covalent bonds. Due to the variation of chemical compositions, there is a variety of ceramic materials used today in industry. New and advanced ceramic materials, such as alumina, zirconia, silicon carbide, silicon nitride, are generally distinguished as structural ceramics for their high strengths, hardness and toughness. There is another group of ceramic materials, such as DICOR/MGC, HCC Dentine, and HCC Enamel. These glass-ceramic materials are produced by the controlled crystallization of appropriate glasses. The basic structure of ceramic materials is a composite consisting of a large portion, typically 95 to 98 vol%, of very small crystals, generally smaller than 1 micron, with a small amount of residual glass phase to make up a porefree composite [17].

In this research, we focus on glass-based ceramics, specifically on DICOR/MGC, HCC Dentine and HCC Enamel. The mechanical properties of these ceramic materials are listed in Table 2.1 [8].

Table 2-1 Mechanical Properties of Dental Ceramic Materials

	Human Enamel	MGC Material	HCC Enamel	HCC Dentine
Compressive Strength (MPa)	392	812	579	.579
Coefficient of Thermal Expansion (ppm/ C)	8-11	7.2	14	14

2.3.1 Microhardness Testing of Materials

Hardness of a given material is an important indicator in terms of understanding the behavior of material when it is subjected to a certain loading condition. The hardness of a given material is determined by hardness test. In general, the hardness test is performed on a specific designed machine. The test by itself measures the resistance to penetration of the surface of a material by a hard object. A variety of hardness tests have been devised, but the most commonly used are the Brinell test, the Rockwell test and the Micro-hardness test [2].

Brinell Hardness Test. Figure 2-1 illustrates the Brinell hardness test in which a hard steel sphere, usually 10 mm in diameter, is forced into the surface of the material. The diameter of the impression left on the surface is measured and the Brinell hardness number (BHN) is calculated from the following equation:

Brinell Hardness Test: $$BHN = \frac{F}{(\pi/2)D(D - \sqrt{D^2 - D_i^2})} \qquad (2.1)$$

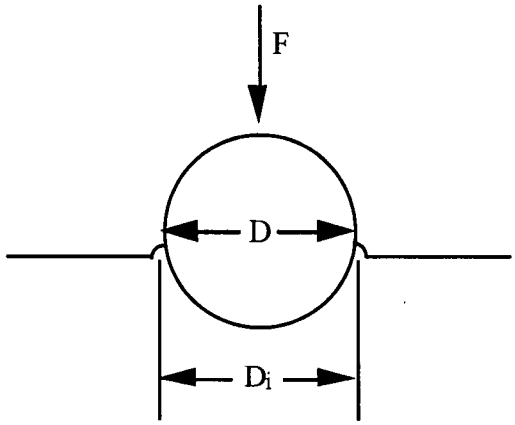

Figure 2-1 Brinell Hardness Test

Rockwell Hardness Test. The Rockwell hardness test use either a small diameter steel ball for soft materials or a diamond cone, or Brale, for hard materials. The depth of penetration of the indentor is automatically measured by the testing machine and converted to a Rockwell hardness number . Several variations of the Rockwell test are used, as shown in Figure 2-2.

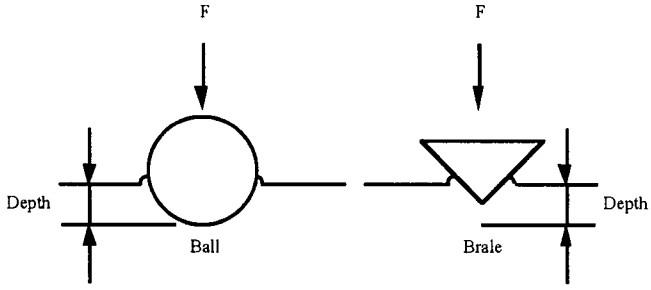

Figure 2-2 Rockwell Hardness Test

Micro-hardness Indentation Test. This type of hardness test is specifically designed for testing the hardness of an object, which is in a micro-scale, such as microstructures. Under those circumstances, macro-scale tests, such as Brinell and Rockwell tests, are not applicable. Two of the most common mechanical parameters

used for comparison purposes are the Vickers and Knoop micro-hardness numbers. Vickers and Knoop Micro-hardness testing involves the indentation of a material at a specified load. The indentations are examined under a microscope in order to measure the lengths of the indentation diagonals. These diagonal lengths are then used in the following formulas to acquire the hardness values [31],

For Vickers Hardness Tests: $$VHN = \frac{1.854 \cdot P}{d^2} \quad \left[\frac{kg}{mm^2}\right] \tag{2.2}$$

For Knoop Hardness Tests: $$KHN = \frac{14.23 \cdot P}{d^2} \quad \left[\frac{kg}{mm^2}\right] \tag{2.3}$$

where the load, P, is in kg, and the diameter, d, is measured in mm.

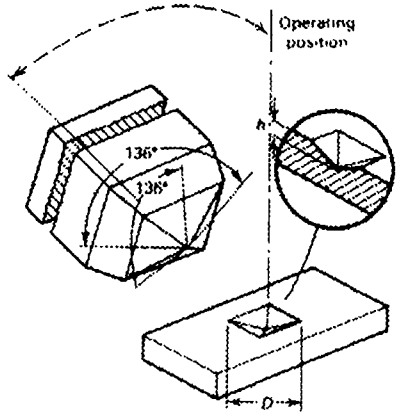

Figure 2-3 Vickers Indentation Test

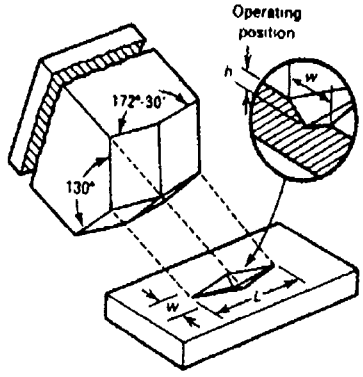

Figure 2-4 Knoop Indentation Test

The rewards of using micro-hardness indentation testing are two-fold: a load-hardness curve for the material can be generated and thus easily compared to other materials, and the qualitative information gained from the damage of indentations can be transferred through image processing into quantitative information that will yield desired surface parameters. Such parameters include the amount of elastic recovery after indentation, the surface cavity density, and the surface roughness.

2.3.2 Formation of Microcracks in Ceramics

To gain a basic understanding of the surface cracking during the material removal process, experiments using sliding microindentation between a diamond indentor and ceramics have been performed [10]. In the machining of ceramics, the presence of chips, the formation of surface texture, and the tool wear observed on rake and frank faces support the existence of the three deformation zones observed during the machining of conventional materials such as metals. However, cracks formed on the machined surface, which are in micro-scale, give distinction to the fundamentals of material removal mechanisms during the machining of ceramics. The experiments simulate the direct contact between the cutting tool and the part material during the machining process. Observations made from these experiments have indicated that a diversity of cracks, such as median cracks, lateral cracks, and cone cracks, are generated in the vicinity of the scratched groove, or along the "tool path", as illustrated in Figure 2-5. Based on a recent study [11], the cracks formed on the machined surface are mainly related to the median cracks, which propagate in the direction of the applied cutting force. The lateral cracks, that run parallel to the machined surface, play a dominant role in the chip formation process. The cone cracks emanating from the edge of the contact impression are surface ring cracks. They grow incrementally downward and disappear in the catastrophic failure mode at instants when chips are formed.

According to Griffith, fracture under tensile stress of a brittle solid is always initiated by a crack. The stress-intensity factor, a parameter characterizing the effects of the applied stress, the crack shape and size on stress-concentration at the crack tip is given by [7],

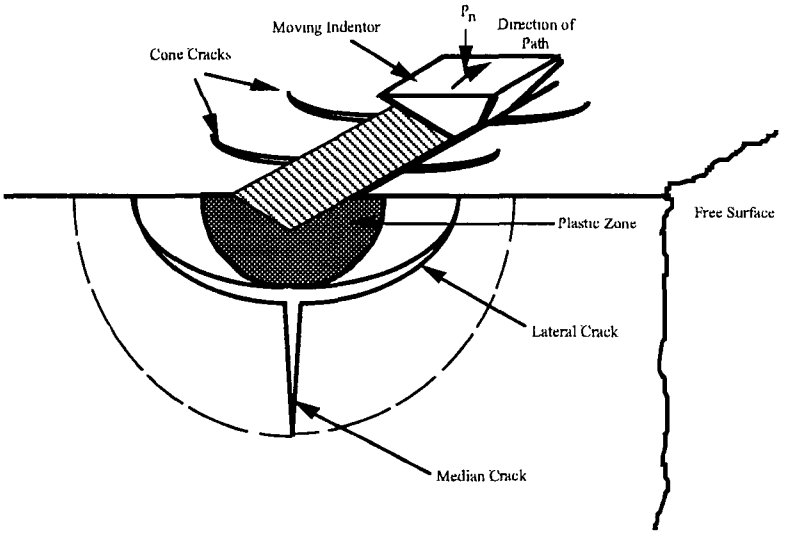

Figure 2-5 Cracks Formed during the Sliding Microindentation of Ceramic Material

$$K_I = 1.12\sigma\sqrt{\pi a / Q} \tag{2.4}$$

where s = applied stress, a = depth of a surface crack, and Q = crack-shape parameter as a function of the ratio a/2c where 2c stands for the width of a surface crack. For surface cracks on ceramic materials, an empirical model to estimate the Q value is given by [15]

$$Q = 2.23 + 0.20\frac{\frac{a}{2c}}{0.05} \qquad for\ 0.50 \le \frac{a}{2c} \le 2.0 \tag{2.5}$$

2.4 Assessment of Surface Integrity

In many industrial applications, the characterization of surface topography cannot be underestimated. In particular, surface topography is critical in the study of microcracking, surface texture and edge effect in ceramic materials. In addition,

surface roughness is an important performance index, as illustrated in Equation (2.6), to characterize the smoothness of the surface finish in dental restoration [14],

$$Ra = \frac{\sum (h_i - \bar{h})}{Area\ of\ Interest}$$

$$\begin{aligned} where,\quad & Ra = Surface\ Roughness \\ & h_i = Sample\ Height\ \ Measurement \\ & h = Mean\ Height\ Measurement \end{aligned} \tag{2.6}$$

To characterize surface integrity, numerous instruments have been invented. . Traditionally, the quality of the surface is measured by traditional technique such as two-dimensional profilometry. However, in order to provide an in-depth understanding of the surface texture, instruments which can capture three dimensional data must be used. In this thesis, a combinational technique utilizing the methodology of atomic force microscopy and scanning electron microscopy are used. They are described in the following sections.

2.4.1 Traditional Two Dimension Profilometry

The basic stylus instrument consists of the following five components: a transducer, a chart recorder, an amplifier, a traverse unit, and a meter system. In the transducer, a linear variable differential transformer (LVDT), changes in amplitude or height vary the mutual inductance. In turn, the change in mutual inductance alters the phase of a high frequency carrier signal. Then, the signal is amplified and de-modulated to represent the surface topography. Next, the signal can be recorded on a chart recorder. As shown in Figure 2-6, the traverse unit displaces the entire instrument in the horizontal or spatial direction. The skid is used as a reference datum according to

which the surface topography is recorded. Some commercial stylus based profilometers include the Perthometer S8P, the Surfcom 475/575-3D, and the Surfascan 3-D.

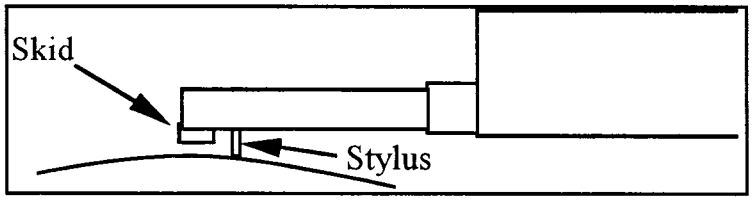

Figure 2-6 Stylus Instrument

The traditional stylus based profilometers are popular for several reasons. First, these instruments are not as expensive as other commercially available surface measurement systems. Second, workpieces do not need to be prepared before examination. In terms of resources and time, this is a considerable advantage of these measurement instruments. Third, the test procedure involved in obtaining a surface profile is relatively simple.

However, the disadvantages associated with stylus type profilometers considerably outweigh the aforementioned advantages. First, these profilometers have been traditionally used to produce two dimensional (2-D) representations of the surface texture. The primary problem with individual profiles obtained at different locations of the workpiece is their lack of a comprehensive representation of the machined surface. Recently, stylus type measurement instruments have been modified to create three dimensional (3-D) surface plots. However, the time required to record a 3-D surface plot using this measurement instrument is considerably longer than when using other measurement instruments. Hence, stylus based instruments cannot be adequately used in on-line monitoring systems.

Second, the effect of waviness in the overall roughness measurement is another issue of concern. Waviness, an index of the overall flatness of the surface, will be significant if a workpiece has topographical features with a wavelength larger than the skid length. Third, isolated extremities in the surface finish may yield erroneous measurement data. Fourth, the contact between the stylus and the specimen may result in permanent damage to both the stylus and the specimen, i.e., the measurement process may introduce damage.

Finally, wear of the stylus is also a significant disadvantage of stylus type instruments. With increasing wear, the geometry of the tip of the stylus changes, i.e., the radius of the stylus tip changes. In turn, as shown in Figure 2-7, the topography will not be accurately traced. Any irregularities smaller than the nose radius of the stylus, in particular the median cracks mentioned in Section 2.3.2, will not be detected. Consequently, the resolution specified by the manufacturer will no longer be attained.

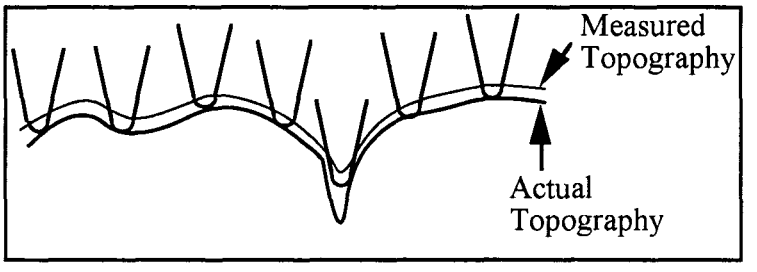

Figure 2-7 Effect of Worn Stylus Tip

2.4.2 Atomic Force Microscopy

Atomic force microscope is a more sophisticated type of surface profilometer capable of obtaining measurements in three dimensions. As shown in Figure 2-8, a sharp atomically sized metal tip connected to a cantilever beam is traversed over the surface of the sample. However, in an atomic force microscope, a direct contact

between the surface and tip is established. The surface roughness is obtained from the atomic force between the stylus tip and the surface. As before, different modes of operation exist. In the first mode, the sample is modulated with the natural frequency of the cantilever beam in the height direction. In turn, the cantilever is deflected because of the force between the two objects. A tunneling current, which controls the feedback mechanism, is modulated to maintain a constant force. In the second mode of operation, the cantilever beam is modulated at its natural frequency. In turn, both the phase and amplitude of the tunneling current are changed. The amplitude controls the feedback mechanisms. In the third mode, the phase, instead of the amplitude is used to control the feedback mechanism. Finally, in the fourth mode, a constant gap between the workpiece and the stylus tip is maintained by varying the force on the tip.

There are several advantages of using the atomic force microscope for surface measurements. First, as before, the attainable resolution in the spatial and amplitude directions is noticeably better than that of conventional stylus type profilometers. Second, if the atomic force microscope is used, workpieces do not have to be conductive. Third, the speed with which the surface topography can be reconstructed allows for possible the use of the technique in on-line monitoring processes.

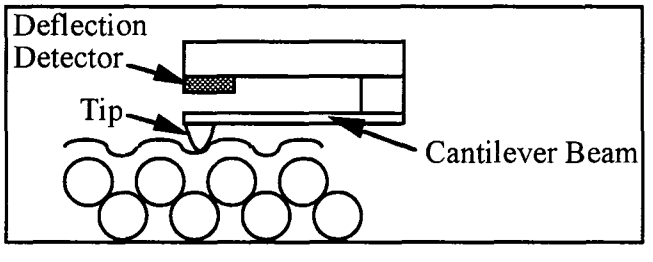

Figure 2-8 Atomic Force Microscopy

2.4.3 SEM-Stereophotography Methods

Recently, image processing methods and electron microscopy have also been used to evaluate surface finish. In these methods, a picture of the machined surface is obtained first. Next, image processing techniques are used to digitize the picture and to characterize the surface integrity. Overall, electron microscopy can be divided into different categories depending on the type of microscope used. First, in transmission electron microscopy (TEM), an image is obtained by magnifying and focusing scattered electrons. Resolutions of up to 0.3 nm have been achieved. However, the primary drawback of TEM is the requirement that the sample used be relatively thin (less than 1μm thick). Hence, a replicate of the surface needs to be made to ensure that the correct thickness is used. Second, scanning electron microscopy (SEM) has also been used to characterize surface topography. In SEM, a raster image is obtained after a focused beam of electrons scans the surface of the specimen. The primary advantage of scanning electron microscopy over transmission electron microscopy is the non-requirement of thin samples. However, workpieces to be examined need to be conductive. Overall, microdensitometric methods are used to convert electron micrographs into grayscale image data. Based on the grayscale level intensity (0 to 255 levels), height data are obtained. Next, after obtaining spatial and amplitude data, fractals, along with other image enhancement techniques, have been used to reconstruct surface topography. The SEM-Stereophotography method will be employed in conjunction with the Atomic Force Microscopy to provide a basis for evaluating the surface integrity of the experimental ceramic materials.

2.5 Summary

Recognizing the stragetic need in ceramic material and ceramic-made products, the University of Maryland initiated ceramic machining research in 1991. Since then researchers at the university have made significant contributions to the knowledge of processing ceramic materials.

At the Advanced Design and Manufacturing Laboratory, ceramic machining research covers optimization of setting machining parameters, on-line detection of the cutting force, and implementation of a computer-based system to perform non-destructive evaluation of surface integrity with emphasis on the investigation of crack systems formed during machining. One Ph.D thesis and three MS theses [9, 14, 15, 25] have been published to summarize the results obtained from the on-going research activities. The material covered in this thesis represents the continuation of these research activities.

Specific topics to be covered in this these are hardness indentation, submerged machining, and assessment of surface integrity using image processing. Advanced computer graphics and software tools are introduced. State-of-the-art facilities, such as an envrionmental scanning electron microscope and an atomic force microscope, are employed in this thesis study.

Chapter 3

Investigation of Microhardness of Ceramic Materials

3.1 Introduction

The focus of this thesis study is the assessment of machinability of ceramic materials. Machinability, as a performance index, has been commonly used in the material processing research to indicate the easiness of a machining operation under which a specific type of material is being processed. A better machinability means the cutting force generated during machining is at a relatively low level, the vibration of tool/workpiece is also at a low level, the tool wear is at a slow rate, and the finish quality can be ensured with ease.

Generally speaking, ceramic materials possess one of the worst machinabilities among all the engineering materials being used. High hardness of ceramics has posed difficulties in removing excessive material for making a defined geometry. A more important aspect is that the brittle nature of ceramics induce cracks, especially micro-cracks, leading to a high failure rate of products made of ceramics during their service.

In order to assess the machinability of the ceramic material designed for dental restoration fabrication, microhardness tests have been selected as the major effort to assess machinability. For establishing a reference for comparison, the investigation begins with a study of microhardness of human enamel. After that, research efforts are devoted to studying three newly fabricated dental restorative materials. These three dental restorative materials are Dicor-MGC, HCC Enamel, and HCC Dentine. The obtained information will be used as a critical reference to assess the feasibility of new

ceramic materials for use as dental restorative materials. Behavior of material under the hardness testing in general reflects the characteristics of the material removal during machining. Therefore, results from the microhardness testing can be directly used to assess their machinability. It should be noted that the methodology employed in this research is new and different from those previously used in the dental research. It combines recently developed image processing technology, computer graphics, and fracture mechanics. Advanced measurement techniques, such as environmental scanning electron microscope and atomic force microscope, are used to provide quantitative information. The objective of this study is to investigate the behavior of enamel material under hardness testing with emphasis on the effect of enamel rod orientation on hardness. Such information for newly developed ceramic materials should be valuable, especially as it relates to material removal during shaping of dental restorations.

3.2 Specimen Preparation and Hardness Testing of Human Enamel

As stated, a special objective of this research is to study the microstructural effect of the enamel rod orientations on the hardness measurement. In order to determine the effect of rod orientation, two different planes on the tooth are used for indentation. As illustrated in Figure 3-1, a tooth is first set in an orientation such that the buccal or occlusal surface is parallel to the testing surface. When the occlusal surface is tested, the enamel rods are aligned with the indentation loading. On the other hand, when the buccal surface is tested, the enamel rods are oriented at an angle to the indentation loading. Acrylic resin is used to mount the tooth in this orientation. The exposed surfaces are polished using a set of grit-sized papers and finally with diamond paste. The polishing sequence results in an enamel surface within a 1/4 micron surface roughness.

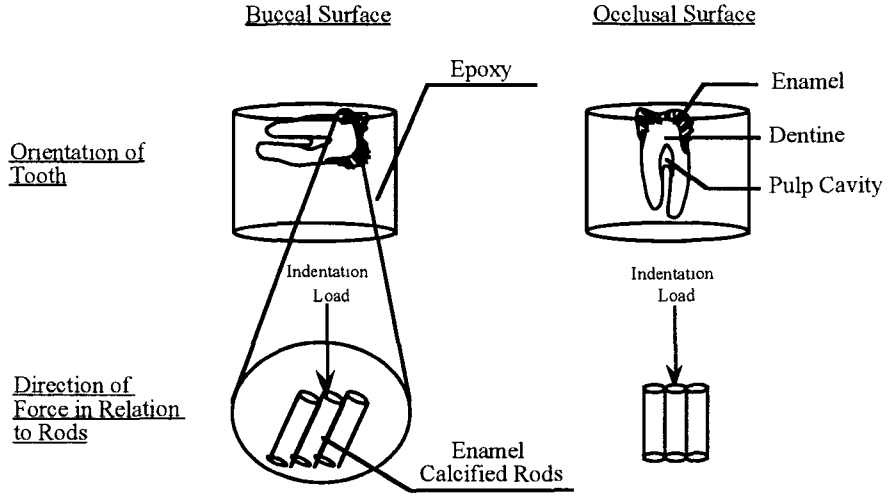

Figure 3-1. Specimen Preparation of the Human Teeth at Two Different Orientation of the Calcified Rods

Specimens prepared in the two different orientations are tested on a Microhardness Indentation Tester Model 300. A Vickers indenter which is a pyramid with edge angle of 136° is used. Eight loading conditions used vary from 50 grams to 2000 grams to model normal functional forces. Under each loading condition, two hardness indentations are performed. Consequently, sixteen indentation tests are done on a molar with a given orientation. Two molars with the identical orientation are used to duplicate the indentation tests. Therefore, a total of sixty-four indentation tests are performed on the exposed surfaces of the four molars in this study.

Four surface impressions obtained from the indentation tests performed are illustrated in Figure 3-2. Among the four impressions, two are taken on the occlusal surfaces and two on the buccal surfaces The loading conditions are 400g and 2000g, respectively. On each impression, two diagonals across the indentation are measured using an optical microscope with 100x magnification. The Vickers hardness number is

obtained by dividing the applied load in kilograms force by the square of the measured diagonal mean in square millimeters, as seen in the following equation,

$$VHN = \frac{1.854 \cdot P}{d^2} \tag{3.1}$$

where: P = load, in kgf, and d = mean diagonal of indentation, in mm. Table 3-1 lists the mean and standard deviation of the hardness measurements.

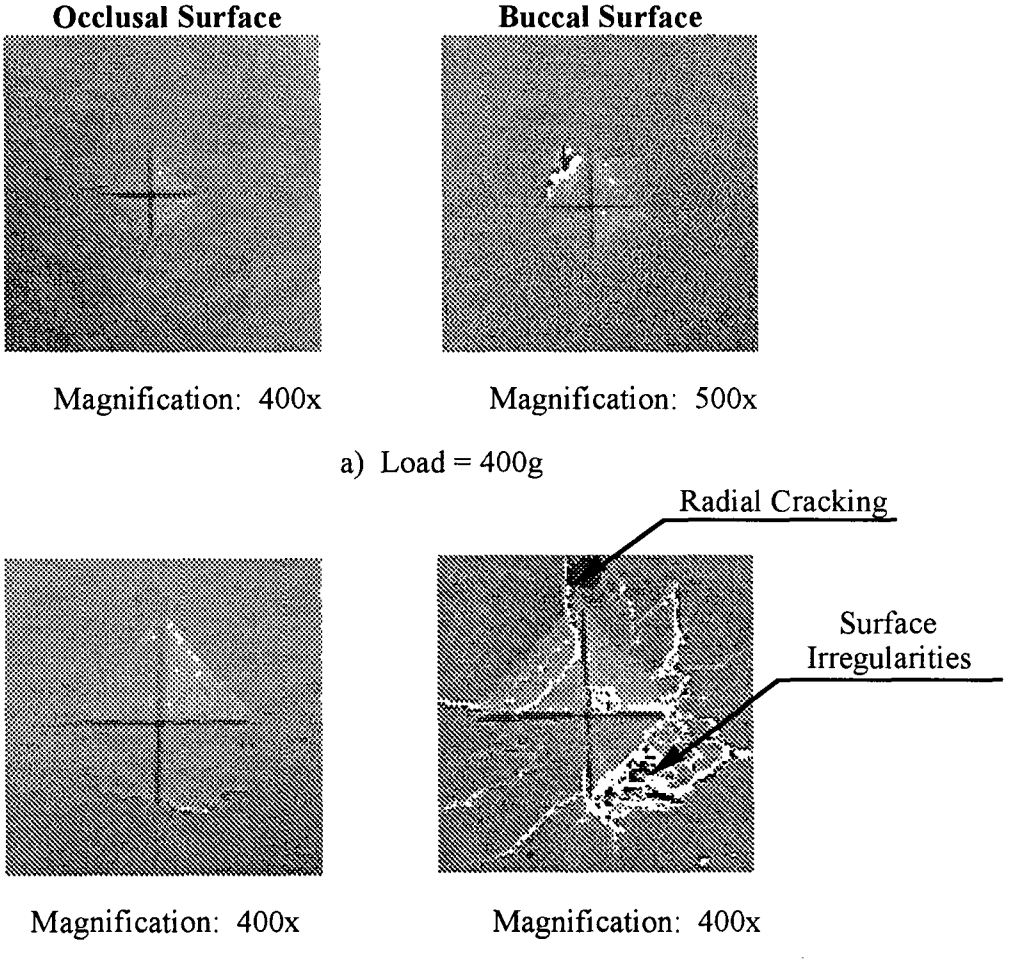

Figure 3-2. ESEM Micrographs of Indentations on the Occlusal and Buccal Surface at Loads of 400g and 2000g.

Table 3-1. Data Obtained from Hardness Measurements

Vickers Hardness Number [Kg/mm^2]				
	Occlusal Surface		Buccal Surface	
Load (g)	Hardness Average	Standard Deviation	Hardness Average	Standard Deviation
50	468	6.6	453	14.5
100	453	13.3	426	23.2
200	430	17.4	412	18.8
400	398	18.3	390	36.3
800	395	3.2	383	8. 9
1000	381	7.4	351	37.2
2000	379	2.4	328	14.4

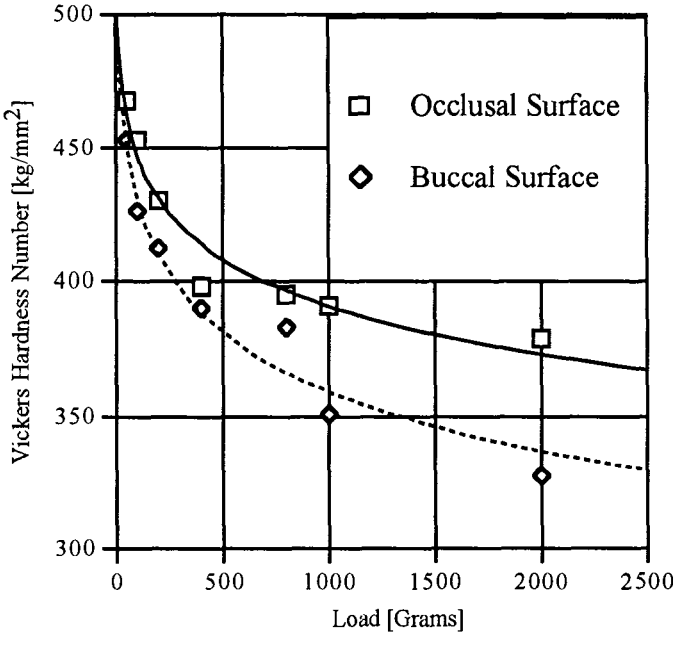

Figure 3-3. Hardness Curves of Enamel on Occlusal and Buccal Surface

To analyze the results obtained from the hardness measurements, the two curves illustrated in Figure 3-3 are constructed using the data listed in Table 3-1. The solid line represents the mean hardness values measured on the occlusal surface and the dashed line

the mean hardness values measured on the buccal surface as the loading condition varies from the low to the high. It is evident that the measured hardness of the human enamel material, either on the buccal surface or on the occlusal surface, is a function of the loading condition. Examining the two plotted curves, a big hardness will be measured under a low loading condition, and a small value of hardness under a heavy loading condition. The variation range covers from 380 VHN [kg/mm^2] when subjected to 400 grams force to 480 VHN [kg/mm^2] when subjected to 50 grams force. Important findings from analyzing the results obtained from the hardness measurements are as follows:

(1) Both curves follow the same trend, i.e., the measured hardness value declines exponentially as the loading increases.

(2) The occlusal hardness-load curve is consistently higher than the buccal hardness-load curve, indicating that the occlusal surface possesses stronger resistance to the indentation force than the buccal surface does.

(3) Standard deviations of hardness measurements on the buccal surface is between 8.9 to 37.2 VHN, which is significantly larger than the standard deviation range of 1.8 to 18.3 VHN observed on the occlusal surfaces. By examining the impressions shown in Figure 3-2, the large standard deviation is mainly contributed by the presence of a crack system developed during indentation.

3.3 Microhardness Testing of Dental Ceramics

As mentioned in previous section, three types of dental ceramics have been tested under the same hardness testing conditions described in Section 3.2. These three dental

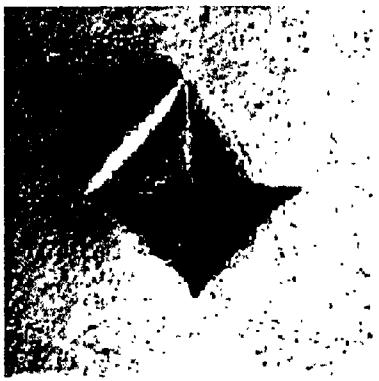

2000g

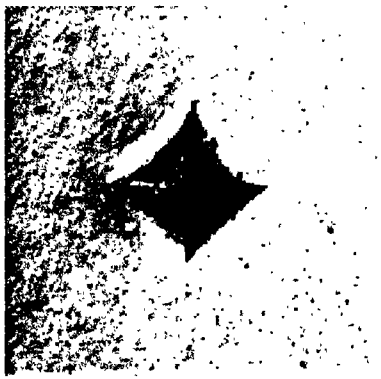

1000g

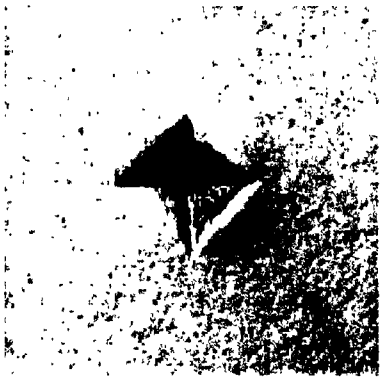

800g

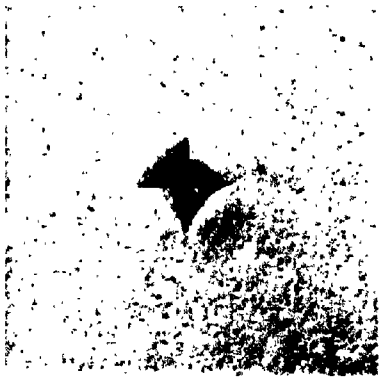

400g

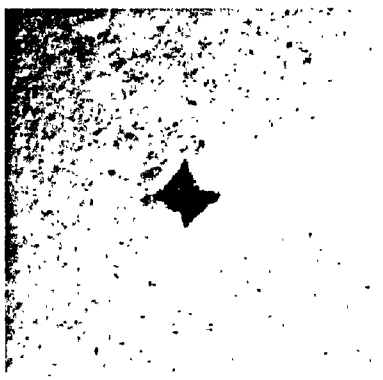

200g

100g

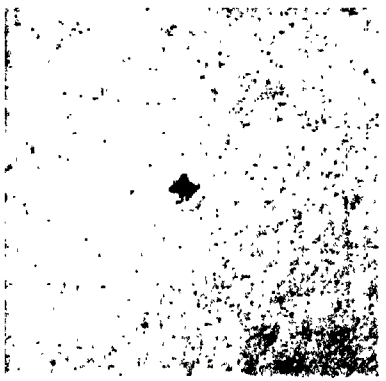

50g

Normarski Micrographs of HCC Enamel Hardness Impressions

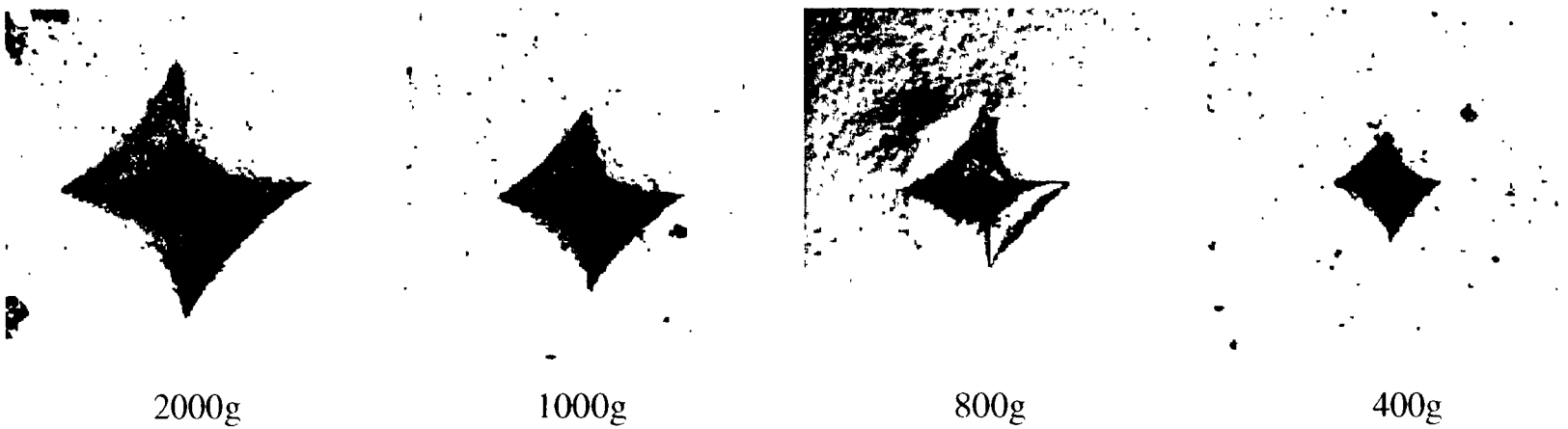

2000g 1000g 800g 400g

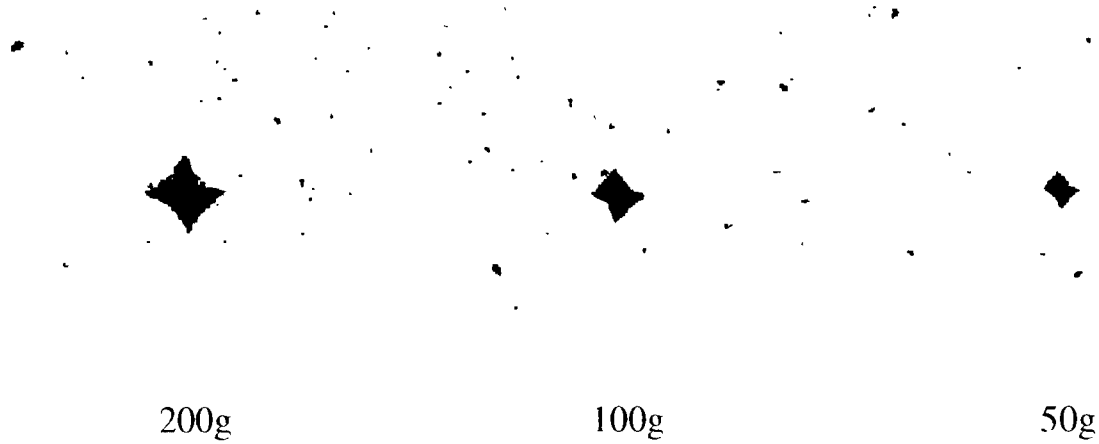

200g 100g 50g

Normarski Micrographs of HCC Dentine Hardness Impressions

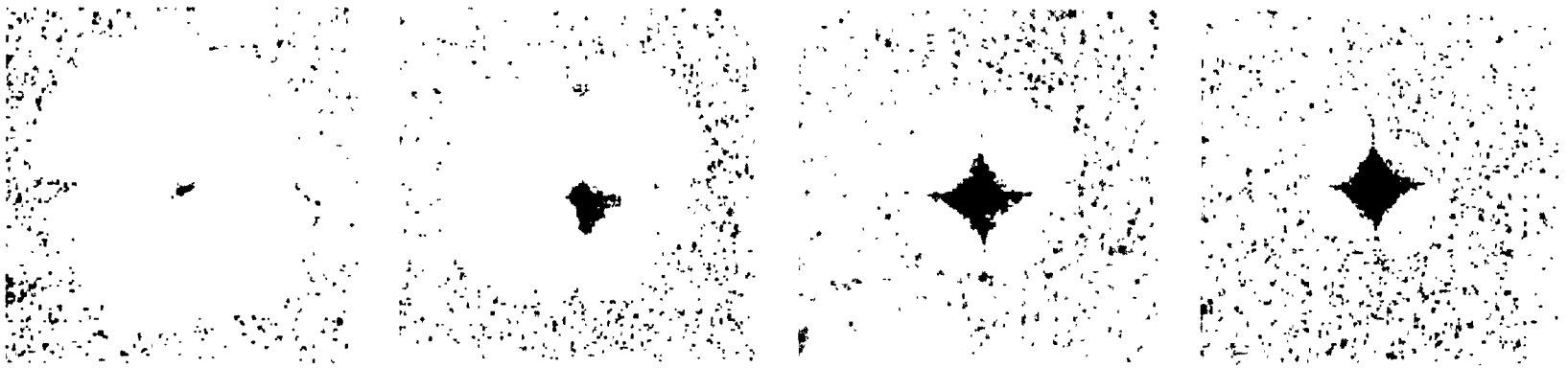

2000g 1000g 800g 400g

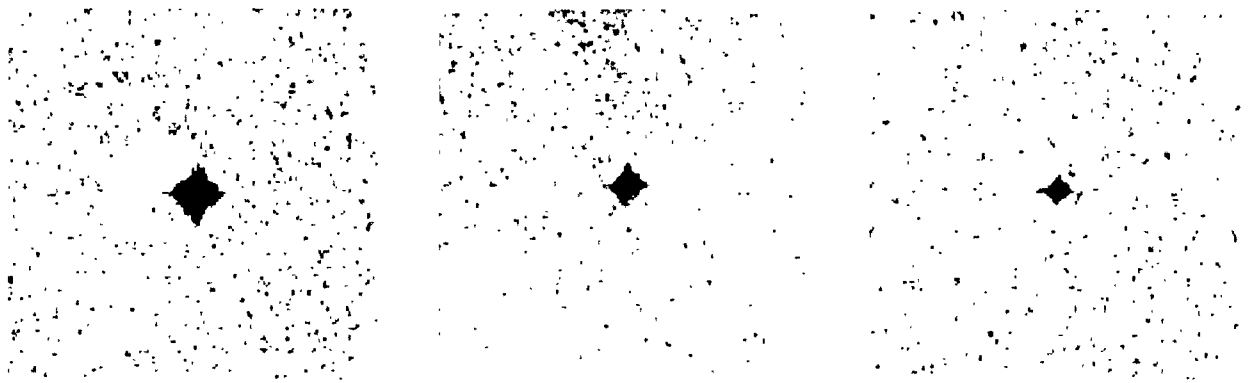

200g 100g 50g

Normarski Micrographs of Corning/MGC Hardness Impressions

Table 3-2 presents the average and standard deviations of the Vickers hardness number obtained from the experiment.

Table 3-2 Hardness Data for 3 types of Dental Ceramics

Vickers Hardness Number [Kg/mm^2]						
	DICOR/MGC		**HCC Dentine**		**HCC Enamel**	
Load (g)	Hardness Average	Standard Deviation	Hardness Average	Standard Deviation	Hardness Average	Standard Deviation
50	407	19.1	191	11.1	218	6.7
100	388	26.3	186	21.6	206	1.5
200	379	16.3	184	1.2	186	0.6
400	386	29.2	172	1.5	184	3.5
800	335	11.8	158	2.3	195	15.3
1000	321	4.2	163	4.6	190	3.1
2000	321	0.2	162	1.4	192	6.8

restorative materials are Dicor-MGC, HCC Enamel, and HCC Dentine. Figure 3-4a, b, and c presents the high magnification micrograhs taken using a Nomarski Microscope.

In order to perform preliminary feasibility study of these new ceramic materials for use as dental restorative materials, their respective hardness curves are constructed in reference to the hardness of the human enamel previously obtained, as illustrated in Figure 3-5.

A number of important observations can be made from the hardness evaluation presented in Figure 3-5. They are listed as follows,

(1) All of the dental ceramics, DICOR/MGC, HCC Enamel, and HCC Dentine, exhibit lower hardness than the human enamel. This is an important observation and a

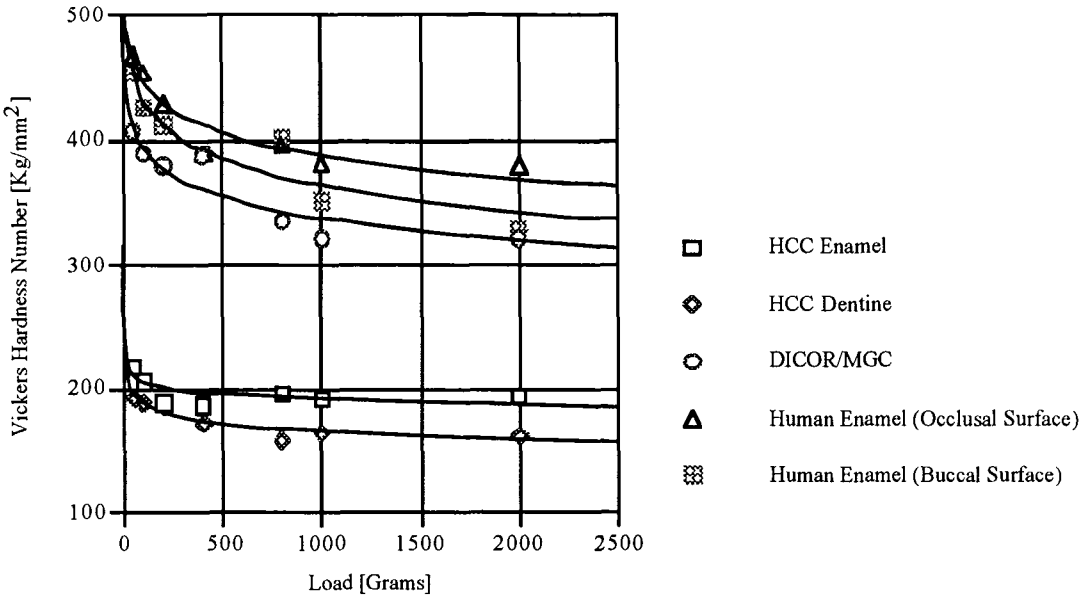

Figure 3-5 Microhardness Testing of 3 types of Dental Ceramics

critical guideline in designing the mechanical property of ceramic material for dental restorations. It is common sense that the dental ceramic replacement must be softer than the human tooth to prevent excessive wear on the enamel surface after clinical implementation.

(2) Two classes of dental ceramics, 'hard' and 'soft' can be identified from Figure 3-4. The first type of dental ceramics, represented by DICOR/MGC, is a tetrasilicic-mica glass ceramics with grain size of 2μm. It is designed to closely resemble the mechanical properties of the human enamel. As illustrated by the hardness values presented in Table 3-3, the average difference of hardness between the human enamel and DICOR/MGC is on the average of 42 kg/mm^2. The second type of dental ceramics, which is represented by HCC Enamel and HCC Dentine. HCC which stands for Hybrid Ceramic Composite, adopts a non-traditional approach of hybridization of organic monomers and inorganic fillers packed in a resin-based matrix. Therefore, the hardness of HCC material is expected to be considerably

less. The average difference between the human enamel and HCC Dentine is about 230 kg/mm^2 whereas the average difference between human enamel and HCC Enamel is about 208 kg/mm^2.

(3) Since the hardness of a material in general gives an indication of the surface characteristics of the material removal process during machining, DICOR/MGC would be an ideal candidate to be used for dental purposes due to the closeness of mechanical property to the human enamel. In Chapter 5, a detail 2^3 factorial design experiment will be used to study the machinabiity of DICOR/MGC.

Chapter 4

Development of a Computer-Based Assessment System

4.1 Needs to Detect Micro-Scale Cracks

In the machining of ceramics, the presence of chips, the formation of surface texture, and the tool wear observed on rake and frank faces support the existence of the three deformation zones observed during the machining of conventional materials such as metals. However, cracks formed on the machined surface, which are in micro-scale, give distinction to the fundamentals of material removal mechanisms during the machining of ceramics. To gain a basic understanding, experiments using sliding microindentation between a diamond indenter and ceramics have been performed by many researchers in this research field. These experiments simulate the direct contact between the cutting tool and the part material during the machining process. Observations made from these experiments have indicated that a diversity of cracks, such as median cracks, lateral cracks, and cone cracks, are generated in the vicinity of the scratched groove, or along the "tool path", as illustrated in Figure 4-1. Based on a recent study, the cracks formed on the machined surface are mainly related to the median cracks, which propagate in the direction of the applied cutting force. The lateral cracks, that run parallel to the machined surface, play a dominant role in the chip formation process. The cone cracks emanating from the edge of the contact impression are surface ring cracks. They grow incrementally downward and disappear in the catastrophic failure mode at instants when chips are formed.

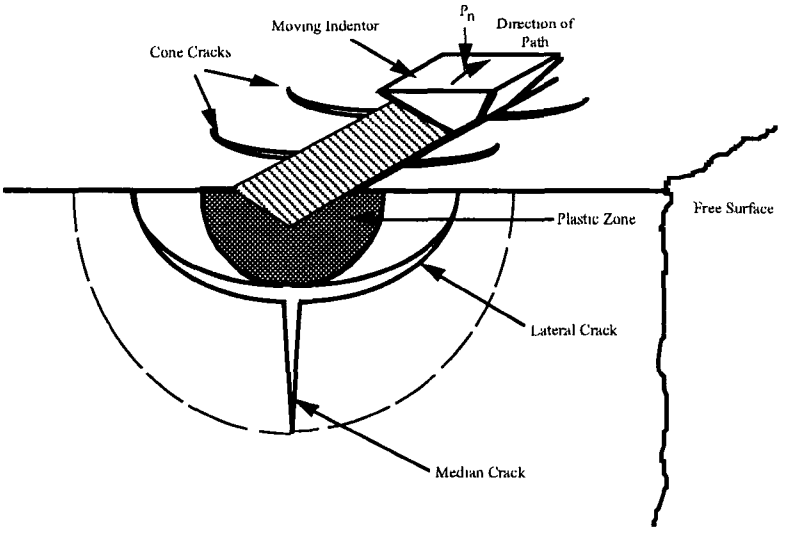

Figure 4-1 Cracks Formed during the Sliding Microindentation of Ceramic Material

4.2 Architecture of a Computer-Based Assessment System

In this study, we apply a new methodology called three-dimensional topography analysis. Through visualization of the hardness impressions, characterization of their geometric shapes is performed using methods of image processing and atomic force measurements. Figure 4-2 illustrates the developed computer-based system to carry out the characterization. The main examination procedure is outlined as follows:

(1) Examination using scanning electron microscopy (SEM) to verify the hardness measurements;

(2) Examination using atomic force measurements (AFM) to obtain digitized indentation topography;

(3) Three dimensional visualization or reconstruction of indentations; and

(4) Quantitative characterization.

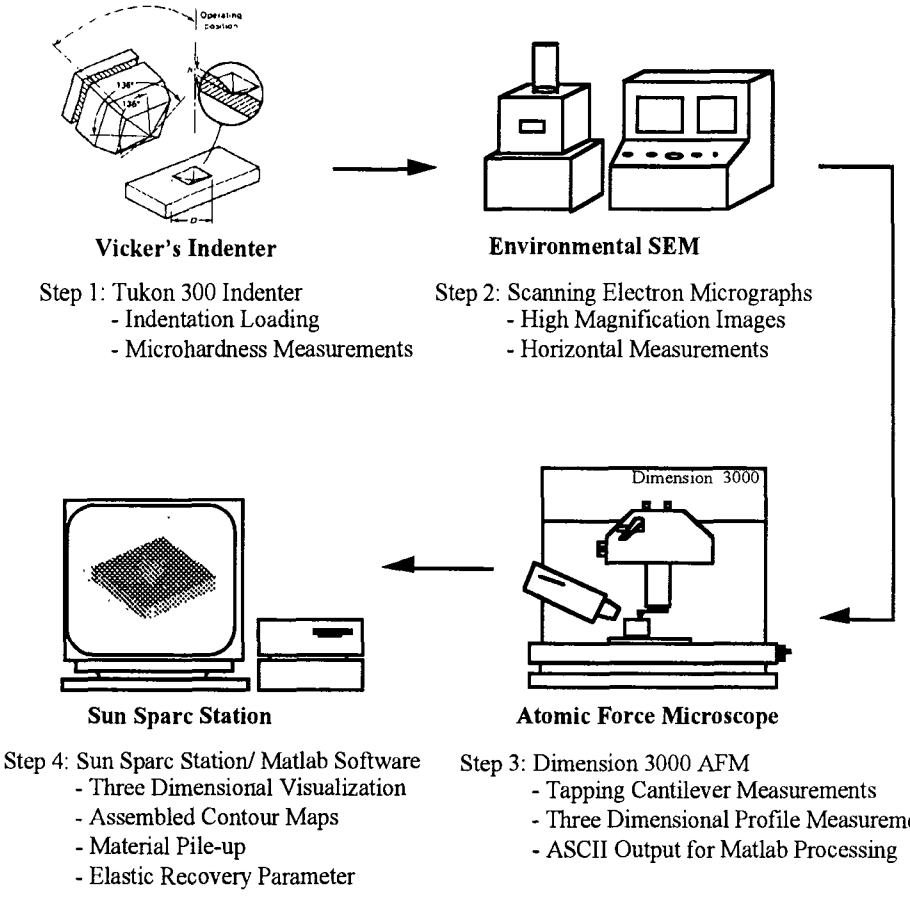

Figure 4-2. Computer-Based System for Characterization of Microhardness Indentations

4.3 Case Study: Characterization of Indentation Impressions

As presented in Section (3.2), The results from the hardness tests indicate that hardness of human enamel varies as the loading condition changes. In addition, the surface orientation has an effect on the hardness measurement. To gain a better understanding, the computer-based assessment system to interpret these observations and identify the significance of this material property on its clinical performance. Such information is important not only to the medical community, but also to the engineering community, which is responsible for designing and manufacturing the material to be used

for dental restoration fabrication.

4.3.1 SEM Examination

In this study, an Environmental Scanning Electron Microscope(ESEM) is used. The four surface impressions illustrated in Figure 3-2 are SEM micrographs taken on both the occlusal and the buccal surfaces indented with loads of 400g and 2000g. The SEM micrographs allow accurate horizontal dimensional measurements to be carried out for verifying the micro-hardness measurements. These micrographs also provide a qualitative assessment of indentations, especially for the effect of the enamel rod structural system on the variations in hardness measurements and fracture patterns formed during indentation.

Examining the four micrographs shown in Figure 3-2, two important observations can be made. The first observation is that the illustrated geometric shape on the occlusal surface reflects the geometry of the indenter. Therefore, the impression has a well defined geometry. Note the rod orientation on the occlusal surface. Because rods primarily extend perpendicularly from the dentinoenamel junction and are generally perpendicular to the occlusal surface. During indentation, the rods are parallel to the applied force through the Vickers indenter and are subjected mainly to compression. Under the compression stress field, the impression is formed under the built-up hydro-static pressure. The indentations at both loading conditions, 400g and 2000g, give a geometrical shape that matches the geometry of the Vickers indenter. As shown in Figure 3-2, radial cracks on the occlusal surface can be observed emanating from corners of the surface impression, at heavy loads, suggesting the release of the accumulated strain energy from the rods. The strain energy is dissipated through plastic deformation and in the process of forming a crack system.

The second observation is that as the load increases, the extent of the resulting damage on the crack pattern formed on the indentation becomes more severe. As illustrated in Figure 3-2, surface deformation and surface irregularities increase with increasing loads from 400 g to 2000 g. On the occlussal surface, the size of the radial cracks increases with increasing load. The crack pattern remains the similar as that of lower loads. Comparable conclusions can be drawn for the buccal surface. As previously mentioned, both radial cracking and surface irregularities can be found on the buccal surface indentations. It is obvious that the extent of the development of these two types of damage increases dramatically from the 400g to 2000g.

4.3.2 Atomic Force Microscopy

Elastic recovery at hardness indentations is a phenomenon well recognized by the research community. As illustrated in Figure 4-2, the indentation process starts in loading, then elastic deformation, plastic deformation, unloading, recovery of the elastic deformation and finally the residual surface impression.

Studies of impression geometries in metallic and non-metallic materials using various standard microhardness indenters indicate that whereas characteristic in-surface dimensions generally remains a reasonable measure of those at maximum loading, (thereby justfying a definition of hardness in terms of post-indentation measurements), the depth of the impression does not. Extremes in depth recovery are shown by 'soft' metals, where it is negligible, and 'highly elastic' rubbers, where it is nearly complete. Therefore, the phenomenon of elastic recovery is an important indicator characterizing the material property to resist the irreversible deformation. Unfortunately, most of the formulas used for hardness evaluation, such as the formula presented in Equation 3.1, do

not count the factor of elastic recovery. As a result, an accurate assessment of material hardness is, if not impossible, difficult to achieve. This is especially true in evaluating the hardness of brittle solids where elastic recovery is usually significant. Another phenomenon to characterize the irreversible, or plastic, deformation is so-called 'pile-up' and 'sink-in', as illustrated in Figure 8. These surface disturbances are formed by dislocation loops generated under shear stress. It is evident that an accurate assessment of hardness has to incorporate both elastic and plastic deformations into the evaluation. To quantify these phenomena, the traditional SEM method is not adequate. A new approach, which is capable of performing measurements in the three-dimensional space, is needed.

In this study, a Dimension^{TM} 3000 Atomic Force Scanning Probe Microscope is used to capture the topographic heights of the indentation geometry in micro-scale [9-11]. The indentation topographic data are obtained using a sampling area of 64 x 64 μm and represents an image resolution of 256 x 256 pixels in both x and y direction. The Z direction accuracy is 1 x 10^{-3} μm and has a maximum depth measurement capability of 6 μm. In processing the data, several software tools are used, including NIH IMAGE and MATLAB [12-13].

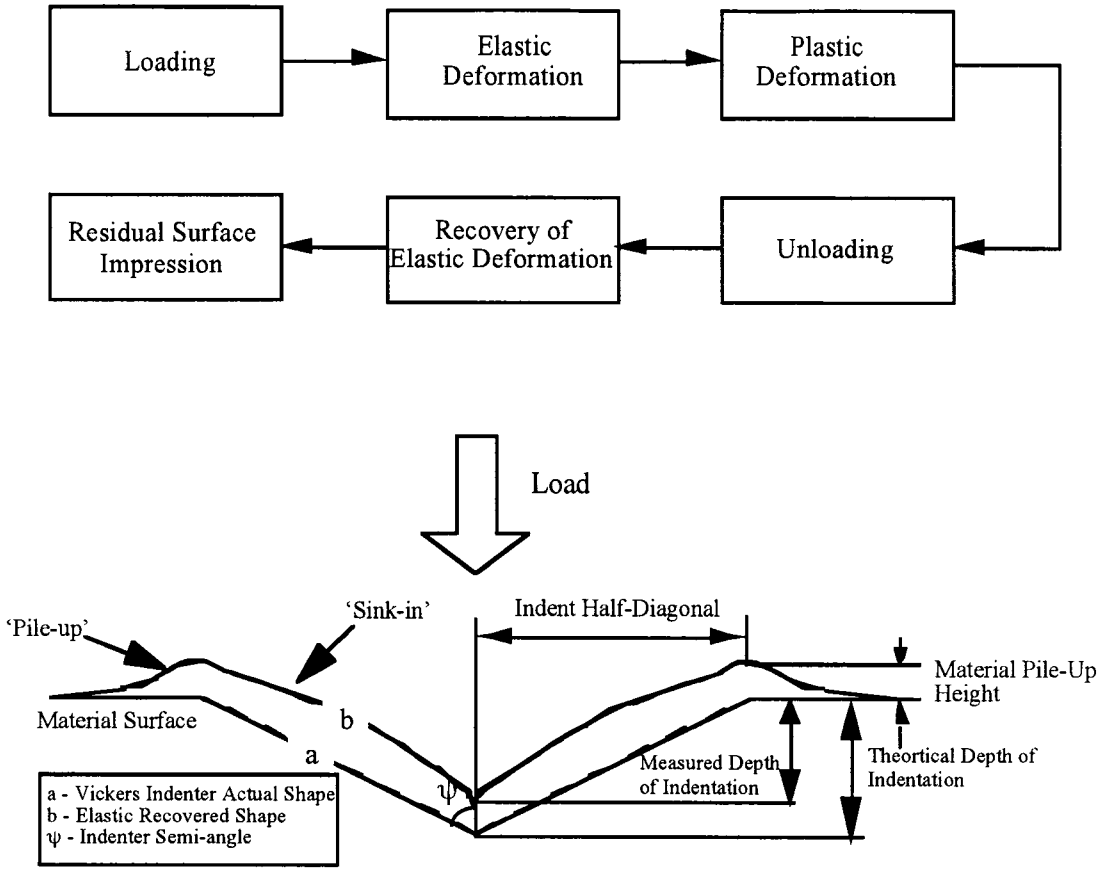

Figure 4-3. Cycle and Illustration of the Profile of Indentation

4.3.3 Three Dimensional Visualization of Indentation

3D image is reconstructed based on the Atomic Force Microscope measurements obtained from the indentations. Several aspects of the three-dimensional visualization of the indentation topography are presented in this section, as illustrated in Figure 5-4. They are (1) Isometric plot, (2) Contour map, and (3) Inverted isometric plot.

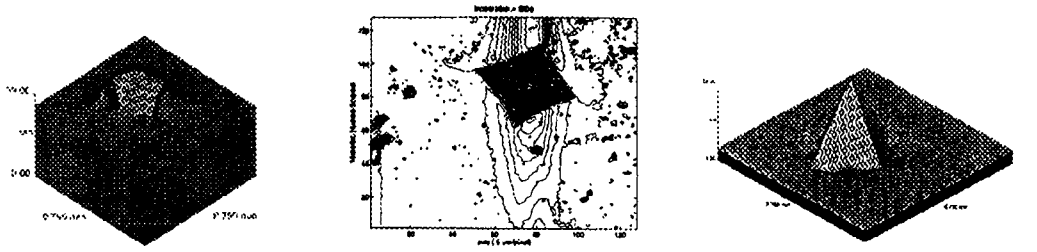

a) Isometric Plot b) Contour Plot c) Inverted Isometric Plot

Figure 4-4 Procedure of 3D Visualization using Image Processing

Figure 4-5a presents two 3D isometric plots of the indentations at 200g and 400g on the occlussal surface, respectively. The two 3D isometric plots shown in Figure 4-5b illustrate the same loading condition on the buccal surface. The basic topographic features of the indentation, namely the 'pile-up', 'sink-in', and the shape of the diamond of the microhardness tester, are observed from these isometric plots. These features give a vivid picture of the deformation process during indentation. In the occlusal case, the rods are perpendicular to the applied load and do not fracture. Thus, a high hardness value is obtained for the occlusal surface and a small amount of pile-up and sink-in volume is found for both indentations at 200g and 400g, as illustrated in Figure 4-5a. In the buccal; surface. the applied force acts at an angle to the rods, thus causing them to fracture and displace in various directions. The broken and mis-aligned rods appear in Figure 4-5b at the significant damage zone located on the edge of the impression, indicating possible shearing among the enamel rods due to its angular orientation nature on the buccal surface with respect to the loading condition. In addition, plastic flow of material forms 'pile-ups' and 'sink-ins'. The volume of these surface disturbances, as observed from Figure 4-5b, is relatively large if compared with the occlusal case.

Figures 4-6a and 4-6b present two contour plots taken from the three dimensional

indentation topographies as displayed in Figure 4-5. A total of forty equally-distant contour levels based on the total height of each indentation topography is used. The significant advantage of the contour plot of impression is that it provides information of a directional nature relating to the surface topography. It's important to notice the asymmetry of the indentation on both the occlusal and buccal surface. The asymmetry is an imprint of the inhomogenous response of the enamel rods matrix to the indentation loading. It suggests the disturbance produced in enamel is irregular. In Figure 4-6a, the asymmetry of the indentation on the occlusal surface is conformed to two main islands of pile-ups on two sides of the indentation. In Figure 4-6b, the asymmetry of the indentation on the buccal surface is more severe, as both fracture and deformation specifically developed on one side of the indentation impression.

In order to see the topographic details of the part of impression below the general level of the surface, two inverted isometric plots of the indentations on both occlusal and buccal surface are presented in Figure 4-7. These inverted plots exhibit the plastic deformation of the material. The pile-up is seen from the surrounding edges of the indentation. Just above the level of the surface, there is evidence of small amounts of sink-in before the shape of the indentation follows exactly the shape of the diamond indenter. From Figure 4-7a, a small amount of the sink-in volume of the impression is found on the occlusal surface. From Figure 4-7b, a much greater amount of the sink-in volume is revealed immediately above the edges of the indentation. It is interesting to note that a significant amount of fracture can be observed on one side of the indentation at 400g loading. This phenomenon can also be confirmed if the corresponding contour plot is examined. This fracture region could be due to the shearing of enamel rods during the indentation unloading cycle. Overall, the qualitative assessment of the indentation morphology using the atomic force microscope can be summarize in the Table 4-1.

Table 4-1. Summary of 3D Visualization Results

	Major Observations		
	Isometric Plot	Contour Plot	Inverted Isometric Plot
Usage	Visualization of basic properties, e.g., pile-up, sink-in, and the shape of impression indenter	Provides information of a directional nature relating to the surface topography	Exhibit the plastic deformation of thematerial below the level of the indentation impression
Occlusal Surface	1) Small amount of pile-up and sink-in volume is found for both indentations 2) The dominant mechanism is uniform plastic deformation of the material	1) The asymmetry of the indentation on the occlusal surface is conformed to two main islands of pile-ups on two sides of the indentation	1) A minimal amount of sink-in of the indentations is found on the occlusal surface
Buccal Surface	1) A large amount of pile-up volume is observed at one corner of the indent, indicating possible shearing of the enamel rods due to its angular orientation nature on the buccal surface	1) The asymmetry of the indentation on the buccal surface is more severe, as both fracture and deformation specifically developed on one side of the indent.	1) A much greater amount of sink-in is revealed immediately below the edges of the indentation. 2) A significant deformation zone is also found on one side of the indentation at 400g loading

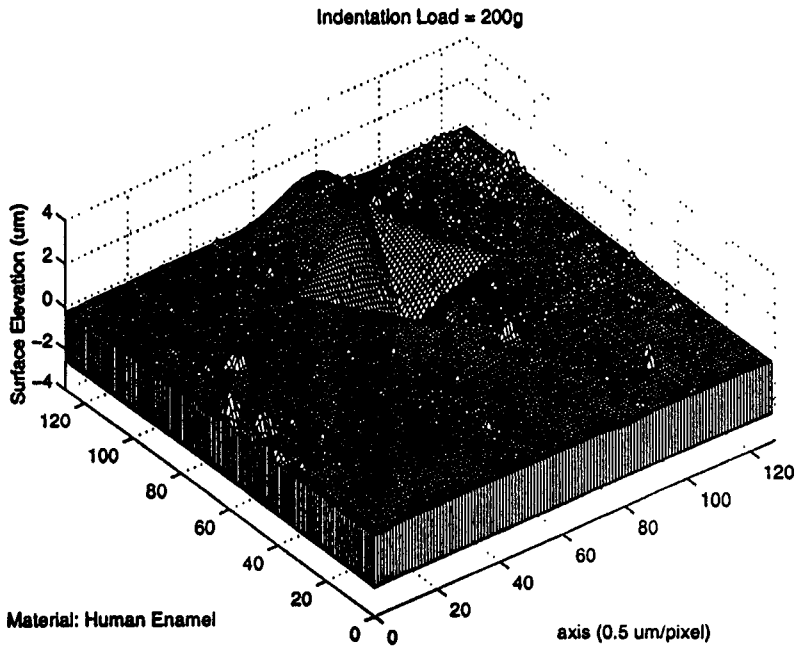

a) Indentation Load = 200 g

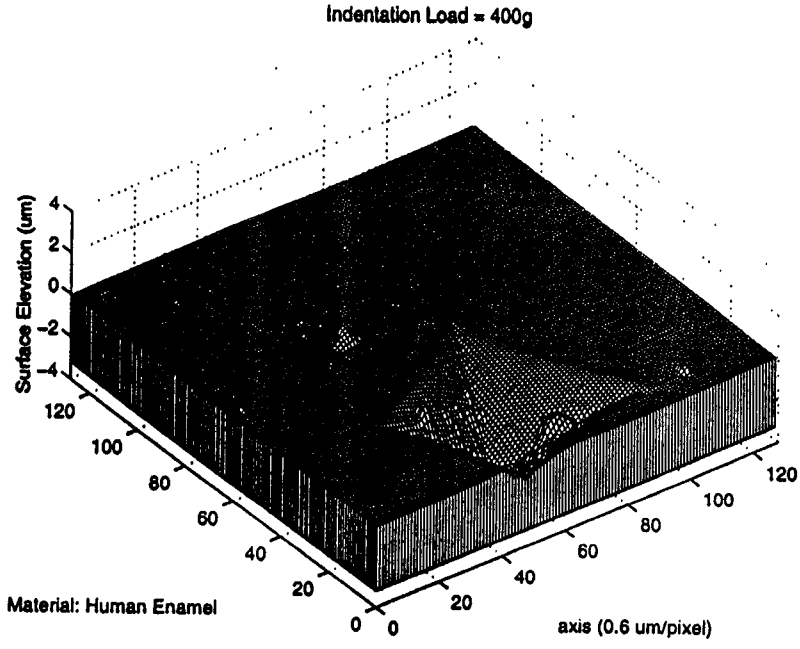

b) Indentation Load = 400 g

Figure 4-5a. Three Dimensional Topography Visualization of the Indents on the Occlusal Surface

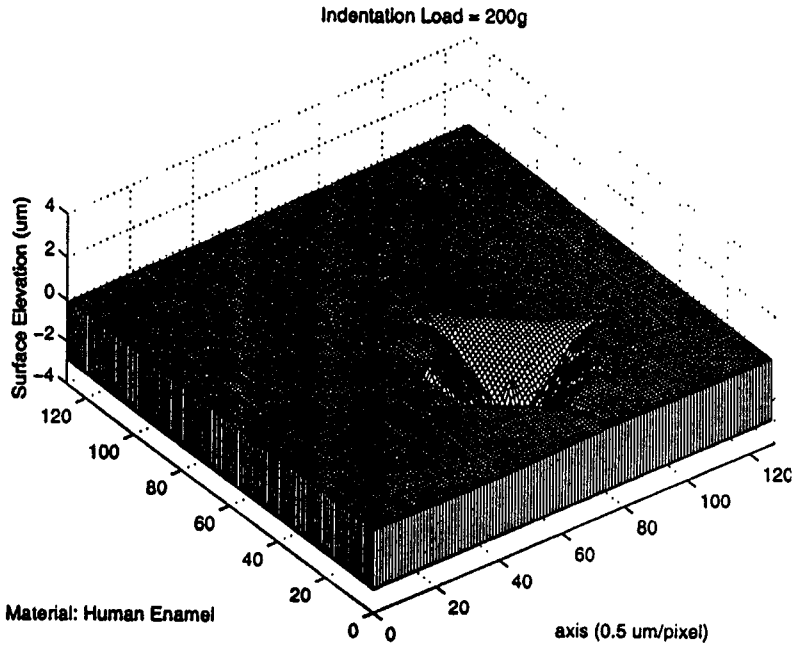

a) Indentation Load = 200 g

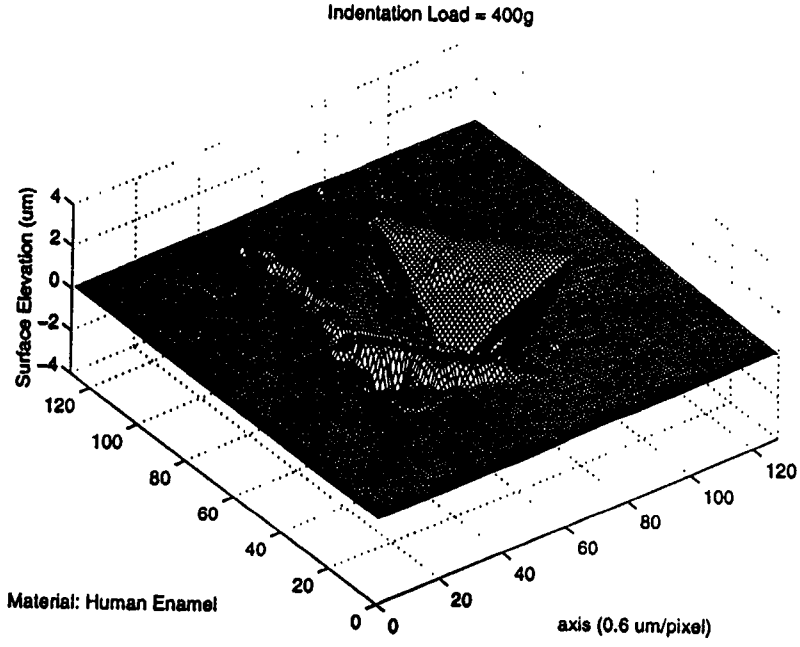

b) Indentation Load = 400 g

Figure 4-5b. Three Dimensional Topography Visualization of the Indents on the Buccal Surface

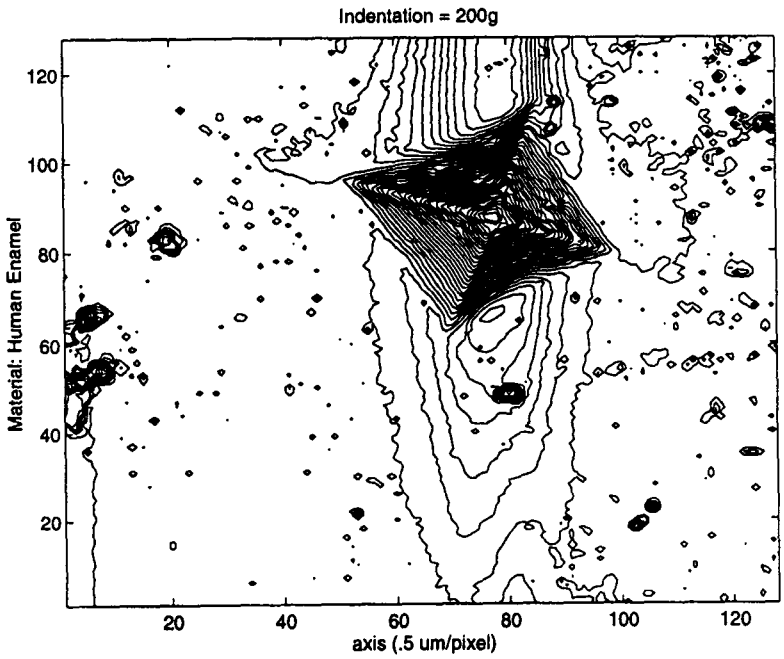

a) Indentation Load = 200 g

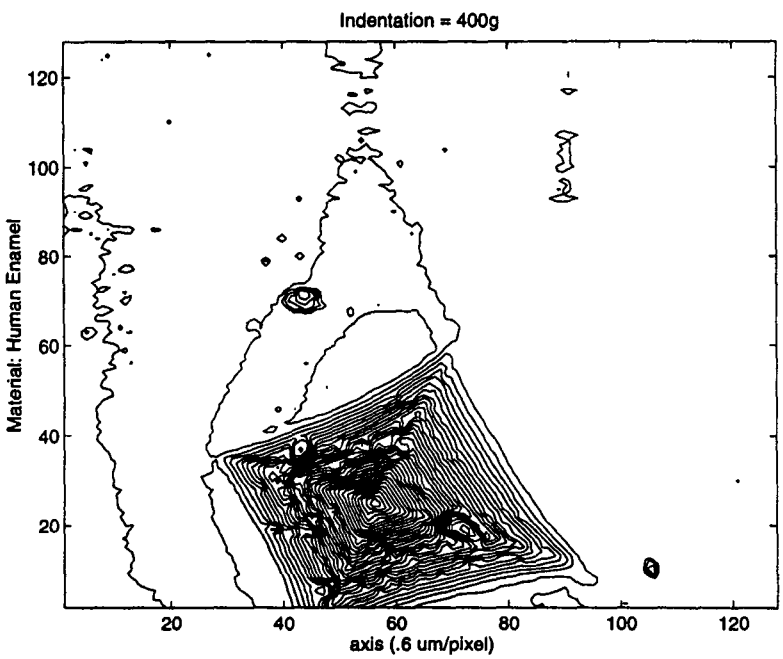

b) Indentation Load = 400 g

Figure 4-6a. Contour Maps of Microhardness Indentations on the Occlusal Surface

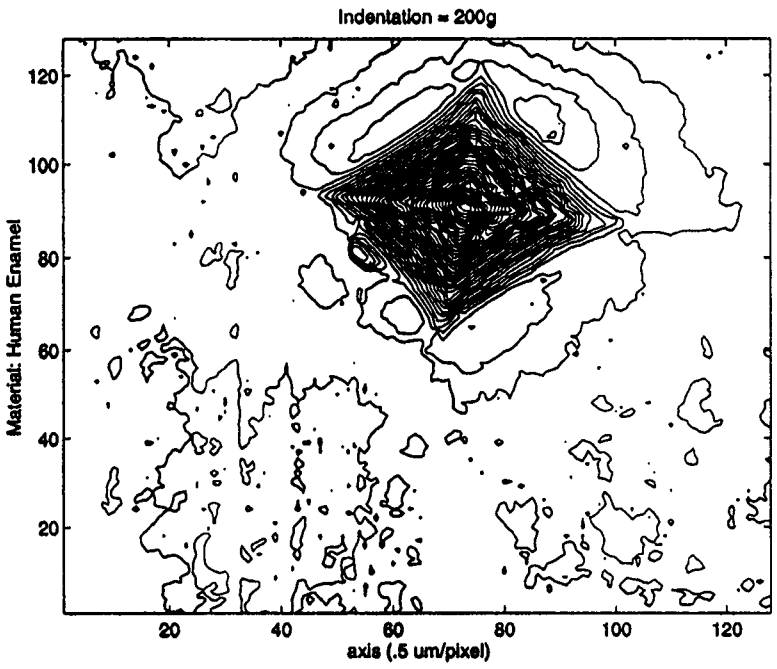

a) Indentation Load = 200 g

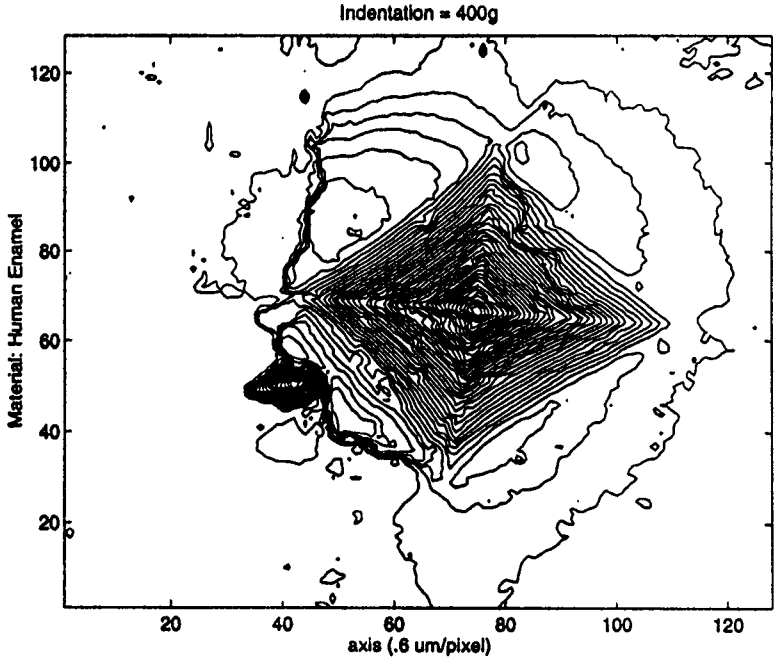

b) Indentation Load = 400 g

Figure 4-6b. Contour Maps of Microhardness Indentations on the Buccal Surface

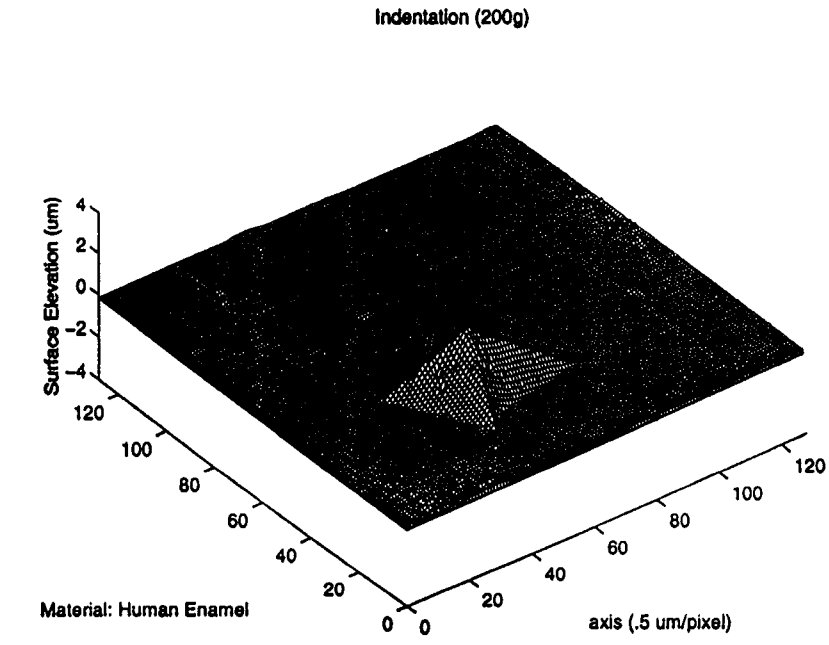

a) Indentation Load = 200 g

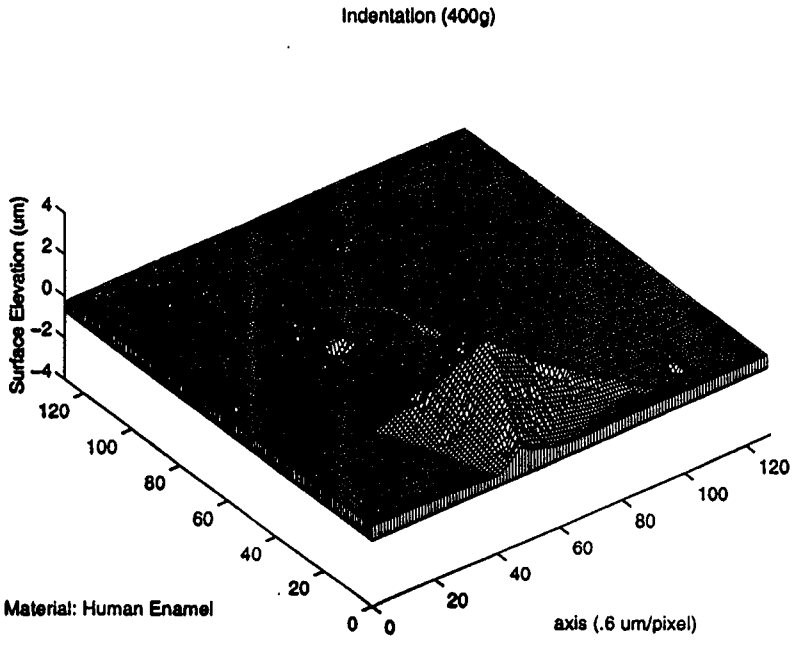

b) Indentation Load = 400 g

Figure 4-7a. Inversion Plots of Microhardness Indentation on the Occlusal Surface

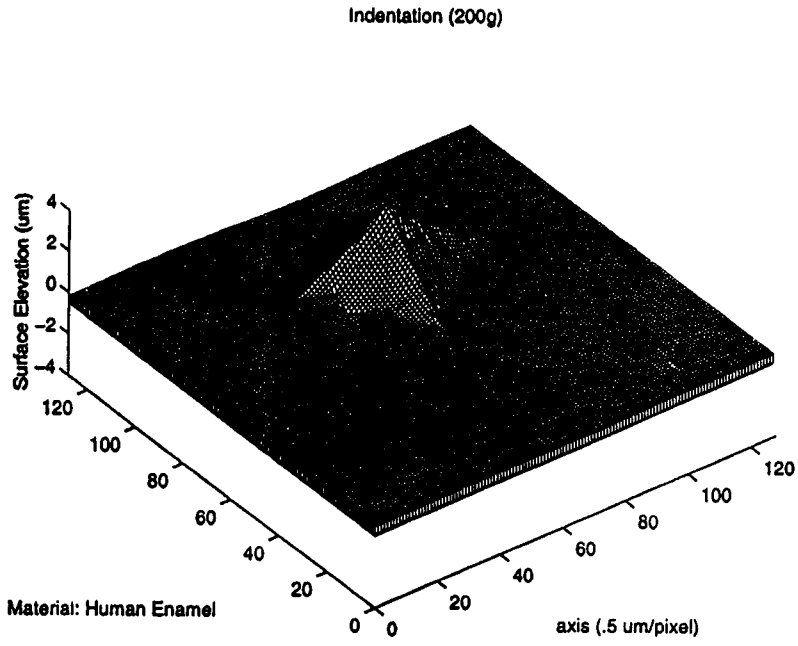

a) Indentation Load = 200 g

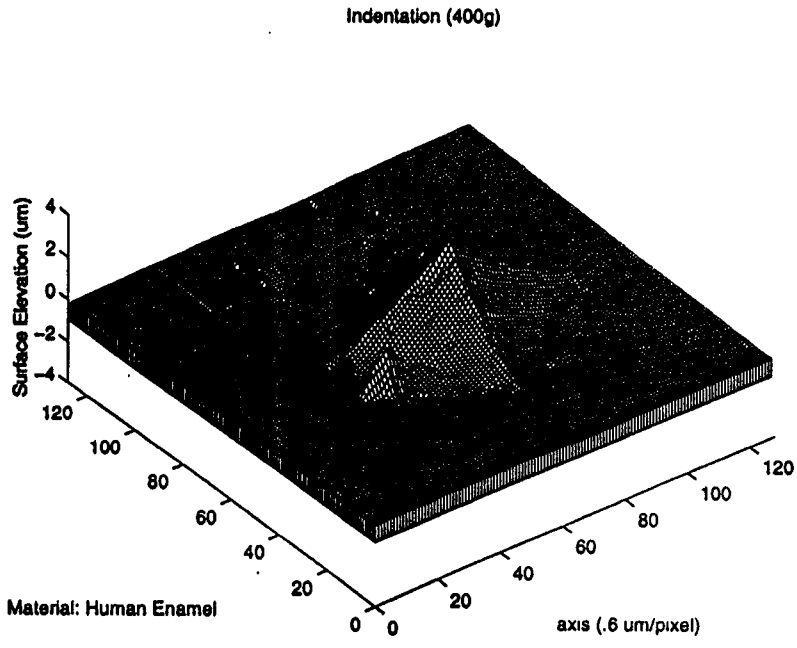

b) Indentation Load = 400 g

Figure 4-7b. Inversion Plots of Microhardness Indentation on the Buccal Surface

4.3.4 Discussion of Results

Information gained from the 3D visualization offers great opportunities to understand the physical process of hardness indentation. The digitized data obtained from the atomic force microscopy measurements form a basis to perform quantification of the hardness indentation process. The three aspects discussed in this paper are elastic recovery of the indentation impression in brittle material, characterization of plastic flow, and normalization of hardness measurements with respect to a selected loading condition.

4.3.4.1 Elastic Recovery in Brittle Material

To quantify elastic recovery at hardness indentations, a new parameter is defined as follows:

$$\text{Elastic Recovered Index} = \frac{\text{Predicted Depth} - \text{Measured Depth}}{\text{Predicted Depth}} * 100\% \qquad (4.1)$$

In this study, the elastic recovery is calculated as a ratio of the difference between the predicted and measured depths to the predicted depth. It is expressed as a percentage. Note that an assumption is made in this study to calculate the predicted depth. It is assumed that the dimension of indentation diagonal remains unchanged during the elastic recovery process. Based on the assumption, the predicted depth is given by

$$\text{Predicted Depth} = (\text{Indent Half Diagonal}) * \cot\psi \qquad (4.2)$$

where parameter ψ represents the semi-angle of the indenter. It is equal to 74° in this

study. It should note that the measured depth can be readily obtained by sorting the data in the depth direction and identifying the most negative number with respect to the reference planary surface, i.e.,

$$\text{Measured Depth} = \max \sum \text{abs}(\text{depth}_i) \tag{4.3}$$

Table 4-2 lists numerical values of the elastic recovery of hardness indentations. Data used for calculation are taken from the atomic force microscopy measurements for the two loading conditions of 200g and 400g for both occlusal and buccal surfaces.

Table 4-2. Results of the Indentation Height Parameters

	Occlusal Surface		**Buccal Surface**	
Load (g)	200g	400g	200g	400g
Measured Depth of Indentation(μm)	2.59μm	3.20μm	2.86μm	3.24μm
Theoretical Depth of Indentation(μm)	4.21μm	6.23μm	4.21μm	6.23μm
Elastic Recovered Index (%)	37%	49%	32%	48%

Examining the listed data, two important observations can be made. The first observation is that elastic recovery along the depth direction is significant at low loading conditions, such as 37% at 200g versus 49% at 400g for the occlusal surface. In fact this is true for both occlusal and buccal surfaces. The second observation is that the elastic recovery is more significant with the occlusal surface than the elastic recovery with the buccal surface, such as 37% versus 32% at 200g, and 49% versus 48% at 400g. However, such differences decrease as the loading condition increases. This is due to the

presence of a dominant crack system usually formed under high loading conditions.

4.3.4.2 Characterization of Material Plastic Flow

Material plastic flow can be characterized by the 'pile-ups' and 'sink-ins' formed during the indentation process. In this study, a parameter, denoted as pile-up height index, is introduced to characterize the formed 'pile-ups'. It is given by

$$\text{Pile - Up Height Index} = \frac{\text{Mean of the heights of pile - ups}}{\text{Predicted Depth of Indentation}} * 100\% = \frac{\frac{1}{n}\sum_{i=1}^{n} h_i}{\text{Predicted Depth of Indentation}} * 100\% \quad (4.4)$$

Table 4-3 lists numerical values of the pile-up height index for the hardness indentations used in Section (3.2). It is interesting to note that numerical values of the pile-up height index are relatively low, 3.5% at 200g and 3.6% at 400g, for the occlusal surface. On the other hand, numerical values are relatively high, 12.4% at 200g and 14.3% at 400g, for the buccal surface. This difference points out the effect of rod orientation with respect to the loading surface on the material plastic flow during indentation.

Table 4-3. Pile-up Height Index

	Occlusal Surface		**Buccal Surface**	
Load (g)	200g	400g	200g	400g
Mean Pile-up Height (μm)	0.15μm	0.23μm	0.52μm	0.89μm
Predicted Depth of Indentation(μm)	4.21μm	6.23μm	4.21μm	6.23μm
Pile-up Height Index (%)	3.5 %	3.6 %	12.4%	14.3%

In order to graphically characterize the material flow during indentation, a second parameter, called spread area index, is introduced. The parameter is defined by

$$[\text{Spread Area Index}]_i = \frac{\sum_x \sum_y \text{Solid Area within a Sliced x - y plane}}{\sum_x \sum_y \text{Total Area within a Sliced x - y plane}} \quad (4.5)$$

for i = 1, 2, 3, ... N where N represents the number of slices taken along the z- direction. Note the solid area is determined by the materialized area which results in the intersection of a sliced horizontal plane and the indentation impression. Table 5-4 lists numerical values of the spread area index on 10 sliced x-y planes.

Figure 4-8 presents two plots of the listed data. Note the curve in dark line, which represents an ideal indentation process without any 'pile-ups' and 'sink-ins'. The top part of the ideal curve has a slope, which characterizes the increase of indented area. The sudden drop portion indicates the sliced x-y plane is just passing the reference surface, on which 'pile-ups' are built in. The zero line is the characteristic of no any 'pile-ups' formed during indentation. Therefore, any deviation from the ideal curve is indication of material plastic flow. The deviation on the top portion represents 'sink-ins'. The deviation on the bottom portion characterizes 'pile-ups'. The closed area between the ideal curve and the measured curve represents the volume of material plastic flow, i.e.,

$$\text{Plastic Flow Volume} = \int_{z=0}^{\text{max pile-up height}} [g(z) - f(z)]\, dz \quad (4.6)$$

Table 4-4. Numerical Values of Spread Area Index

	Spread Area Ratio [%]									
Z-Direction Height (μm)	0.4	0.2	0	-0.2	-0.4	-0.8	-1.2	-1.8	-2.2	-2.6
Occlusal Surface (200g)	0.1%	0.3%	90.3%	93.9%	94.9%	96.7%	97.9%	99.2%	99.7%	99.9%
Buccal Surface (200g)	4.6%	9.4%	93.8%	94.8%	95.7%	97.2%	98.3%	99.4%	99.8%	99.9%
Occlusal Surface (400g)	.13%	0.9%	88.1%	90.1%	91.6%	94.4%	96.4%	98.2%	99.0%	99.6%
Buccal Surface (400g)	5.9%	14.7%	85.5%	90.2%	91.8%	94.3%	96.3%	98.3%	99.2%	99.7%

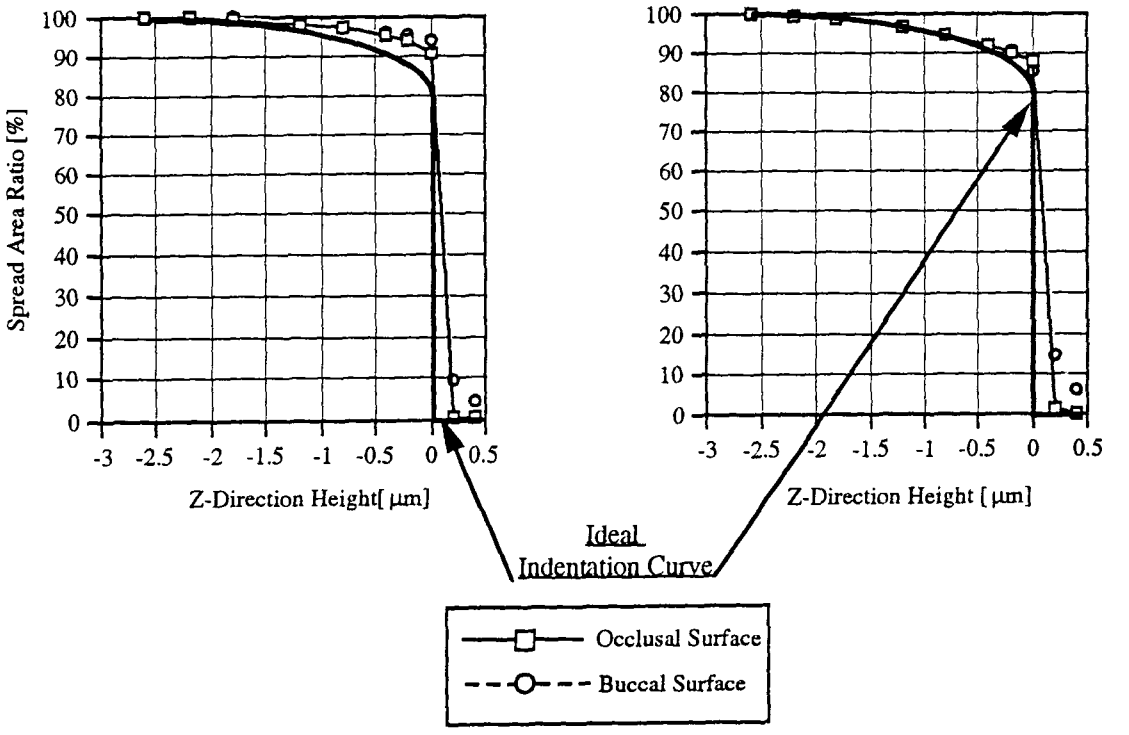

Figure 4-8. Graphical Illustration of Material Flow during Indentation

The two curves in Figure 4-8a represent the spread area index curved based on the calculations for both the occlusal and buccal surface at 200g. The two curves in Figure 4-8b represent a similar situation except the loading condition is at 400g. All the four

curves indicate that 'sink-ins' are much less significant than 'pile-ups' in the determination of plastic flow volume because the deviation on the top portion seems negligible if comparing it with the deviation on the bottom portion. Examining the two curves in either Figure 4-8a or Figure 4-8b, the total deviation for the occlusal surface is always less than that for the buccal surface. There are more 'pile-ups' formed, or more plastic flow, on the buccal surface than those formed on the occlusal surface. The material plastic flow volumes for the four cases are calculated using the integration formula, Equation 4.6, are listed as.

Rod orientation:	Occlusal Surface		Buccal Surface	
Loading:	200 g	400 g	200 g	400g
Plastic flow volume: [unit: 10^3 μm]	78	208	135	253

4.3.4.3 Normalization of Hardness Measurements

The hardness values measured under different loading conditions differ from each other significantly. As shown in the data listed in Table 4-1, the maximum number is 468 VHN at 50g and the minimum number 379 at 2000g for the occlusal surface. Therefore, telling a hardness number without giving the corresponding loading condition may not provide sufficient information on the hardness property of the material. Normalization of the hardness measurements made under different loading conditions with respect to a selected, or commonly acceptable, loading condition is needed.

If examining the formula used to determine the hardness value from measurement, such as Equation 4.1, a surprising fact is that the geometrical parameter used is the dimension of the impression diagonal. This parameter has the least effectiveness in characterizing the reversible deformation occurred during indentation. The credibility of determining hardness value without taking to account the reversible deformation, such as elastic recovery of the indentation depth, is in question.

In this study, a procedure to perform normalization and incorporate the reversible deformation into the hardness determination is proposed. Equation 1 is revised and two new parameters are introduced.

$$\text{Normalized Hardness} = \frac{1854 * P}{d^2} * \sqrt[4]{\text{Elastic Recovered Index}} * C \quad (4.7)$$

The first parameter is based on the elastic recovery index. Recognizing the non-linearity between the material hardness and elastic recovery, a fourth root is used. As an example to demonstrate the introduction of this parameter, the following data are before and after the normalization for the occlusal surface together with the four numerical values of elastic recovery index:

$$\text{Normalized Hardness} = \frac{1854 * P}{d^2} * \sqrt[4]{\text{Elastic Recovered Index}} \quad (4.8)$$

before normalization:	468	453	430	398
elastic recovery index	29%	25%	37%	49%
after normalization:	328	331	334	326

As indicated, the normalized hardness values are 328, 331, 333, and 326, that are very close to each other and vary slightly about 330 VHN. Numerical values of these four normalized hardness measurements may not seem reasonable if comparing their values measured before normalization. These values are 468, 453, 430, and 398, respectively. Therefore, there is a need to make an adjustment for the normalized hardness value be set at a given loading condition. Say the loading condition of 200g is selected. The parameter C in equation 8 can be set at the following value:

$$C = \sqrt[4]{3} = 1.316 \tag{4.9}$$

Using this correction factor to adjust the normalized hardness values will allow us to raise the average of the normalized hardness values to a new level. It is now at 430 VHN because the four normalized hardness values after adjustment are 431, 435, 439, and 429 VHN, respectively, as illustrated in Figure 4-9. Graphically speaking, such a normalization and adjustment process is to bend a curve to a horizontal line and then shift the line upward or downward. In this study, the shift value is 100 VHN.

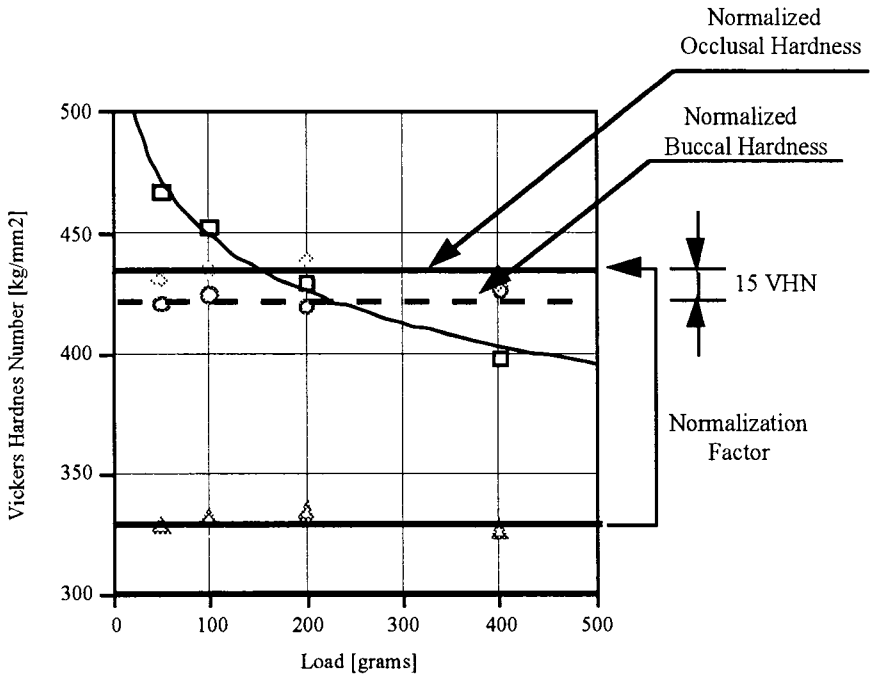

Figure 5-9. Illustration of Hardness Normalization

The significance of implication of this normalization process is two-fold. First, the normalized hardness values are determined not only by the applied load and the measured diagonals of the impression, but also by incorporating the reversible deformation into the hardness evaluation. As a result, the normalized hardness value will have a unique hardness value for a given type of ceramic material without specifying the loading condition under which a specific indentation test is performed.

The second contribution of this normalization process is the establishment of a criterion to use the hardness measurement as a tool for comparison among different ceramic materials. In this study, we obtained two curves, one for the occlusal surface and the other for the buccal surface. Using equation 8 and having parameter C set at 1.316, the normalized hardness value for the occlusal surface is 435 VHN, and the normalized hardness for the buccal surface is 420 VHN.

Therefore, comparison between the two normalized values clearly indicates that the hardness of the occlusal surface is higher than that of the buccal surface. The difference is about 6-10 %, mainly due to the orientation of rods with respect to the loading surface.

4.4 Summary

A research effort to perform a combined analytical and experimental study with focus on identifying crack fracture characteristics in microhardness indentation of human dental enamel. Significant findings are summarizes as follows.

1. Vickers Microhardness indentation using loading conditions, from 50g to 2000g has been performed on both occlusal and buccal surfaces in human enamel. Significant cracking fracture and deformation patterns have been observed.

2. A computer-based Scanning Electron Microscope and Atomic Force Measurement Analysis system has been used to perform surface height measurements of the indentation topography. These measurements are used to visualize hardness indentations using computer graphics software. Three types of visualization plots of the indentation have been presented, 1) isometric plot, 2) contour map, and 3) inverted isometric plot, providing a vivid picture and rich information into the material fracture and deformation during the indentation process.

3. Quantitative indices, such as the pile-up height, material spread area, and pile-up volume have been introduced to serve as performance indices to evaluate the material property of human enamel material. Results from this study affirm that

difference in enamel rod orientation contributes to variation of hardness characteristics and modify the cracking mechanism in an intrinsic way.

4. A new formula to determine microhardness values for indentation tests is proposed in this research. By incorporating elastic recovery into evaluation, a normalized hardness measurement can be achieved to associate a given type of ceramic material with a unique hardness value. This approach offers a unique opportunity to use hardness measurement as a means for comparison and other investigations related to material hardness characteristics.

Chapter 5

Machining Experiments

5.1 Introduction

The brittle nature of ceramics makes them difficult to machine. This chapter presents the effort made in machining ceramic specimens to be used for surface integrity assessment. These experiments are important because results from these experiments form a basis to explore the possibility of using hardness tests as an effective means for machinability evaluation.

Recognizing the unique stress-corrosion-cracking behavior of ceramic material under certain aggressive environments, an apparatus is employed to create a machining environment where workpiece and cutting tool are submerged in a bath filled with cutting fluids. The obtained results suggest that the chemo-mechanical interactions occurred during machining have great influence on the stress distribution produced in the ceramic material being machined, thus having direct effects on crack initiation and propagation. By controlling the machining parameters, higher material removal rate with less surface damage can be achieved, showing the potential of submerged machining as an innovative technology for machining ceramic material

The material selected for the milling tests in this thesis study is DICOR/MGC, a machinable glass ceramic material. For dental restorations, a particularly important consideration is the closeness of physical properties of the restorative material to that of human enamel. Overall, in terms of translucency, thermal conductive, density, and hardness, DICOR/MGC closely resembles the physical properties of human enamel. In addition to

having a material removal rate close to that of human enamel when compared to other advanced ceramic materials, experimental studies indicated that DICOR/MGC wore at higher rate than human enamel.

5.2 Design of Experimentation

In order to carry out a systematic study, three important aspects regarding machining are considered. They are type of materials, machining environment, and machining parameters. To keep the number of machining tests at a manageable level, the first step is to narrow the search space, or to identify a feasible region. The criterion used for this investigation is 2 μm of the finish quality of machined surfaces.

5.2.1 Selections of Ceramic Material and Tool Material

In this thesis research, the ceramic material used is Dicor-MGC. It is a two phase tetrasilicic mica glass-ceramic material and has a micro structure consisting of mica flakes of approximately 70 volume percent dispersed in a non-porous glass matrix. The hardness of Dicor-MGC is about 3.4 GPa. The cleavage fracture along the planes of mica flakes makes the material machinable. Dicor-MGC has been widely used as a new material in dental restorations. Figure 5-1 illustrates the specimen used in the machining tests. It is a 152.4 mm long bar with a rectangular cross-section, each side equal to 12.7 mm. The material of the end mill selected was high speed steel with hardness of about 18 GPa, which is 5 times as hard as the Dicor-MGC material under the investigation.

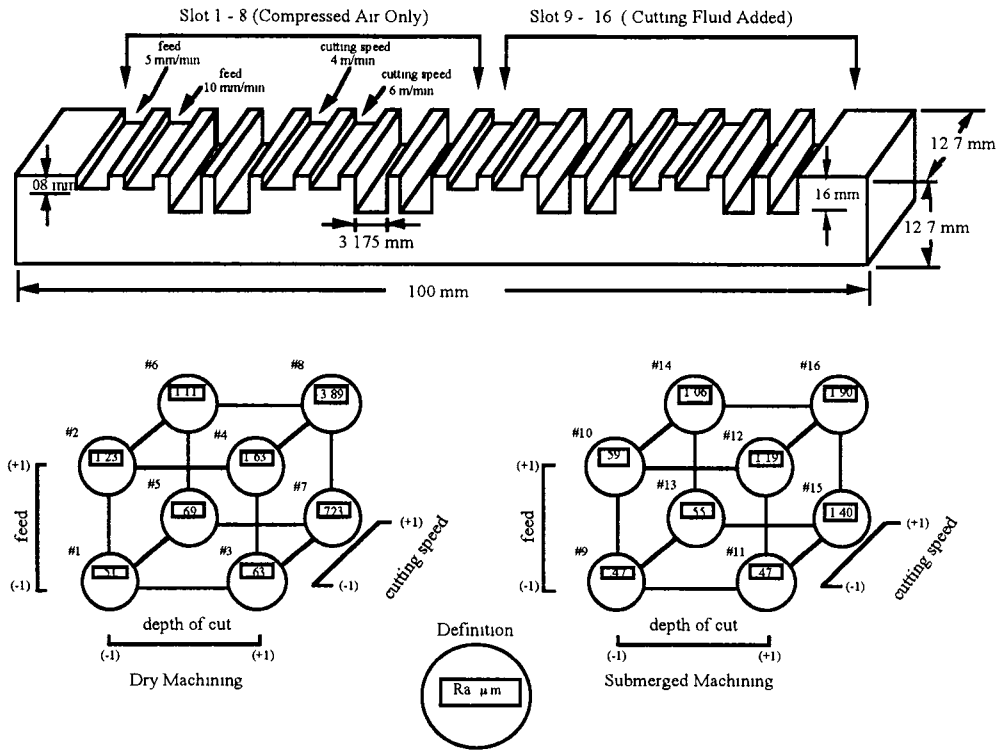

Figure 5-1 Ceramic Specimen and Setting of Machining Conditions

5.2.2 Machining Parameter Settings

The four machining parameters selected for this thesis research are type of the cutting fluid used, and three machining parameters. They are depth of cut, feed and cutting speed. A design of experimentation method is used to set each of the four variables at two levels, namely, high and low. Table 5-1 lists the 16 combinations of these four parameter settings. A graphical representation of this experiment design is illustrated by the two cubics shown in Figure 5-1. For example, the circle located in the front and right corner represents the machining condition set for Test 1, which is a combination of depth of cut = 0.08 mm, feed = 5 mm/min, and cutting speed = 4 m/min at a dry cutting environment where compressed air is used to assist in chip removal. On the other hand, the machining

condition set for Test 8 is a combination of depth of cut = 0.16 mm, feed = 10 mm/min, and cutting speed = 6 m/min at a dry cutting environment. Note the machining environment for Tests 1 - 8 where no cutting fluid is used. Therefore, the machining is under a dry environment. On the other hand, the machining environment for Tests 9 - 16 where cutting fluid is used. The fluid used in this investigation is a commercially available emulsifiable oil, called LS-A-14H [11]. The emulsifiable concentrate is mixed with water in a ratio of 9:1. The pH ranges from 9.7 to 9.9. To carry out these experiments, an NC program is prepared to carry out the machining tests, first at the dry environment, and then at the submersion environment.

Table 5-1 Design Matrix for the Experimentation and Measured Data

Test No.	Paramter Settings				Surface Roughness (μm)
	Feed [mm/min]	Depth of Cut [mm]	Cutting Speed [m/min].	Machining Environment	
1	5 (-1)	0.08 (-1)	4 (-1)	Dry Machining	0.51
2	10 (+1)	0.08 (-1)	4 (-1)	Dry Machining	1.23
3	5 (-1)	0.16 (+1)	4 (-1)	Dry Machining	0.63
4	10 (+1)	0.16 (+1)	4 (-1)	Dry Machining	1.63
5	5 (-1)	0.08 (-1)	6(+1)	Dry Machining	0.69
6	10 (+1)	0.08 (-1)	6(+1)	Dry Machining	1.11
7	5 (-1)	0.16 (+1)	6(+1)	Dry Machining	0.72
8	10 (+1)	0.16 (+1)	6(+1)	Dry Machining	3.89
9	5 (-1)	0.08 (-1)	4 (-1)	Submerged Mach	0.47
10	10 (+1)	0.08 (-1)	4 (-1)	Submerged Mach	0.59
11	5 (-1)	0.16 (+1)	4 (-1)	Submerged Mach	0.47
12	10 (+1)	0.16 (+1)	4 (-1)	Submerged Mach	1.19
13	5 (-1)	0.08 (-1)	6(+1)	Submerged Mach	0.55
14	10 (+1)	0.08 (-1)	6(+1)	Submerged Mach	1.05
15	5 (-1)	0.16 (+1)	6(+1)	Submerged Mach	1.4
16	10 (+1)	0.16 (+1)	6(+1)	Submerged Mach	1.9

5.3 Experimental Setups

In order to explore the potential for chemically-assisted machining of ceramics, a special apparatus is employed to carry out the machining tests. It is illustrated in Figure 5-2. By holding a sufficient amount of cutting fluid, the machining is under a submersion condition. The apparatus consists of three parts, namely, a container for cutting fluid, a vice to hold the workpiece, and a base on which strain gages are mounted for the purpose of measuring the cutting force during machining. During the machining tests, the apparatus is fixed on the table of a CNC machining center. The workpiece is tightened in the vice before the filling of cutting fluid. The cutting tool used in this investigation is an end mill with diameter equal to 3.175 mm.

A Matsuura MC-570 Machining Center -- a state-of-the-art computer numerical control (CNC) machine -- in the Advanced Design and Manufacturing Laboratory, is used for end milling operations. Specifically, a 2 level - 3 factor factorial design experiment is performed to assess the machinability of DICOR/MGC dental ceramic material. As illustrated in Figure 5-1, the three factors of interest are feed (factor F), spindle speed (factor S), and depth of cut (factor D). Note that a full axial depth of cut is taken for all experiments, i.e., the radial depth of cut is entirely governed by the diameter size of the end mill. The high and low levels for each of the variables are listed in Table 5-2.

roughness average, R_a, are obtained. They are listed in Table 5-1

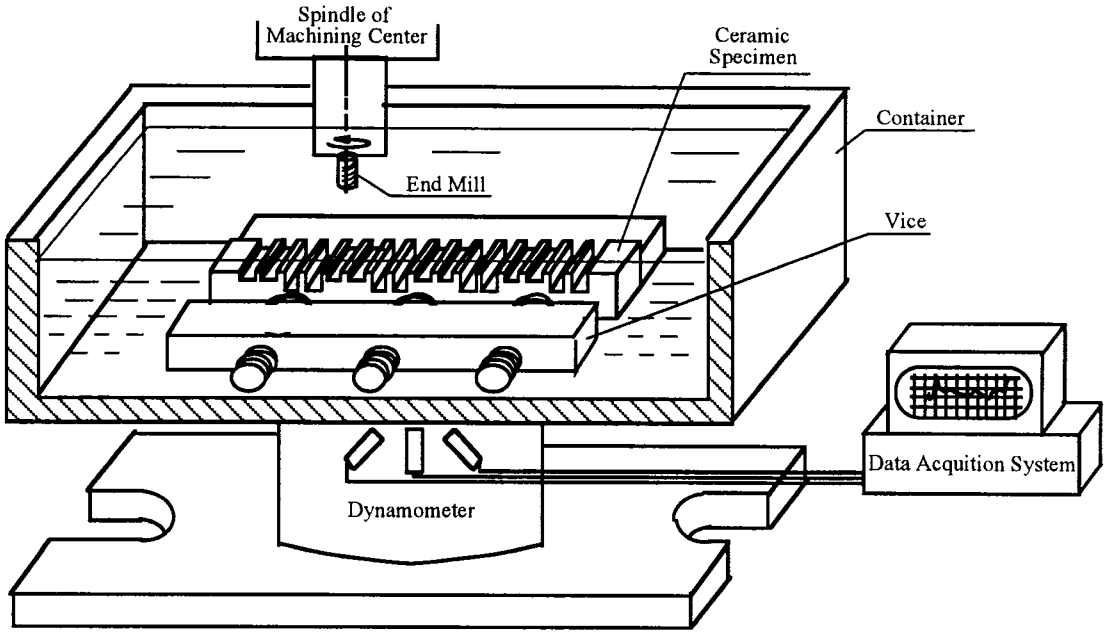

Figure 5-2 Submerged Machining Apparatus

5.4 Assessment of Experimental Data

Assessment of experimental data obtained from this investigation is based on the requirements of 2 μm of the finish quality of machined surfaces. It is believed that the smoother the surface produced, the less likely it is damaged sufficiently to compromise its clinical performance. In addition, quantitative information on the degree of damage which has been induced to the ceramic material during the preparation is essential to the assessment of machining performance. Observations indicate that most of the ceramic components failure occurred during service initiate at the surface cracks, which grow and penetrate, leading to unstable failure.

The assessment performed in this investigation focus on surface finish. In this study, the traditional surface profilometer method, Perthometer-S5P (resolution 40×10^{-9} m), is used. Traces from each of the 16 machined surfaces are taken, and values of roughness average, R_a, are obtained. They are listed in Table 5-1.

5.5 Analysis of Experimental Results

Data obtained from a factory design, such as the one used in this investigation, offers an unique opportunity to derive empirical models capable of describing effects of the four parameters on the machining performance.

5.5.1 Main Effects of the Four Machining Parameters

Using the algorithm, proposed by Box[3], averaging the 8 pairs of roughness measurements for each of the four machining parameters provides an estimate of the main effect of each of the four parameters on finish quality in terms of surface roughness. For example, the main effect of the machining environment can be identified by,

$$\frac{1}{2}\left[\frac{0.47+0.59+0.47+1.19+0.55+1.05+1.40+1.90}{8} - \frac{0.51+1.23+0.63+1.63+0.69+1.11+0.72+3.89}{8}\right] = -0.18 \quad [\text{unit}: \mu\text{m}] \qquad (5.1)$$

In a similar manner, the three main effects of feed, depth of cut, and cutting speed can also be obtained. An empirical model to describe the main effects of these four parameters on finish quality is represented by

$$\bar{R}_a = 1.13 + 0.45(\text{feed}) + 0.35(\text{depth of cut}) + 0.28(\text{cutting speed}) - 0.18(\text{machining Environment}) + (\text{combinational effects}) \quad [\text{unit}: \mu\text{m}] \qquad (5.2)$$

Note that the first term in Equation (5.2), 1.13 mm, is the grand average, or the average of the 16 R_a measurements, serving as an indication of the order of surface finish under this investigation, which is about 1 mm. When using Equation (5.2), numerical

values of the four parameters used for prediction have to be either (+1) representing a high level setting or (-1) representing a low level setting. For the qualitative parameter representing the machining environment, (-1) means dry machining and (+) submerged machining. For example, replacing all the parameters by (-1) in Equation (5.2) corresponding to a combination of using smaller depth of cut, smaller feed, lower cutting speed, and a dry machining environment.

Examining Equation (5.2), the four values associated with the four machining parameters characterize their main effects on the surface finish. The three positive values indicate that large R_a values, or a degrading trend of surface Finnish, can be anticipated when feed, depth of cut and cutting speed are set at the high level. On the other hand, the negative value, -0.18 mm, is associated with the machining environment parameter, strongly indicating the benefit of improving finish quality. The ratio of 0.18 to 1.13 quantifies a 16% of reduction from the mean Level of roughness average when the submersion is being used to machine the Dicor-MGC material.

5.5.2 Interaction Effects between and/or among the Four Parameters

The benefit of using submerged machining can be further exploited when the experimental results are analyzed in two separated sets, one with the dry machining environment and the other with the submerged machining environment. For each data set, the grand average, main effects, and combinational effects among feed, depth of cut, and cutting speed are calculated to obtain the two empirical models:

For the dry machining environment:

$$\bar{R}_a = 1.30 + 0.66(\text{feed}) + 0.42(\text{depth of cut}) + 0.30(\text{cutting speed}) + 0.38(\text{feed x depth of cut}) + 0.23(\text{feed x cutting speed}) + 0.29(\text{depth of cut x cutting speed}) + 0.31(\text{feed x depth of cut x cutting speed}) \quad [\text{unit : } \mu\text{m}] \tag{5.3}$$

For the submerged machining environment:

$$\bar{R}_a = 0.95 + 0.23(\text{feed}) + 0.29(\text{depth of cut}) + 0.27(\text{cutting speed}) + 0.08(\text{feed x depth of cut}) + 0.02(\text{feed x cutting speed}) + 0.14(\text{depth of cut x cutting speed}) - 0.08(\text{feed x depth of cut x cutting speed}) \quad [\text{unit : } \mu\text{m}] \tag{5.4}$$

Examining the eight values representing the grand average, main and combinational effects in Equation (5.3) and (5.4), important observations are

(1) The numerical values in Equation (5.4), or associated with the submersion, are significantly smaller that those in Equation (5.5), indicating that a better surface finish condition can always be expected when the submersion is applied. This can be further confirmed when examining the data presented in the two cubics shown in Figure 5-1. For the identical machining parameter settings, the roughness value for test 1 is 0.51 μm for the dry machining, larger than 0.49 μm for test 9 under the submerged machining, 1.23 μm for test 2 which is larger than 0.47 μm for test 10, and so on.

(2) The influence contributed by the submerged machining to improve finish quality is unevenly distributed to the eight effects estimated from the experimental data. Figure 5-3 presents a comprehensive picture to illustrate such distribution. The most significant reductions are associated with the combinational effect between feed and depth of cut, the combinational effect between feed and cutting speed, and the

combinational effect among feed, depth of cut, and cutting speed. Those reductions almost eliminate these effects on degrading the finish quality statistically. Significant reductions includes the grand average, the main effect of feed, the main effect of depth of cut, and the combinational effect of depth of cut and cutting speed. The least reduction, which is 10%, is associated with the main effect of cutting speed. Statistically the following formula depicts the relationship between the roughness average of a machined surface and the three machining parameters under the submerged machining:

$$\bar{R}_a = 0.95 + 0.23(\text{feed}) + 0.29(\text{depth of cut}) + 0.27(\text{cutting speed}) + 0.14(\text{depth of cut x cutting speed}) \quad [\text{unit} : \mu m] \tag{5.5}$$

The explicit format of Equation (5.5) is an indication of the involvement of the stress-corrosion-cracking behavior of ceramic material in the process of material removal during machining.

(3) Because of the interplay between depth of cut and cutting speed, a combination of low cutting speed and low depth of cut may result in finish quality which is very compatible with the finish quality obtainable under the combination of low cutting speed and high depth of cut. This observation may bring practical interest that, when the submersion is applied, a combination of low cutting speed and large depth of cut could offer a higher material removal rate under the assumption of keeping satisfied finish quality of the machine surface.

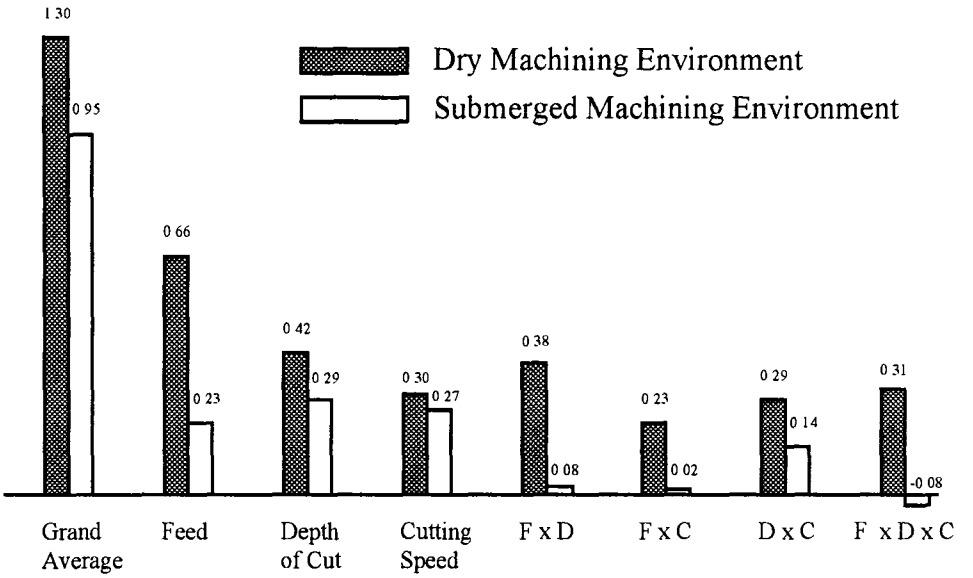

Figure 5-3 Comparison of Estimated Effects Between the Dry and Submerged Machining Environments

Chapter 6

Assessment of Surface Texture and Edge Effects

6. 1 Introduction

Two major aspects of the surface response in machining of DICOR/MGC glass ceramic will be studied using the computer-based surface characterization system described in Chapter 4. They are the surface texture formation and the edge effect. Both aspects are crucial in achieving the final goal of the dental research, a high quality ceramic crown replacement. Surface texture is critical in the study of surface and sub-surface damage under the brittle regime of ceramic machining. Formation of microcracks can greatly degrade the strength and toughness of ceramic part in service. On the other hand, the study of edge effect focuses on the control of geometric and dimensional accuracy of the machined part, which is critical in realizing the shape of the human dental restoratives.

6.2 Surface Texture Formation

Surface texture formation during machining is determined by a combinational effect of the kinematics of a cutting tool during machining and the geometric shape of the cutting tool. Figure 6-1a is an illustration where an image is taken from a milled surface. The part material is aluminum. In Figure 6-1a, the tool path trajectory during machining is clearly depicted because of plastic deformation in the material removal process. Figure 6-1b is also an image taken from a milled surface. However, the part material is Dicor, a new type of ceramic used for dental restorations. Examining Figure 6-1b, the tool path trajectory during machining can also be seen. Note the magnification scale used in

Figure 6-1b. The scale was 250x, which is more than 10 times than the scale used in Figure 6-1a. The image represents an area covering 0.19 x 0.19 mm^2 on the machined surface. According to the end mill kinematic motion during machining with the listed machining parameter settings, there are 44 trajectories on display with an approximately 4.3 μm distance away from each other.

Results from our earlier study on the chip formation process indicate that chip fragments collected during machining can be distinguished as two types. The first type of chip is denoted as machined chip, i.e., the chip formation is contributed to direct contact between the ceramic material being machined and the rake face of the cutting tool. Plowing marks observed on the back of chip speak the signify flow on the rake face under plastic deformation.

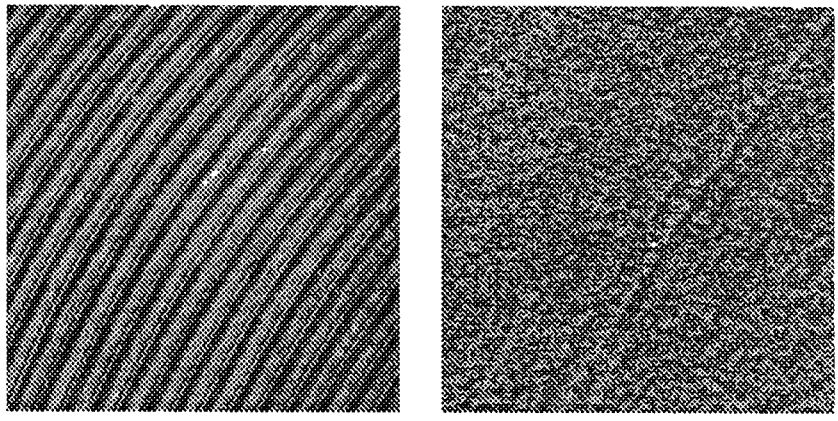

Ra =	1 64 μm	Ra =	0 94 μm
Area =	1 768 mm^2	Area =	0 0369 mm^2
Magnification =	20 x	Magnification =	250 x
End Mill Flute No =	2	End Mill Flute No =	2
Feed Rate =	180 mm/min	Feed Rate =	5 mm/min
Spindle Speed =	800 r p m	Spindle Speed =	600 r p m
Depth of Cut =	1 3 mm	Depth of Cut =	0 5 mm

(a) Metal (Aluminum) (b) Ceramic (Dicor)

Figure 6-1 Comparison of the Formed Tool Path Trajectory

The second type of chip is denoted as fractured chip, i.e., all the surfaces surrounding the chip fragment are fractured surfaces. There is no evidence indicating any direct contact between the tool rake face and the chip fragment during the machining. The process of

forming the fractured chip is a result of crack initiation and propagation, either in intergranular and/or transgranular forms.

6.2.1 Machining Tests

The preparation of specimens with machined surfaces is illustrated in Figure . 6-2. An end mill with a diameter of 3.175 mm cuts two blocks of 12.7 x 12.7 x 44.5 mm^3. On each of the two blocks, four slots are machined under four different conditions. The four different machining conditions for slots 1-4 are combinations of two feedrate settings (5 and 10 mm/min) and two spindle speed settings (600 and 900 rpm) with the depth of cut set at 0.5 mm [16]. When preparing slot 5-8, the feedrate and spindle speed settings remain unchanged, but the depth of cut is set at 0.25 mm.

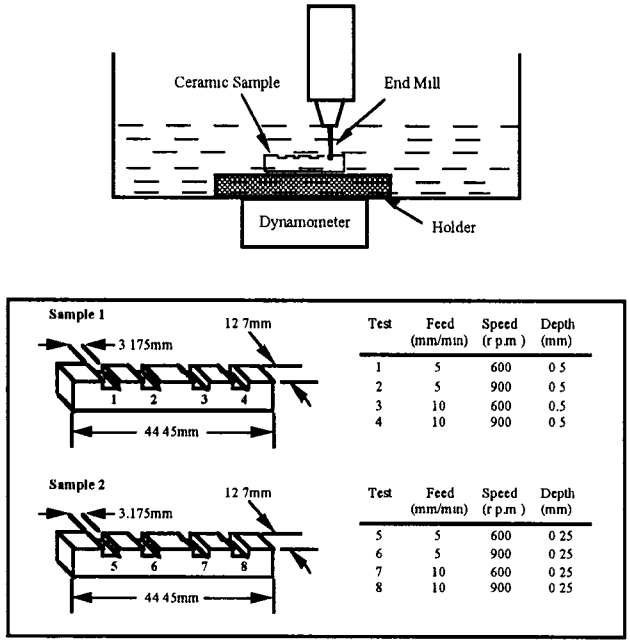

Test	Feed (mm/min)	Speed (r p.m)	Depth (mm)
1	5	600	0 5
2	5	900	0 5
3	10	600	0.5
4	10	900	0 5

Test	Feed (mm/min)	Speed (r p.m)	Depth (mm)
5	5	600	0 25
6	5	900	0 25
7	10	600	0 25
8	10	900	0 25

Figure 6-2. Preparation of Specimens with Machined Surfaces

The specimens after machining re examined using ElectroScan E-3 Environmental Scanning Electron Microscope. Figure 6-3 presents eight representative SEM

micrographs obtained through image processing. Each of these eight graphs contains 125 pixels by 125 pixels, representing a scanning area of 0.10 x 0.10 mm^2. The image data is then transformed into height variation data using a defined calibration relation between the intensity of electron reflection and the micro-scale surface graduation. Figure 6-4 presents two surface topographs reconstructed in the three-dimensional space after the data transformation.

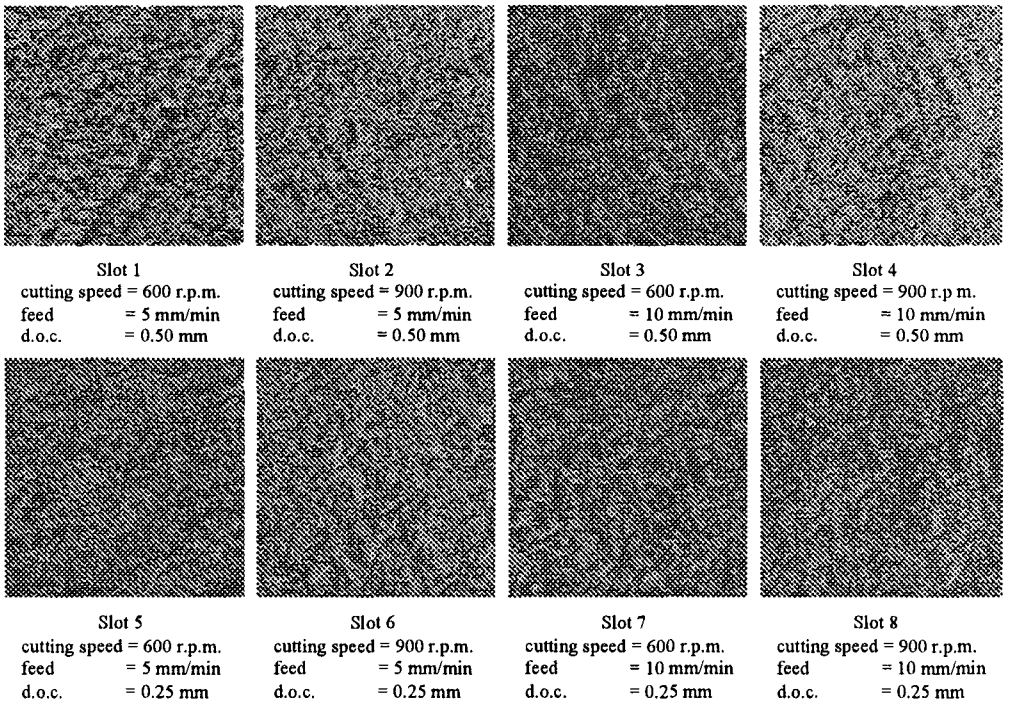

Figure 6-3. SEM Micrographs of Milled Surfaces of Dicor Specimen (Area = 0.10 mm x 0.10 mm)

6.2.2 Assessment of Surface Roughness

Traditionally, surface texture formed during machining is examined using profilometers. By taking profiles, surface characterization indices, such as roughness average and peak-to-valley, are evaluated from the measured heights along the

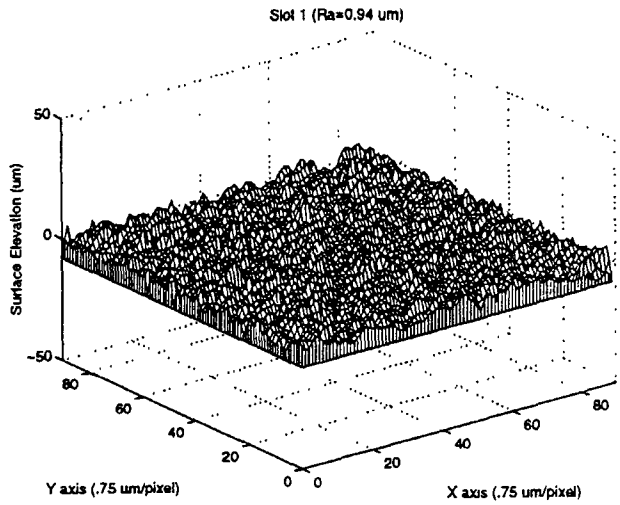

(a) Machined Surface (Slot 1)

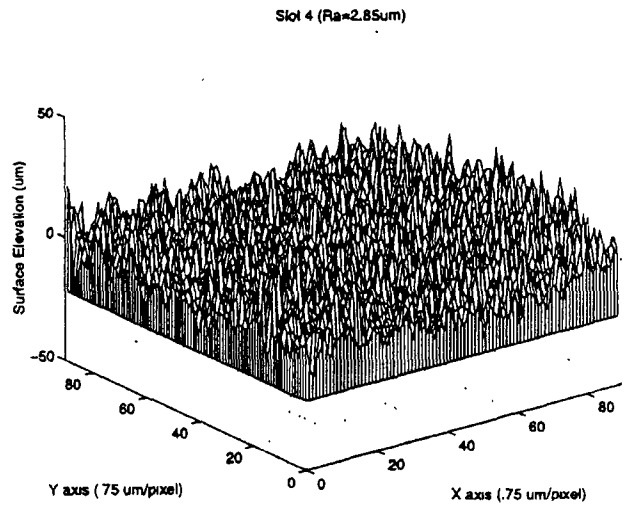

(b) Machined Surface (Slot 4)

Figure 6-4. Reconstructed Surface Topography

profiles. Figure 6-5 presents four profiles which are constructed using the data stored in the height variation data file. The two profiles with R_a= 0.83 and 0.88 μm in Figure 6-5a represent the surface roughness condition of slot 1 and the two profiles with R_a = 3.25 and 2.97 μm in Figure 6-5b are representations of slot 4. Note the "cut-off length", which

is 0.68 μm, used in the roughness average evaluation. It is 0.68 μm, representing a total of 90 data

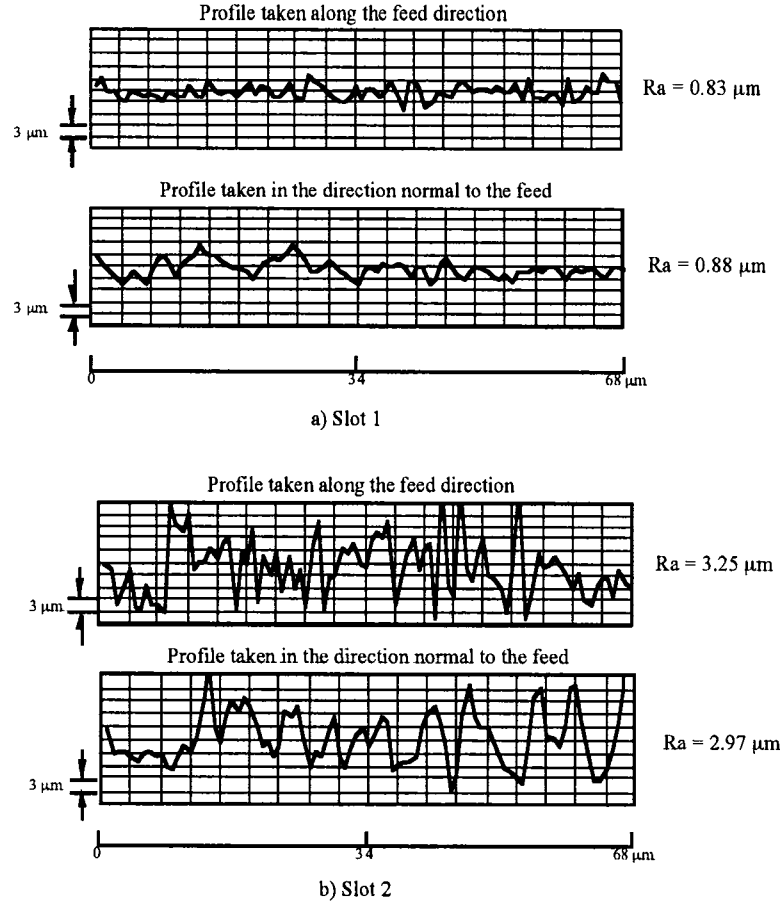

Figure 6-5. Profiles Reconstructed from Height Variation Data Files

(pixels) used in the evaluation. Table 6-1 lists the roughness average values evaluated from the eight machined surfaces. The smallest R_a value is 0.21 μm associated with slot 8. The corresponding machining conditions are feedrate: 5 mm/min, spindle speed: 600 rpm, and axial depth of cut: 0.25 mm. Numerical values of the standard deviation are also presented in Table 6-1, indicating the variation range of the R_a evaluation. Generally speaking, a large R_a mean value is associated with a large value of the R_a standard deviation.

Table 6-1 Results of Ra Evaluation

Slot Number	1	2	3	4	5	6	7	8
Ra (μm)	0.94	0.80	2.85	1.73	1.43	0.53	1.21	0.21
Standard Deviation (μm)	0.03	0.03	0.13	0.15	0.11	0.04	0.09	0.03

6.2.3 Examination of the Assembled Contour Maps

Examining Figure 6-4, the two reconstructed surface topographies represent visualization of machined surfaces. The surface texture shown in Figure 6-4a characterizes the machined surface on slot 1 and the surface texture shown in Figure 6-4b characterizes the machined surface on slot 4. A comparison of the two surface topographies gives a vivid picture showing how the two surface textures are different from each other. The surface condition on slot 4 is much rougher than that on slot 1 because it has higher peaks and deeper valleys.

Note the scale used in the visualization. In the marked X and Y axes, each pixel represents 0.75 μm, and the indicated 80 pixels represent a length of 60 μm. The unit of the vertical axis is micrometer. To quantify the surface texture, contour plots are taken at six levels on the vertical direction. They are 2.0 μm, 1.5 μm, 1.0 μm, 0.5 μm, 0 μm, and -1.0 μm with the level of 0 μm representing the reference plane used for the R_a evaluation, as illustrated in Figure 6-4. Figure 6-6 presents two contour maps. Figure 6-6a is the contour map representing slot 1. The contour map is an assembly of the six contour plots at the six indicated height levels taken from the surface topography shown in Figure 6-4. Similarly, Figure 6-6b is the contour map representing slot 4. On these contour maps, the grain size of 2 μm is also indicated as reference for examination.

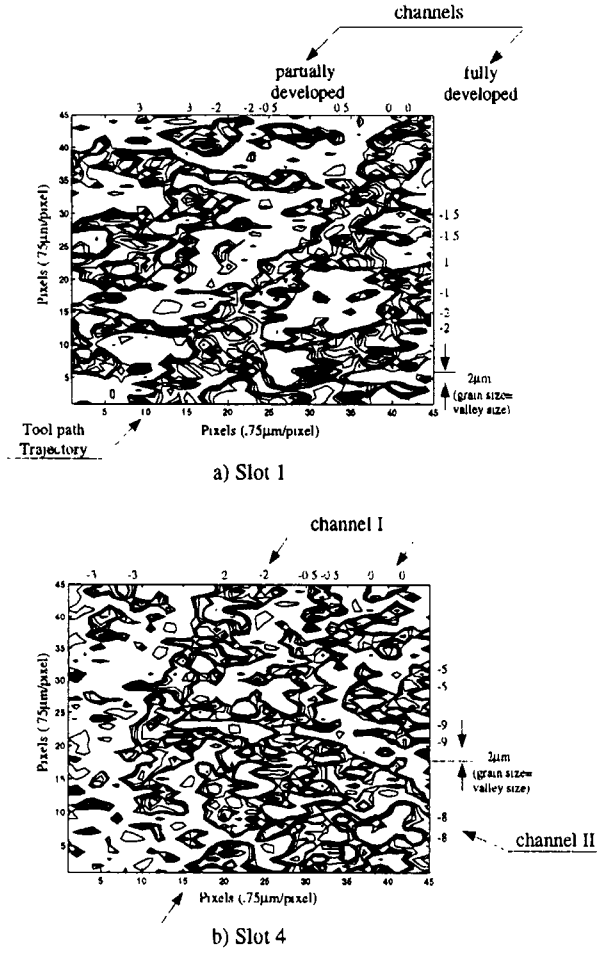

Figure 6-6. Contour Map for Quantifying the Machining Induced Surface Texture

Examining the two contour maps, several important observations can be made. The first observation is the presence of isolated islands formed by clustered contour lines on the contour maps. These isolated islands represent valleys formed on the surface texture. The size of these isolated islands characterizes the geometric shape of their corresponding valleys. It is interesting to note that the smallest size of a valley on both maps is about 2 x 2 μm, which is about the grain size of the Dicor material used in this study. This observation suggests the existence of pullouts of a single grain during

machining. It is well understood that grain boundaries in Dicor material represent a weak link when subjected to a tensile stress field due to the presence of second phase. The development of micro-cracking on the grain boundary enforces an entire grain to dislodge from the surface being machined. Valleys or cavities on the surface texture are formed as a result of these pullouts. The second observation is that most of the islands shown in Figure 6-6a are larger than the 2 x 2 μm islands. The average size of these islands is somewhere between 10 x 5 μm and 10 x 10 μm. The 10 μm is about one dimension related to the size of mica-flakes. Wenote that the Dicor material used in this study contains mica-flakes as a second phase. Addition of these mica flakes is designed to improve the machinability, a mechanism similar to free-machining steel where inclusions are added. This observation indicates that the easy-cleavage properties of mica flakes create the weak boundaries which promote the micro-cracking propagation. By closely examining those large islands shown in Figure 6-6a, small islands can also be identified within them, indicating that the co-existence of the pullouts of single grains and the progressive development of micro-cracking between the neighboring grain boundaries.

The third observation is the presence of cavity channels. Some of them are fully developed and some are partially developed, as illustrated in Figure 6-6a. The formation of these cavity channels is closely related to the internal stress field developed on/near the machined surface during machining. The most noticeable characteristic of the cavity channels is that their orientation follows the tool path trajectory. This suggests that the tensile stress induced by machining is along the cutting speed direction. Under high internal stresses, micro-cracks merge along the tensile stress direction while releasing the strain energy accumulated under the buildup of hydro-static stresses. As long as a sufficient amount of the released energy is available, cavity channels will be formed in a completed form during the material removal process. Otherwise, partially completed channels will be formed.

6.2.4 Evaluation of Cavity Density

To quantitatively describe the surface texture formed during the machining of ceramics, a new parameter is introduced in this study. The parameter is denoted as cavity density. It is defined as a percentage of the area covered by cavities or valleys, and is evaluated at a given elevation level. In practical applications, the cavity density has its implication on how deep a post-machining process, such as polishing, should go to remove the surface irregularities. Figure 6-7 presents the evaluated cavity densities associated with the eight machined surfaces. These percentages are evaluated at a distance of one micrometer below the reference plane for the R_a evaluation. The lowest value of cavity density is 1.52% and the highest value 46.33%. It is interesting to note that the lowest and highest cavity densities correspond to the least and most material removal rates used during the machining, respectively.

6.2.5 Characteristics of Material Microstructure

Based on the observations discussed, several elements of material microstructure have direct effects on the surface texture formation during machining. The pullout of individual grains implies that the size and shape of grains control the size and shape of micro-scale cavities because they are matching partners. The volume fraction of second phase determines the stress development on grain boundaries. From a viewpoint of improving machinability, weak boundaries promote micro-cracking activities during machining, thus facilitating the material removal process. However, the size and shape of the second phase has to be prepared such that the desired cracking merge and cleavage during machining are obtainable. The Dicor material used in this study contains the needle-shape of mica-flakes, lending the material to be machinable.

6.2.6 Machining Parameters

The three machining parameters selected in this investigation are the axial depth of cut, feedrate, and spindle speed. As the data accumulated in this study indicate, their effects on the surface texture formation are important, some of them are very critical in terms of controlling the micro-cracking activities during machining.

Examining the cavity density data presented in Figure 6-7, the largest difference between two parameter settings is 35.59% (37.11% - 1.52%). This difference is contributed by a shift of the feedrate setting from 5 mm/min to 10 mm/min while maintaining the depth of cut and spindle settings unchanged at 0.25 mm and 600 rpm, respectively. The main effect of feedrate on the cavity density can be calculated by averaging the four differences as listed in Figure 6-7. It is 18.39%, which is the largest among the three averages listed in Figure 6-7. It is well understood that a large feedrate setting results in a rough surface because a significant amount of material will be uncut during machining and remain on the machined surface. However, there is another effect, which is vital during the machining of ceramics. This effect is best depicted in Figure 6-6b where fully developed channels intersect each other during machining. As illustrated, channel I represents the tool path trajectory followed by tooth I during machining and channel II represents the tool path trajectory followed by tooth 2. When the two trajectories meet, the material at the cross point, which is uncut during the end mill first pass, will be removed during the second pass. The brittle nature of the material and the lack of support due to partial removal of the material on the back present an environment in which, cracking not only in micro-scale, but also in macro-scale, can easily occur. The chipping off

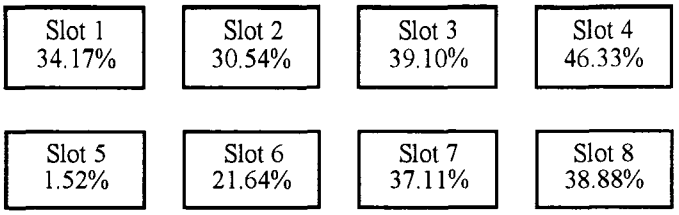

Main Effects:

$$\text{Depth of Cut} = \frac{(34.17-1.52)+(30.53-21.64)+(39.10-37.11)+(46.33-38.88)}{4} = 12.75\%$$

$$\text{Spindle Speed} = \frac{(30.54-34.17)+(46.33-39.10)+(21.64-1.52)+(38.88-37.11)}{4} = 6.38\%$$

$$\text{Feed} = \frac{(39.10-34\ 17)+(46.33-30.54)+(37.11-1.52)+(38.88-21.64)}{4} = 18.39\%$$

Figure 6-7. Densities Evaluated at (- 1 μm) Elevation Level

at those cross points leads to massive cavities formed on the surface texture.This observation also confirms an early finding in the study of chip formation that a large variation of chip size lead to a rougher surface finish, which calls for controlling the chip size variation to improve finish quality [10].

The effect of depth of cut on the surface texture formation can be sensed by examining the four differences between the upper and lower rows. The largest value of cavity density is 32.65% (34.17% - 1.52%), representing that a shift of depth of cut from 0.25 mm to 0.50 mm also changes the surface texture drastically. The average effect, or the main effect, is 12.75%, as calculated and listed in Figure 6-7, which is very close to the average effect of feedrate. This implies that the depth of cut is a very influential parameter in controlling the cavity density. This critical influence is due to the fact that depth of cut has its most influence on the cutting force generation. The cutting force is the dominant factor in determining the internal stress level, thus in determining the micro-crack initiation and propagation.

The effect of spindle speed, or cutting speed, on the cavity generation does not show as strongly as feedrate and depth of cut do. Certainly, an increase in spindle speed has a negative effect on the cavity generation. The average effect in this study is 6.38%, as indicated in Figure 6-7. It is understood that machining at high cutting speed resembles a high loading rate, which decreases the crack toughness of ceramic material. However,

machining at high cutting speed brings an elevated temperature environment. The crack toughness increases with the increasing temperature. The two conflicting effects give rise to a less significant position for the cutting speed to play in controlling the surface texture formation.

6.3 Study of the Edge Effects

In the second part of this chapter, we address a special type of surface and/or subsurface damage induced during the machining process, called edge chipping. Figure 6-8 illustrates a representative edge chipping phenomenon observed during an end milling process. Edge chipping encompasses surface damage both in macro-scale and in micro-scale. Its presence on finished products not only vitiates dimensional and geometric accuracy, but also causes possible severe failure of the ceramic component during service due to the micro-cracks left on the machined surface. Subsequently, the control of chipping effects in machining ceramic materials represents a new challenge to the manufacturing community. Research on characterizing edge chipping induced by the material processing, although not extensive, initiated as early as 1960. As reported in [8], a form tracer was used to measure the size and shape of edge chipping along the edge formed during machining. A general conclusion was made that chipping size was proportional to the material removal rate during machining. However, the previous research remained as qualitative studies, instead of quantifying the edge chipping effect.

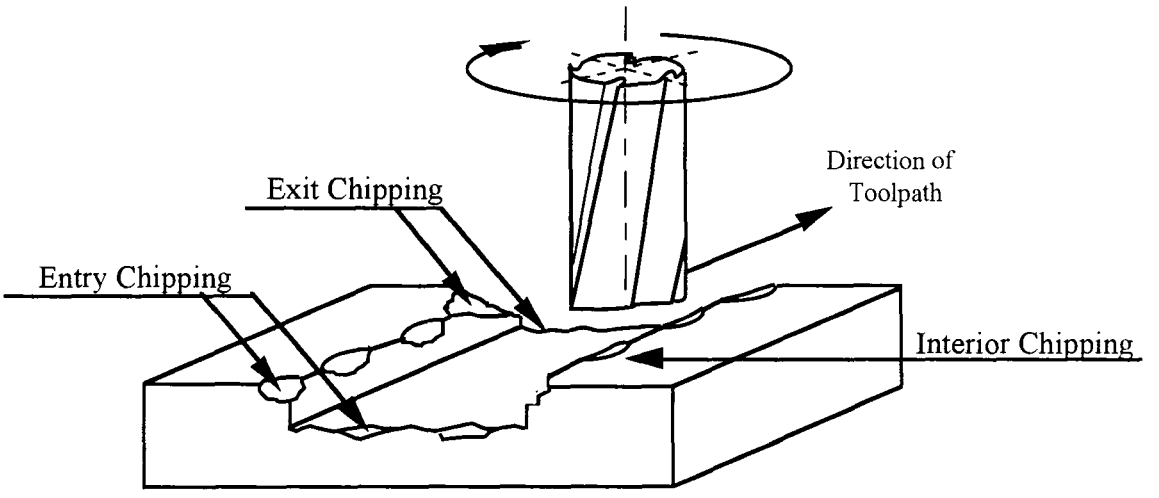

Figure 6-8. Illustration of the Edge Chipping Phenomenon

6.3.1 Characterization of Edge Chipping Phenomenon

As illustrated in Figure 6-8, the formation of edge chipping initiates at the instant when the cutting tool contacts the ceramic part being machined. Edge chipping occurs on both sides along the machining path, and is present when the cutting tool leaves the ceramic part. According to the time history, the formation of edge chipping can be distinguished by three types:

(1) *Entry chipping.* Entry chipping is primarily formed during the initial impact of the dynamic loading process when the cutting tool first contacts the part material.

(2) *Interior chipping.* Interior chipping is the most dominant chipping formed in the process of material removal along the tool path.

(3) *Exit chipping*. Exit chipping is formed due to the sudden release of the stress energy, built in the part material during the machining process, at the instant when the cutting tool is leaving the part material.

As we have observed, the edge chipping remaining on the machined part can cause serious problems in fabrication due to a loss of geometric accuracy and the presence of micro cracks. It should be noted that edge chipping is a fracture mechanism. Its formation is related to the microstructures present in the part material, the size and shape of grains, and the internal stress distribution. Although edge chipping in macro-scale can be observed by careful visual examinations, edge chipping in micro-scale requires special efforts to identify its size and geometric shape characteristics.

Figures 6-9a, 6-9b, and 6-9c present the three types of chipping: the entry chipping, interior chipping, and exit chipping. Each figure provides eight representative SEM micrographs examined at the entry, interior, and exit locations, respectively. The SEM micrographs contain 640 pixels by 480 pixels, which

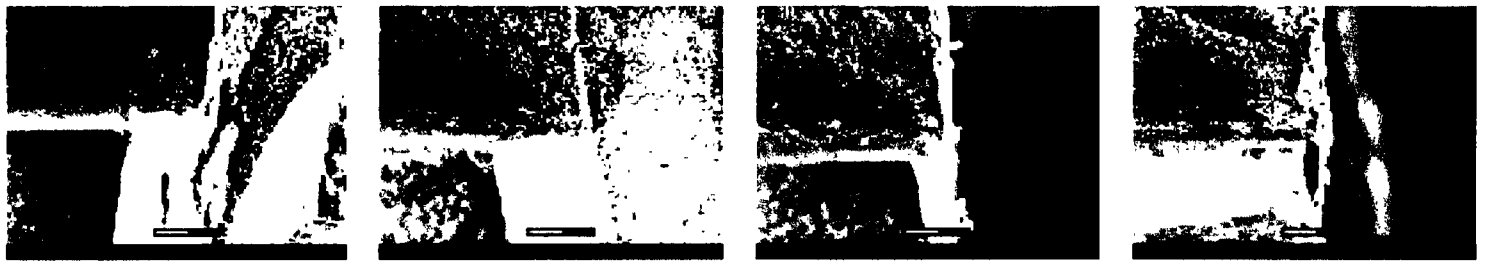

Slot 1
Cutting Speed = 600 rpm
Feed = 5 mm/min
Depth of Cut = 0.50 mm

Slot 2
Cutting Speed = 900 rpm
Feed = 5 mm/min
Depth of Cut = 0.50 mm

Slot 3
Cutting Speed = 600 rpm
Feed = 10 mm/min
Depth of Cut = 0.50 mm

Slot 4
Cutting Speed = 900 rpm
Feed = 10 mm/min
Depth of Cut = 0.50 mm

Slot 5
Cutting Speed = 600 rpm
Feed = 5 mm/min
Depth of Cut = 0.25 mm

Slot 6
Cutting Speed = 900 rpm
Feed = 5 mm/min
Depth of Cut = 0.25 mm

Slot 7
Cutting Speed = 600 rpm
Feed = 10 mm/min
Depth of Cut = 0.25 mm

Slot 8
Cutting Speed = 900 rpm
Feed = 10 mm/min
Depth of Cut = 0.25 mm

Figure 6-9a SEM Micrographs of the Entry Edge of the Ceramic Specimen

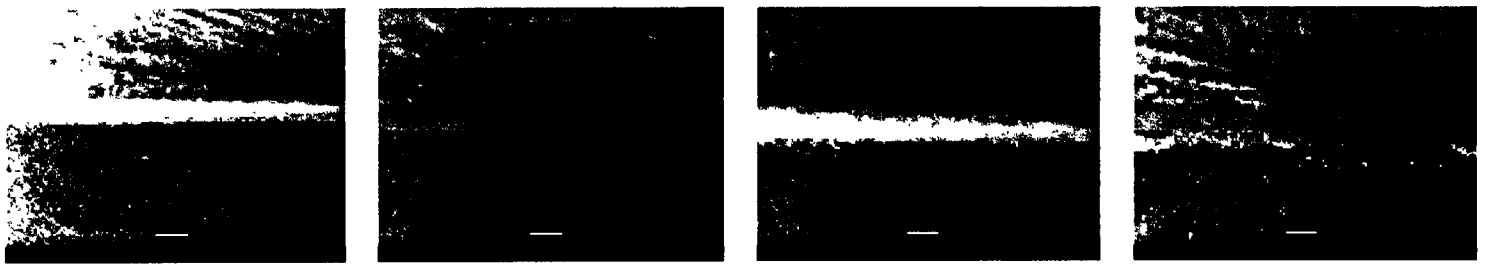

Slot 1
Cutting Speed = 600 rpm
Feed = 5 mm/min
Depth of Cut = 0.50 mm

Slot 2
Cutting Speed = 900 rpm
Feed = 5 mm/min
Depth of Cut = 0.50 mm

Slot 3
Cutting Speed = 600 rpm
Feed = 10 mm/min
Depth of Cut = 0.50 mm

Slot 4
Cutting Speed = 900 rpm
Feed = 10 mm/min
Depth of Cut = 0.50 mm

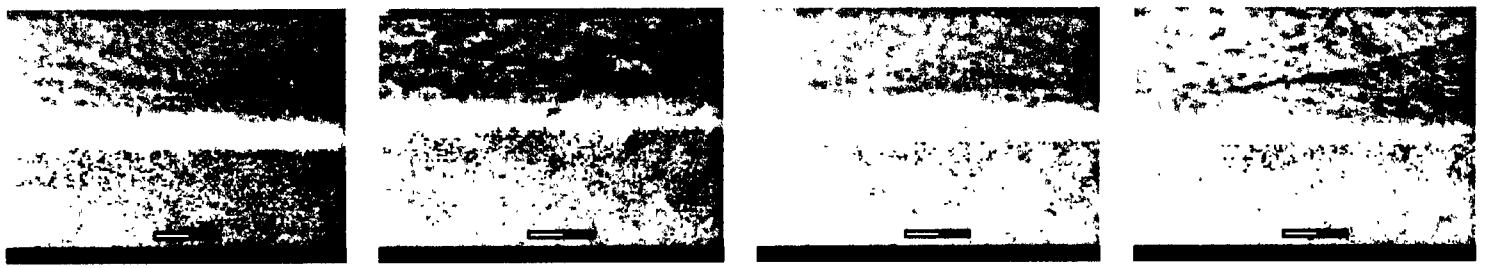

Slot 5
Cutting Speed = 600 rpm
Feed = 5 mm/min
Depth of Cut = 0.25 mm

Slot 6
Cutting Speed = 900 rpm
Feed = 5 mm/min
Depth of Cut = 0.25 mm

Slot 7
Cutting Speed = 600 rpm
Feed = 10 mm/min
Depth of Cut = 0.25 mm

Slot 8
Cutting Speed = 900 rpm
Feed = 10 mm/min
Depth of Cut = 0.25 mm

Figure 6-9b SEM Micrographs Along the Machined Slot of the Ceramic Specimen

Slot 1
Cutting Speed = 600 rpm
Feed = 5 mm/min
Depth of Cut = 0.50 mm

Slot 2
Cutting Speed = 900 rpm
Feed = 5 mm/min
Depth of Cut = 0.50 mm

Slot 3
Cutting Speed = 600 rpm
Feed = 10 mm/min
Depth of Cut = 0.50 mm

Slot 4
Cutting Speed = 900 rpm
Feed = 10 mm/min
Depth of Cut = 0.50 mm

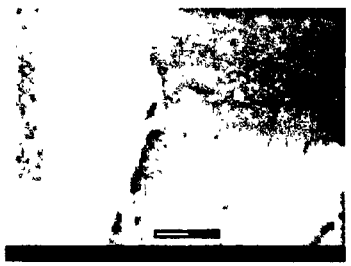

Slot 5
Cutting Speed = 600 rpm
Feed = 5 mm/min
Depth of Cut = 0.25 mm

Slot 6
Cutting Speed = 900 rpm
Feed = 5 mm/min
Depth of Cut = 0.25 mm

Slot 7
Cutting Speed = 600 rpm
Feed = 10 mm/min
Depth of Cut = 0.25 mm

Slot 8
Cutting Speed = 900 rpm
Feed = 10 mm/min
Depth of Cut = 0.25 mm

Figure 6-9c SEM Micrographs of the Exiting Edge of the Ceramic Specimen

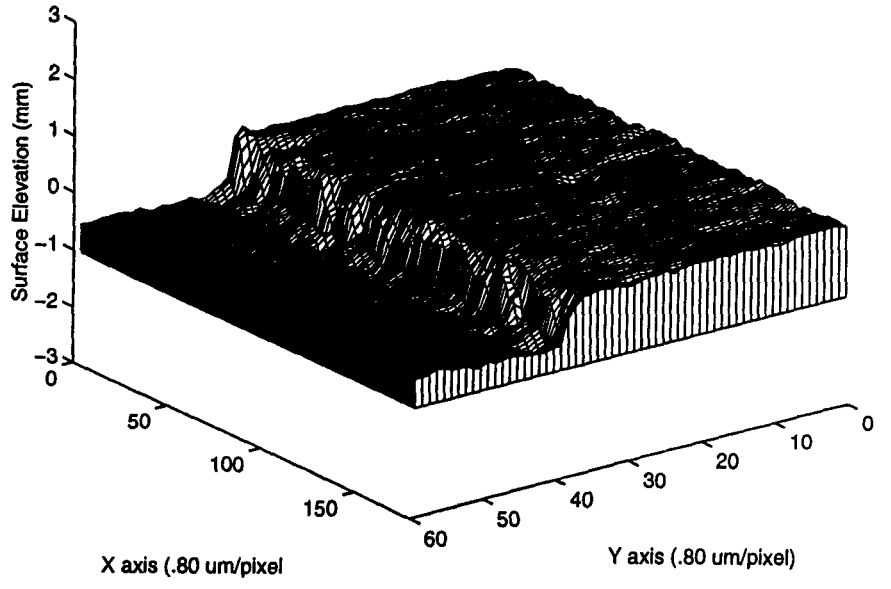

a) Slot 1 (Depth of Cut = 0.50 mm)

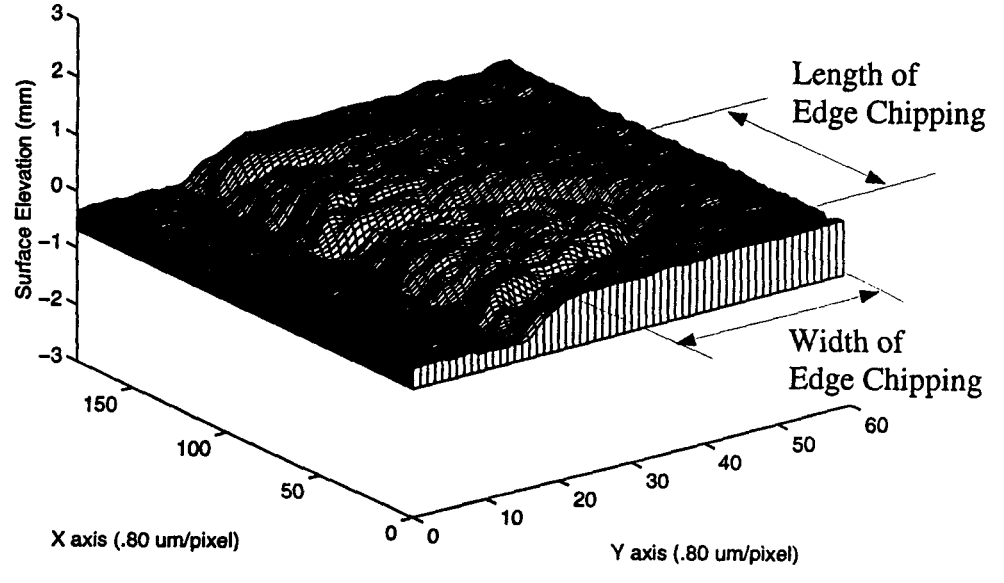

b) Slot 5 (Depth of Cut = 0.25 mm)

Figure 6-10 Three Dimensional Reconstructed Topography of the Machined Edges

represents a scanning area of 0.50 x 0.35 mm^2. Figures 6-10 present two surface topographs reconstructed in three-dimensional space using computer graphics with the transformed height variation data. The edge chipping topography displayed in Figure 6-10a is associated with a small depth of cut, 0.25 mm, while Figure 6-10b represents an edge chipping topography with the depth of cut set at 0.50 mm. A comparison of the two edge chipping topographies reveals that the edge chipping associated with the small depth of cut is significantly more severe than that associated with the large depth of cut, which clearly demonstrates the effect of depth of cut setting on the interior edge chipping formation during machining.

The size of edge chipping damage due to brittle fracture is a critical factor in assessing the machining performance for damage control. Characterization of the edge chipping sites is extremely important for correlating the edge chipping effect to the machining setting condition. In this study two quantitative measurements, i.e., the

Table 6-2. Results of Chip Length, Width and Aspect Ratio Evaluation

Slot Number	1	2	3	4	5	6	7	8
Chip Length (μm)	40.7 (30.2) (51.2)	40.2 (36.3) (44.1)	46.1 (35.8) (56.4)	76.1 (58.7) (93.5)	102.6 (62.0) (143)	101.0 (83.6) (118)	106.4 (60.8) (152)	169.8 (123) (216)
Chip Width (μm)	13.2	12.8	15.7	27.4	37.3	39.0	37.2	56.4
Aspect Ratio (L/W)	3.0	3.3	3.2	3.0	2.8	2.6	3.0	3.2

length and the width of edge chipping are used to characterize the interior edge chipping phenomenon, which constitutes a dominant portion of all edge chipping in the slot milling process. Because a noticeable difference of the interior edge chipping on the left and right sides exists, data are taken on both sides and recorded. A ratio of the measured

length to the measured width, denoted as the aspect ratio, is then calculated. Table 2 lists the measured and calculated data for subsequent analyses.

6.3.2 Evaluation of the Length of Edge Chipping

The data listed in the second row of Table 6-2 represents the lengths of the edge chipping for the eight machining conditions. The average of the first four numbers, associated with a depth of cut equal to 0.50 mm, is 50.8 μm, and the average of the second four numbers associated with a depth of cut equal to 0.25 mm is 120.0 μm, as calculated below. Thus, the effect of depth of cut on the edge chipping length is evident. A small depth of cut setting will induce interior edge chipping with a large length.

$$\frac{40.7 + 40.2 + 46.1 + 76.1}{4} = 50.8 \quad (\mu m)$$

$$\frac{102.6 + 101.0 + 106.4 + 169.8}{4} = 120.0 \quad (\mu m) \qquad (6.1)$$

The two circled numbers listed below each edge chipping length value in the second row represent the lengths of the edge chipping on the right and left sides of the respective slot. Although each side of the slots was subjected to identical machining conditions, the numerical data on the right side is consistently larger than that on the left side, indicating an effect of the direction of end milling rotation on edge chipping. Figure 6-11 offers the explanation of this effect, which is derived from the configuration of cutting geometry during the material removal process. As illustrated, the thickness of cut on the right side is significantly larger than that on the left side. Consequently, the cutting force generated during machining will be significantly larger while machining the right side, as compared to the magnitude of the cutting force generated while machining the left side. It is well understood that a large external force induces a strong internal stress field in the part

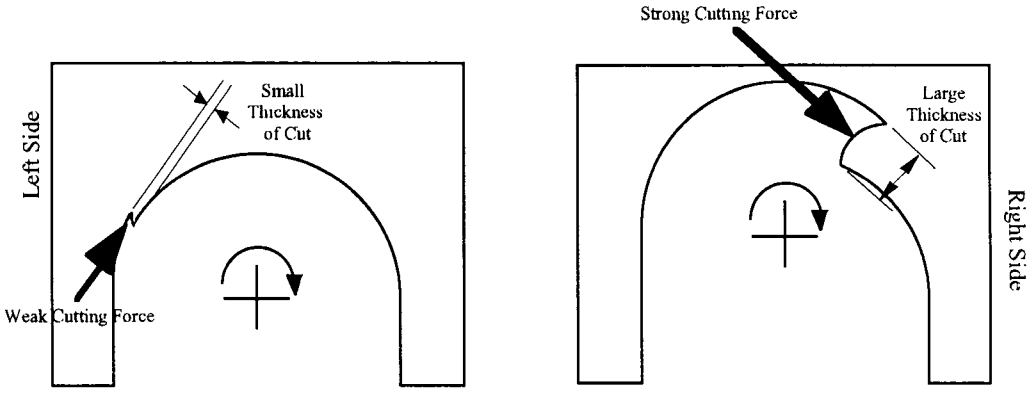

Figure 6-11. Effect of the Direction of End Mill Rotation on Edge Chipping

material being machined, thus leading to severe stress concentration and greater edge chipping thereafter.

In order to correlate the edge chipping effect to the machining parameter settings, an empirical model is derived from the data listed on the second row in Table 6-2. It is given by

$$\text{Chip Length} = 85.4 + 22.8\,(\text{Spindle Speed}) - 69.2\,(\text{Depth of Cut}) + 28.5\,(\text{feed}) \qquad (6.2)$$

The three coefficients listed in the model, +22.8, -69.2, and +28.5, characterize the effects of three parameters on the length of edge chipping. The two positive signs mean that the length of edge chipping will increase as spindle speed and feed increase. On the other hand, the negative sign with depth of cut indicates a large depth of cut setting tends to reduce the length of edge chipping. The derived empirical model is very useful for providing guidelines in setting the machining parameters during the machining of ceramic materials.

6.3.3 Evaluation of the Aspect Ratio of Edge Chipping

Examining the aspect ratio data listed in Table 6-2, an important observation is that the aspect ratio remains almost constant with small variation about the mean value of 3. This indicates that the edge chipping with large length is usually associated with large width, and the edge chipping with small length associated with small width. Consequently, the volume of individual edge chipping locations, or individual edge chipping cavities, varies in a specific pattern as they jump from one value to another. This phenomenon indicates that the formation of edge chipping is related to certain inherent properties of the material being machined. Among them, the microstructural characteristics are more likely to be responsible. These characteristics include the grain size, weak grain interfaces, and volume fraction of the second phase.

6.3.4 Evaluation of the Cavity Density of Edge Chipping

In order to gain a comprehensive understanding between the fracture mechanism present during machining and the formation of edge chipping, a special effort is made. The method of contour mapping is used to evaluate the cavity density, a performance index defined to characterize the third dimension of edge chipping.

Examining the two reconstructed surface topographies shown in Figs. 6-11a and 6-11b, they represent two visualized edges formed during the machining of the two slots, i.e., slot 1 and slot 5, respectively. As depicted, the extent of chipping generated damage on slot 1 is much more severe than that on slot 5 because it has a much larger chipping size formed. Note the scale used in the visualization. In the marked X and Y axes, each

pixel represents 0.8 μm, and the indicated area 160 pixels by 80 pixels represents an actual area of 128 μm x 64 μm. The unit of the vertical axis is also in micrometer.

To quantify the surface texture of the chipped edges, contour plots are taken at six levels on the vertical direction. They are 0 mm, -0.1 mm, -0.2 mm, -0.3 mm, -0.4 mm and -0.5 mm with the level 0 mm representing the reference plane for material removal, as illustrated in Figure 6-12a and 6-12b. Figures 6-13a and 6-13b present the two assembled contour maps for the two chipped edges of slot 1 and slot 5, respectively. On the these contour maps, the grain size of 2 μm is also indicated as reference for examination. Important observations are listed as follows:

(1) The size of the chipping formed varies as the machining condition varies. In Figure 6-12a, the corresponding cutting condition are cutting speed: 600 rpm, feed rate: 5 mm/min, and depth of cut: 0.5 mm. The average chipping size, as indicated by those small isolated islands formed by clustered contour lines on the contour map, is 8 μm x 2.4 μm at -0.2 mm level. In Figure 6-12b, while maintaining the same cutting speed and feed rate, a smaller depth of cut, 0.25 mm, is used. The average chipping size increases to 96 μm x 40 μm, indicating severe edge chipping as discussed previously. It is interesting to note that the smallest size of edge chipping

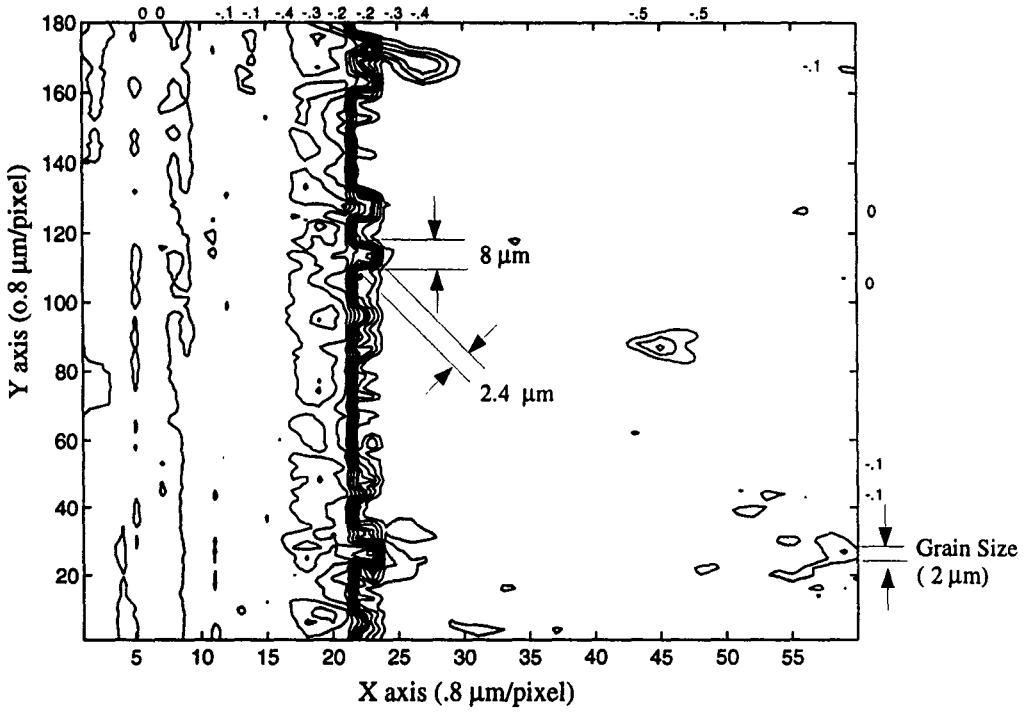

a) Slot 1(Chip Size Evaluated at -02mm)

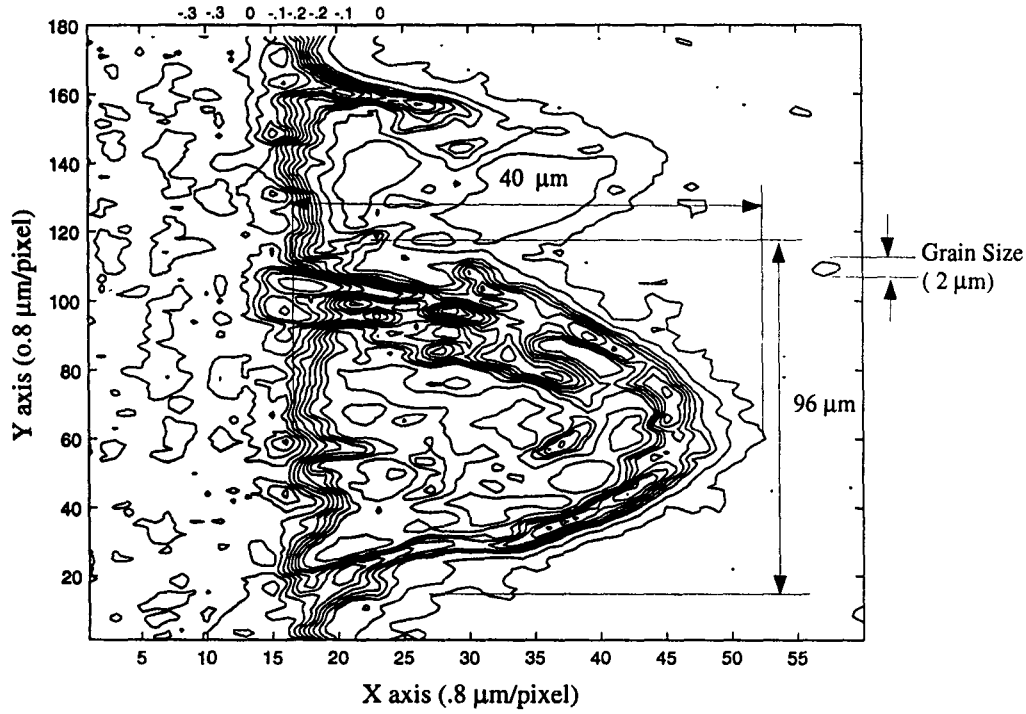

b) Slot 5 (Chip Size Evaluated at -02 mm)

Figure 6-12 Assembled Contour Maps of the Machined Edge Topography

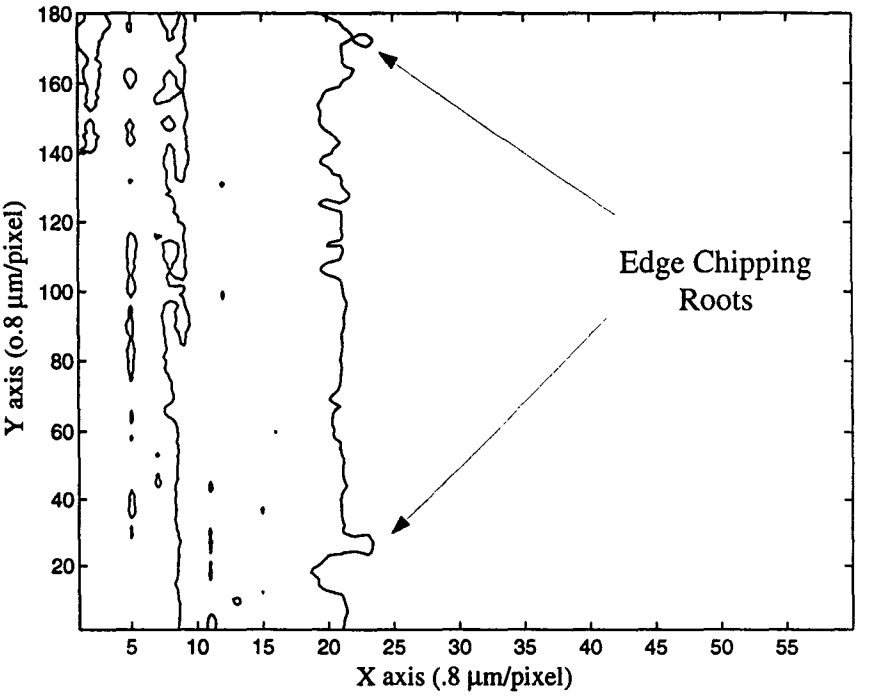

a) Slot 1(Elvation Level = -0.35 mm)

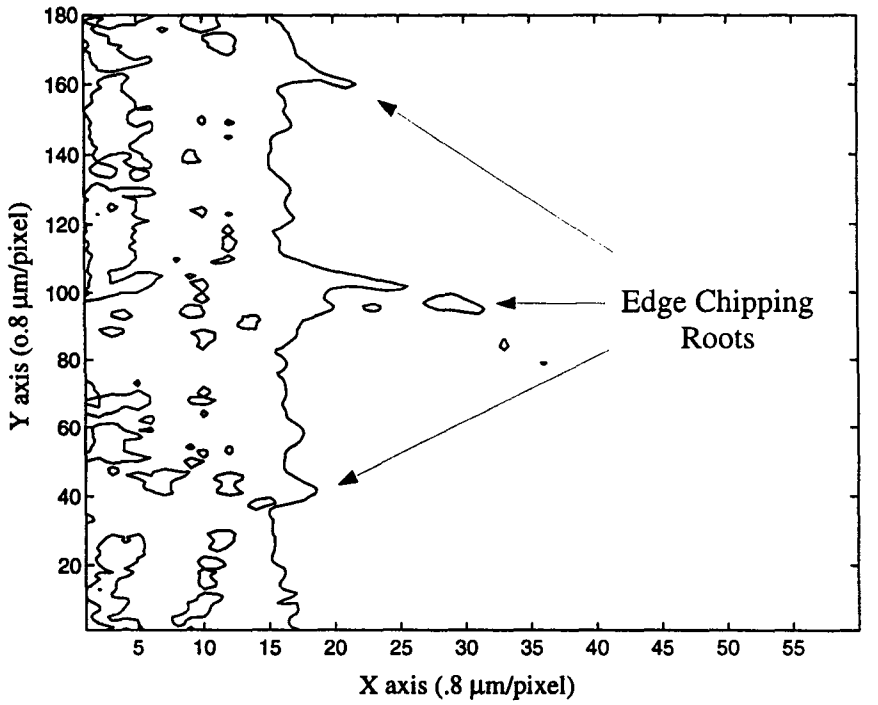

b) Slot 5 (Elevation Level = -0.25 mm)

Figure 6-13 Contour Maps of the Machined Edge Topography Illustrating Roots of Edge Chipping

on both maps is about 2 μm, which is about the grain size of DICOR material used in this study. This observation suggests the existence of pullouts of a single grain during machining. It is well understood that grain boundaries in DICOR material represent a weak interface when subjected to a tensile stress field due to the presence of second phase - mica flakes. Edge chipping with small sizes can be due to the dislodgment of individual grains. On the other hand, macro-scale edge chipping is mainly caused by intergranular fracture along multi-grain boundaries.

(2) The density of contour lines surrounding the isolated islands characterizes the depth of edge chipping. To quantify the depth of the edge chipping, contours are constructed as the elevation level goes down toward the machined surface. Figures 6-13a and 6-13b are the two contour maps, on which the edge chipping almost disappears, indicating the location of the edge chipping root. The two relative distances between the contour map and the machined surface are marked on Figures 6-13a and 6-13b, which are 0.35 mm and 0.25 mm, respectively. If comparing the distance with the depth of cut setting for slot 5 which is equal to 0.25 mm, it is evident that the edge chipping starts at the corner of the end milling tool where stress concentration is built up. Cracks are formed and then propagated upward. When the crack propagation reaches the free-surface of the part material, edge chipping occurs. However, for the case of a large depth of cut setting, the crack propagation has its limit. The built-up strain energy may not be sufficient enough to allow the crack propagation reaching the free-surface.

6.3.5 Control of Edge Chipping during Machining

Control of edge chipping on the shop floor and/or on clinic sites is a major issue during the machining of DICOR material. For the three types of edge chipping, different approaches should be applied. For instance, controlling the direction of end mill rotation may represent an effective and economic way to minimize the interior edge chipping effect as long as the side with severe edge chipping is removed after machining. In this paper we present a new approach to control the edge chipping at both entry and exit locations.

6.3.6 Addition of Epoxy Material at the Entry and Exit Locations

The basic methodology employed in the new approach is illustrated in Figure 6-14. Epoxy material is used to construct a sandwich structure, in which the glass ceramic specimen is placed between two epoxy blocks. Such a design follows two considerations:

1. Providing an energy buffer to prevent sharp impact at the entry location; and

2. Providing additional support to back the ceramic material at the exit location.

Note that the two epoxy blocks shown in Figure 6-14 cover the left portion of the ceramic specimen only. The right portion remains unsandwiched. This special arrangement allows a side-by-side comparison to determine whether the added epoxy material attenuates the entry edge chipping and/or the exit edge chipping during machining.

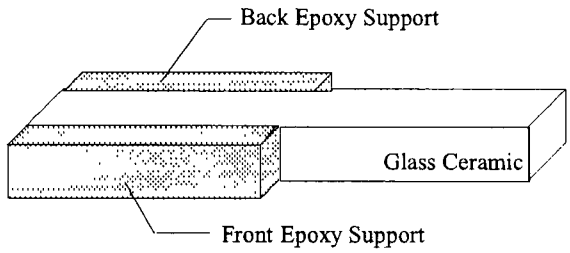

(a) Before Machining

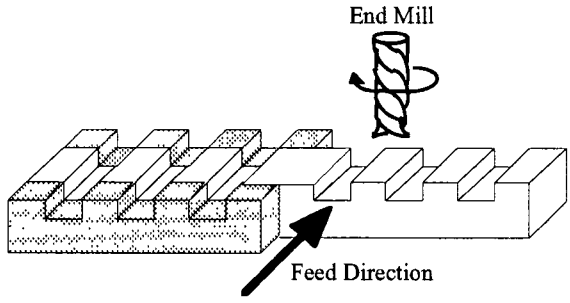

(b) After Machining

Figure 6-14. Addition of Epoxy Material to the Ceramic Specimen

6.3.7 Experimental Investigation

The experimental investigation using the specimen with the epoxy material blocks to study possible protection of edge chipping consists of two steps:

Step 1: Duplicates of slots are machined with identical cutting parameter settings. As illustrated in Figure 6-14, three slots are machined on the left portion and three slots are machined on the right portion. The cutting parameter settings are: spindle speed = 900 rpm, feed rate = 0.005 m/min, and depth of cut = 0.25 mm. An end mill with a diameter of 3.175 mm is used.

Step 2: After machining, the edge chipping effects at the entry and exit locations are examined under the environmental scanning electron microscope (ESEM). Four micrographs, which are representative of the edge chipping damage, are shown in Figure 6-15. The top two micrographs show the entry edge chipping and the exit edge chipping without the epoxy block support. The two micrographs below them are taken from the left portion where additional support with the epoxy blocks is present during machining.

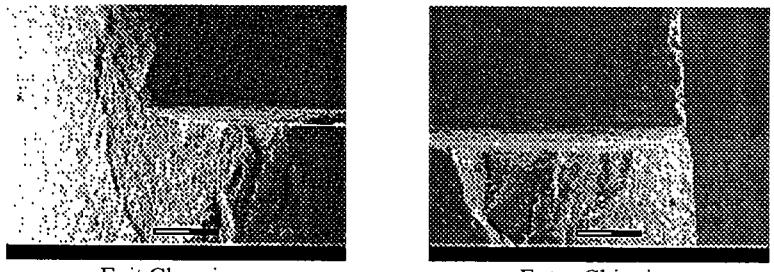

Exit Chipping Entry Chipping

(a) Without Epoxy

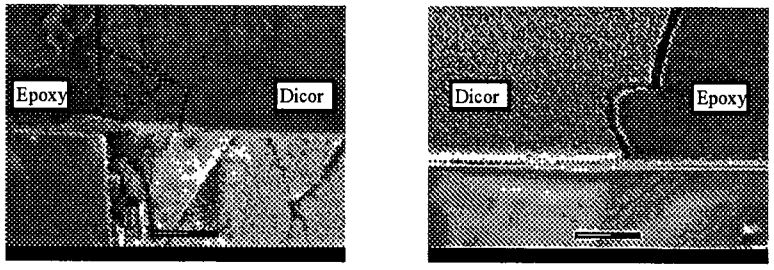

Exit Chipping Entry Chipping

(b) With Epoxy

Figure 6-15. Comparison of Edge Chipping at the Entry and Exit Locations with/without Presence of Epoxy Blocks

Examining the two micrographs at the entry location, significant reduction of edge chipping when epoxy block was present during machining can be observed. This concludes that, serving as a buffer, the epoxy material absorbed the impact energy and a

smooth transition of the end mill from leaving the epoxy material to entering the ceramic material was achieved.

Examining the two micrographs at the exit location, the edge chipping with presence of the epoxy block is as severe as that without the epoxy block support. Figure 6-16 presents an enlarged view of the exit edge chipping with presence of the epoxy block. The interface between the epoxy material and the ceramic specimen is marked. A micro-scale gap on the interface can be observed. Micro cracking on the ceramic specimen is clearly depicted in the area Just before the gap. These observations indicate that there exists discontinuity on the interface in terms of the energy transition from the ceramic part to the epoxy block. Figure 6-17b qualitatively describes that a small portion of the built-up strain energy is transferred to the epoxy block and a significant portion of the built-up strain energy is lost on the interface. The lost energy is converted to surface energy in the process of micro-cracking at the exit location.

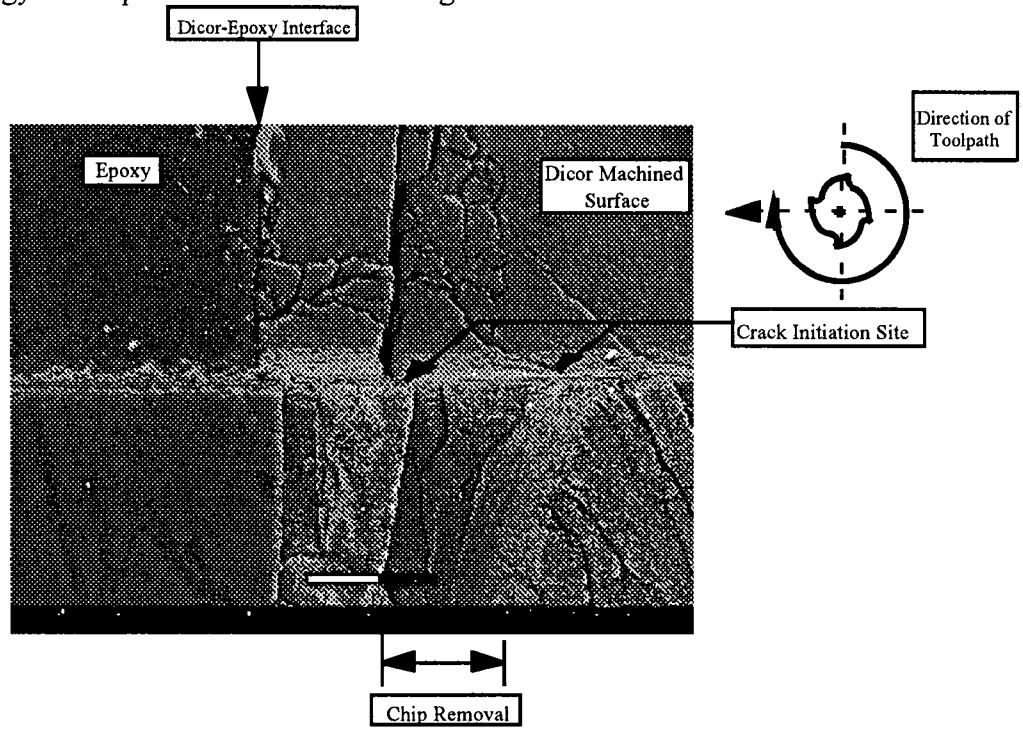

Figure 6-16. Micro-Cracking on Interface between the Ceramic Specimen and the Epoxy Block

6.3.8 Analysis Using Finite Element Method

In this study, an attempt has been made to use finite element method to examine the stresss distribution at the exit edge developed in the machining zone. The study has been very limited. Therefore, the results presented in this study serves as a reference only. It is interesting to note that the edge chipping on the left side of the slot is much more severe as compared with that on the right side. It might be contrary to what has been observed from the interior edge chipping effect, in which the edge chipping on the left side of the slot is much less severe than that on the right side. To gain a comprehensive understanding, an analysis using finite element method is conducted. Figure 6-17a presents the mesh generation and the induced stress distribution obtained from the finite element analysis. The distribution illustrates the concentration of tensile stress at the left corner at the exit location and the compressive stress at the right corner. Note that the cutting force acting at the right corner is significantly reduced at the exit location because of the reduction of thickness of cut, considering the fact that the end mill is rotating from the air to contacting the ceramic specimen when it cuts the right corner.

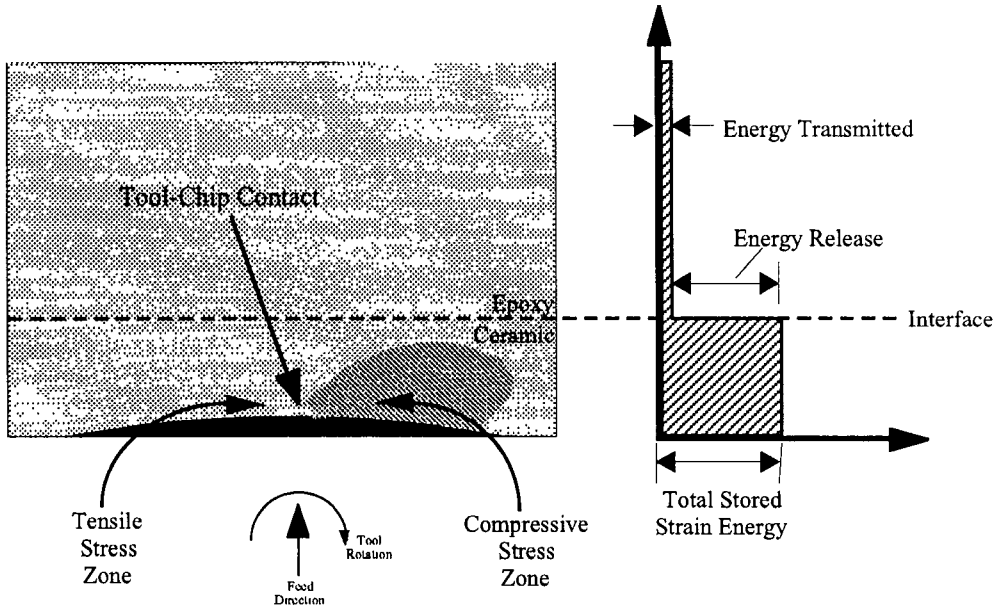

(a)Induced Stress Distribution (b) Energy Distribution

Figure 6-17. Analysis Using Finite Element Method and Energy Distribution on the Interface

Chapter 7

Conclusions and Recommendations

7.1 Conclusions

The overriding objective of this thesis has been to evaluate the machinability of dental restorative materials. Recognizing the influence of material properties on the mechanisms of material removal, special efforts have been devoted to gaining a comprehensive understanding of the material properties and investigating the interrelationships between the material properties and machining processes. The ultimate goal of this thesis study is to provide guidelines for controlling the material process and ensuring cost-effective machining operations for dental restoration fabrication. Important contributions of this thesis work are summarized in the following:

1. A new formula to determine microhardness values for indentation tests is proposed in this research. By incorporating elastic recovery into evaluation, a normalized hardness measurement can be achieved to associate a given type of ceramic material with a unique hardness value. This approach offers a unique opportunity to use hardness measurement as a means for comparison and other investigations related to material hardness characteristics.

2. The SEM-stereophotography method developed in this study has been a great success in characterizing the micro-scale surface texture. The high resolution of micrographs attainable ensures coverage of rich information on surface height variation in micro-scale at an accuracy conventional profilometry methods can never achieve.

3. Identification of surface cavities provide strong evidence of the material removal mechanisms present during machining. Pullouts of individual grains due to dislodgment from the neighboring contact area and cavities formed through the progressive development of grain boundary microcracking are two among the possible material removal mechanisms.

4. Factors including material microstructure and three machining parameters, namely, feedrate, depth of cut, and spindle speed, are studied with respect to their influence on the surface texture formation. It is found that feedrate and depth of cut are the two most influential factors in controlling the cavity density, and the spindle speed has the least influence because of the conflicting effects on the crack toughness of ceramic material contributed by loading rate and temperature. It is expected that the interplay between microstructure and machining parameters will have its unique effect on the surface texture formation because of its unique effect on the microcracking activities during machining.

5. An effort has been made to search a methodology to control the edge chipping formation during machining. Epoxy material is used to provide additional support to the specimen being machined. Effectiveness of reducing the entry edge chipping has been achieved. However, no effect has been observed to control the exit edge chipping due to discontinuity of energy transformation on the interface.

7.2 Recommendations

Although the accomplishments have been significant, there is still a significant amount of work to be done in order to improve the precision and accuracy in

characterization of ceramics for dental restoration application. Several recommendations are listed as follows:

1. Study of Other Dental Ceramics. In this study, we have performed our machinability evaluation for four basic types of dental materials, Human Enamel, DICOR/MGC, HCC Enamel, and HCC Dentine. However, these are only a small batch out of the spectrum of materials considered for this dental restoration research project. Currently, there are other materials available on the market, such as Cerec Mark II, Vita Alumina, and Vita Spinell. Similar study are needed not only for these material but for new materials to be developed as well.

2. Compatiblity Study with Fatigue Test. Evaluation of microcrack using the SEM/AFM characterization methodology has been studied as part of this thesis work. It has shown great promises of using scanning electron microscopy and image processing in quantification of microcracks. Extensive studies have done in this area. One aspect, which stands out, is the study of micro-cracking with fatigue tests where a micro-crack system is introduced using fatigue tests in the laboratory environment. It is extremely important to integrate this study with the on-going research work conducted elsewhere to gain a better understanding of the micro-mechanisms in the material processing.

3. Z-direction Depth Measurement Limitation in the Atomic Force Microscope. The resolution of the SEM/AFM technique for studying hardness impressions can be effective in a depth range up to 6 μm. Measurements of the impressions used in this thesis study are within this range. Therefore, accuracy of the measurements meets the need of this study. However, measurements of impressions that have depths larger than 6 μm, may experience difficult in terms of ensuring high

accuracy. It is suggested that further improvement in the system developed in this study be considered to expand the capability of atomic force microscopy as a general technique for studying hardness impression using the three-dimensional characterization method.

4. FTIR Microscope. It has been demonstrated that surface chemistry analysis is an important aspect in the study of ceramic machining. The study is critical for chemical-assisted machining [24]. Machining under different machining environments, such as the submerged machining described in this thesis, represents a new and innovative technology for ceramic processing. Chemical additives, such as alcohol, boric acid, and others, should be tested. Under these circumstances, FTIR can be the ideal tool for studying the effectiveness of chemical-assisted machining.

References

[1] ANSYS General Purpose Finite Element Analysis (FEA) program, Revision 5.0, Swanson Analysis Systems, Inc., 1992.

[2] Barsom, J. and Rolfe, S., "Fracture & Fatigue Control in Structures,"second edition, Prentice-Hall, Inc., 1987.

[3] Box, G., W. Hunter, and J. Hunter, "Statistics for Experimenters, An Introduction to Design, Data Analysis, and Model Building." John Wiley & Sons, Inc., 1978.

[4] Evan, A.G., and Marchall, D. B., "Wear Mechanisms in Ceramics," In Fundamentals of Friction and Wear, Ed. D. A. Rigney, Metals Park, Ohio, American Society of Metals, 1980, pp. 439-452.

[5] Goldstein, J., Newbury, D., and Echlin, P., *Scanning Electron Microscopy and X-Ray Microanalysis*, Plenum Press: New York, Second Edition, 1992.

[6] Groenou, B., Maan, N., and Veldkamp, J., "The Science of Ceramic Machining and Surface Finish," edited by B. Hockey and R. Rice, National Bureau of Standards, SP-562, P. 43, 1979.

[7] Griffith, A.A., " The Phenomena of Rupture and Flow in Solids,"Philosophical Transactions of the Royal Society (London), 221, pp. 163-198, 1921.

[8] Grossman, D., "Structure and Physical Properties of Dicor/MGC Glass-Ceramic," Proceedings of the 1991 International Symposium on Computer Restorations, Regensdort-Zurich, Switzerland, 1991, pp. 103-115.

[9] Hwang T. W., "Analysis of Surface Quality in Machining of Metals and Advanced Ceramics", Ph.D. Thesis Report, University of Maryland at College Park, 1992.

[10] Inasaki, I., "Grinding of Hard and Brittle Materials," Annals of the CIRP, Vol. 36 (2), 1987.

[11] Irwin, G.R., "Fracture Dynamics," Fracturing of Metals, American Society of Metals, Cleveland, OH, 1948.

[12] Irwin, G.R., et al., "Fracturing and Fracture Dynamics," Welding Journal, Vol. 31, Research Supplement, pp. 95s-100s, 1951.

[13] Jahanmir, S., Ives, L., and Ruff, A., Ceramic Machining: Assessment of Current Practice and Research Needs in the United States, National Institute of Standards and Technology, Report SP-834, 1992.

[14] Job, L. S., " Assessment of Surface Integrity of Machined Ceramics Using Image Processing", Master Thesis Report, 1995.

[15] Khanchustambham E. G., "A Neural Network Approach to On-line Monitoring of Machining Processes, Master Thesis Report, Unversity of Maryland at College Park, 1992.

[16] Konig, W., et al, "Machining of New Materials," Processing of Advanced Materials, Vol. 1, 1991, pp. 11-26.

[17] Lawn, B., Fracture of Brittle Solids, Second Edition, Cambridge University Press, 1994.

[18] LS-A-14H Specification, Tower Oil & Technology Co., Chicago, Illinois, 1994.

[19] MATLAB: High Performance Numerical Computation and Visualizastion Software, The MATH WORKS, Inc., 1992.

[20] Mazurkiewicz, M., "Understanding Abrasive Waterjet Performance,"Machining Technology, Vol. 2, No.1, 1991, pp. 1-3.

[21] Nakagawa, T., Suzuki, K., and Uematsu, T., "Three Dimensional Creep Feed Grinding of Ceramics by Machining Center," Report in Machining of Ceramic Materials and Components: Eds. K. Subramanian, Norton Company and R. Komanduri, General Electric Company, New York, NY, ASME, 1985, pp. 1-7.

[22] Ng, S., Le D. , Tucker S., Zhang G., "Characterization of Machined Induced Edge Chipping in Glass Ceramics," Accepted to present at the 1996 ASME Winter Annual Meeting.

[23] Ohbuchi, Y., et al., " Chipping Generation Mechanism in Slot Grinding of Ferrite," Int. J. Japan Soc. Pre. Eng. , Vol.28 , No.1, Mar. 1994.

[24] Rekow, D., Zhang, G., and Thompson, V., "Machining Ceramic Materials for Dental Restorations," Proceedings of the International Conference on Machining of Advanced Materials, Maryland, July, 1993, pp. 425-435.

[25] Satish, K. G., "An Investigation of the Mechanics in the Machining of Ceramic Material", Master Thesis Report, University of Maryland at College Park, 1994.

[26] Slotwinski, J., et al., "Ultrasonic Measurement of Surface and Subsurface Structure in Ceramics," Proceedings of the International Conference on Machining of Advanced Materials, Maryland, July, 1993, pp. 117-124.

[27] Stout, K. J., ed., *Three Dimensional Surface Topography; Measurement, Interpretation, and Applications*, Penton Press: London, England, 1994.

[28] Underwood, E., "Recent Advances in Quantitative Fractography,"*Fracture Mechanics: Microstructure and micromechanisms*, edited by Nair, S. et al., ASM International, pp. 87-109, 1989.

[29] Zhang, G., Ko, W., and Ng, S., "Submerged Precision Machining of Ceramic Material," 1995 ASME Conference on Advanced Material Processing, Los Angles, July 1995.

[30] Zhang, G., Ng S., Le, D., "Characterization of Surface Texture Formed During Machining of Ceramics", Technical Papers of the North American Manufacturing Research Institution of SME, pp. 57-62, 1996.

[31] Zhang, G., Ng S., Le D. , Tucker S., Rekow D., "Three Dimensional Characterization of Indentation Impressions in Human Enamel", Submitted for Review to the Journal of Dental Materials.

[32] Zhang, G., Satish, K., and Ko, W., "The Mechanics of Material Removal Mechanisms in the Machining of Ceramics," ASME Winter Annual Meeting Proceedings, November 1994, pp. 121-135.